
THE UNIVERSITY
*of* EDINBURGH

# Nanoscale Dynamics of Ice Growth on Surfaces

*Vasileios-Martin Nikiforidis*


*Doctor of Philosophy*

THE UNIVERSITY OF EDINBURGH

2021

*To Professor Jason M. Reese*

# Abstract

The freezing of liquid water to form ice is the most common phase transition on our planet, and the ubiquity of ice growth on surfaces offers many engineering and scientific challenges. Ice growth can prevent the operation of — and cause damage to — a broad spectrum of man-made structures and devices, such as aircraft, ships, wind turbines, photovoltaic devices, heat exchangers, and telecommunications equipment. Consequently, ice growth on surfaces is an important topic of study, and undesirable ice growth can impact both life and property. While there is a vast experimental and numerical literature on how modifying surface characteristics affects ice growth, little is understood about the underlying nanoscale mechanisms. This is because icing is challenging to study experimentally, as the nucleation of ice crystals within supercooled liquid occur on the order of nanometres. Numerical investigations into icing rely on the use of molecular dynamics (MD) simulations, as MD can accurately resolve the nanoscale molecular interactions relevant to ice nucleation and growth. However, there are two issues with the use of MD: a) these simulations are computationally expensive; and b) as nucleation is a rare event when compared to MD timescales, the simulations need to be accelerated to force ice formation to occur, which affects the accuracy of the results obtained.

An alternative seeded MD simulation approach is presented in the present work, which reduces the computational cost while still ensuring accurate simulations of ice growth on surfaces. In addition, this approach enables the study of ice growth on vastly more complex surfaces than have been considered thus far. In this thesis, this approach is used to investigate fundamental questions of surface icing, such as: a) the effect of surface wettability and structure on ice growth; and b) the role of the nanometre-thick interfacial region adjacent to the surface on ice growth, which has been shown to be important in previous experiments. The findings presented here should provide an improved understanding on the role of the surface properties on the structure and dynamics of ice growth, and provide a useful framework for future slab-seeded ice growth simulations.

# Acknowledgements

First, I would like to thank the late Professor Jason M. Reese, to who I am deeply indebted for giving me the opportunity for this PhD studentship and making me part of his research group. Jason inspired motivation and was always there to provide guidance, support and opportunities to expand your knowledge and interact with people expert in the field. I consider myself fortunate to have had the opportunity to be part of his team.

I would like to thank Dr Rohit Pillai for taking over Jason's position as my first supervisor and at a difficult time. Rohit provided me with guidance, and his interest and patience were constant and unremitting throughout my PhD. I would also like to thank Dr Matthew K. Borg, my second supervisor, for his unwavering support and assistance throughout my PhD. I wish to thank Dr Saikat Datta for his help with aspects of coding and our valuable discussions. I also wish to thank Dr Livio Gibelli for our useful discussions and morning coffee that became our ritual. I am also lucky to have collaborated with AkzoNobel and Peter Jones, who has introduced me to the experimental aspects of icing.

I would also like to thank other colleagues and PhD students within our group for our talks, assistance, lunchtime banter, and time spent on group activities.

Finally, I would like to express my gratitude to all of my Edinburgh friends for making this city my second home. I am grateful to my family, especially my father George, who has always been my mentor, for their support throughout my years of studies.

# Declaration

I declare that this thesis was composed by myself, that the work contained herein is my own except where explicitly stated otherwise in the text, and that this work has not been submitted for any other degree or professional qualification except as specified.

**Vasileios-Martin Nikiforidis**

# Publications

**Invited book chapter:** Tagliaro, I., Cerpelloni, A., Nikiforidis, V. M., Pillai, R., Antonini, C. (2022) "On the Development of Icephobic Surfaces: Bridging Experiments and Simulations". In: Marengo M., De Coninck J. (eds) *The Surface Wettability Effect on Phase Change.* Springer.

**Publication submitted:** Nikiforidis, V. M., Datta, S., Pillai, R., Borg, M. K. "Impact of surface nanostructure and wettability on interfacial ice physics".

# Contents

# Figures and Tables

## Figures

---

# Tables

# List of Acronyms

**AFM** Atomic Force Microscopy
**BCC** Body-Centred Cubic
**CNT** Classical Nucleation Theory
**CB** Cassie-Baxter
**DDL** density-depleted layer
**DSC** Differential Scanning Calorimetry
**FCC** Face-Centred Cubic
**FFS** forward flux sampling
**FTIR** Fourier transform infrared spectroscopy
**HBN** hydrogen bond network
**HCP** Hexagonal Closed-Packed
**HIN** heterogeneous ice nucleation
**INA** ice nucleation agent
**KMC** kinetic Monte Carlo
**LJ** Lennard-Jones
**LIS** liquid impregnated surfaces
**MD** molecular dynamics
**MSD** mean square displacement
**mW** monatomic water
**$\mu$VT** grand canonical ensemble
**NPT** isothermal-isobaric ensemble
**NVE** microcanonical ensemble
**NVT** canonical ensemble
**PBC** Periodic Boundary Condition
**PEG** polyethylene glycol
**PPPM** Particle-Particle-Particle-Mesh
**QLL** quasi-liquid layer
**SHS** Superhydrophobic surfaces
**SLIPS** slippery-liquid-infused porous surfaces
**SW** Stillinger-Weber
**TPS** transition path sampling

# Chapter 1

# Introduction

*"I come from fields of fractured ice,*
*Whose wounds are cured by squeezing,*
*Melting they cool, but in a trice,*
*Get warm again by freezing.*
*Here, in the frosty air, the sprays*
*With fern-like hoar-frost bristle,*
*There, liquid stars their watery rays*
*Shoot through the solid crystal."*

- James Clerk Maxwell

Ice covers a substantial part of the Earth; on average 7% of the ocean's surface and 10% of the land is permanently frozen. Ice is also present in our atmosphere, and contributes significantly to the formation and precipitation of clouds. The amount of surface and atmospheric ice determines the amount of incident solar radiation reflected and adsorbed from the planet. Finally, ice is also ubiquitous outside of Earth, such as on other planets, satellites and comets in the solar system and beyond. The presence of ice is an important indicator that a celestial body is capable of supporting life. Understanding how ice behaves is thus key to answering the two most profound questions that humans face as a species, namely predicting the future of our planet and unraveling the emergence of life in the universe.

In the context of the engineering applications that motivate this thesis, icing is widely studied because it can damage man-made structures and devices. For example, ice accretion on aircraft can affect the proper functioning of aerodynamic surfaces, increasing drag, and increasing stall speed (the slowest speed at which the aircraft can maintain level flight), as well as probes and sensors, such as leading to incorrect engine power settings (R. Gent, P. Dart, 2000). Icing is also a problem on the ground in cold regions, either at high latitudes or in mountainous areas. Indeed, ice and snow

accumulation on overhead power grid components, such as conductors, ground wires and insulators, can cause power line collapse and black-outs that may last several hours; this is both a severe inconvenience for the users, and a source of economic losses for energy operators (Solangi, 2018).

The thread connecting the diverse examples of ice formation listed thus far is that in every case, liquid water comes into contact with some sort of impurity, which then initiates the process of freezing under the right temperature conditions. This process is called *heterogeneous* ice nucleation, which is the dominant mechanism of ice formation. Liquid water can also freeze in the absence of impurities via *homogeneous* nucleation, but this is rare. In fact, pure liquid water has been shown to exist in a metastable supercooled state down to $-37.5°C$ (Tian *et al.*, 2018), and can be stored for months in a lab at $-20°C$ (Huang *et al.*, 2018). Freezing in an application of interest to engineers typically occurs at higher temperatures, which means it occurs via impurity-mediated heterogeneous nucleation. It has been empirically established that the choice of material in surface design is important, as ice nucleation efficiency depends strongly on surface type. Given its importance and ubiquity, it might have been reasonable to assume that the physics of heterogeneous ice growth was well-understood. However, this is far from the case and fundamental questions regarding the formation, structure and behaviour of surface icing remain unanswered (Bartels-Rausch, 2013).

## 1.1 Three Important Questions

While ice nucleation is extremely important and has been widely-studied, it is only the first step of the process of surface icing; the formed ice nuclei have to then agglomerate with each other, form interconnected networks, and eventually grow to form bulk ice. Consequently, engineers aiming to minimise surface icing incorporate a broader set of objectives than just preventing nucleation. This includes reduction of heterogeneous nucleation rate, lowering of ice adhesion strength and increasing the freezing delay time. Focusing on ice growth, experimentalists have highlighted the importance of surface wettability and topography to surface icing (Darmanin and Guittard, 2015; Huang *et al.*, 2019; Jiang *et al.*, 2020). In addition, many research papers indicate how a small variation of the surface roughness could lead to a significant change of the icing mechanism (Eberle *et al.*, 2014; Fu *et al.*, 2015), demonstrating the potential of atomic-scale control of icing and the necessity for its systematic analysis at the molecular

level. This raises an important question: *What is the role of the surface structure and chemistry in promoting/inhibiting ice growth?*

There are two main challenges faced by experimentalists when trying to understand the mechanisms of surface icing. First, the analysis of experimental results is limited by the stochastic character of icing and the difficulties associated with water impurities and surface heterogeneities. Second, the mechanisms of icing occur in nano-to-microsecond time scales and length scales of a few hundred to thousand molecular diameters, which are very hard to observe experimentally. An alternative to running experiments is to use highly-accurate molecular simulations, using a well-validated tool such as molecular dynamics (MD). Since ice nucleation is fundamental to the initiation of icing, the majority of MD simulation studies have focused on the complex problem of the spatial and temporal evolution of heterogeneous ice nucleation (HIN). However, molecular simulations have their own set of challenges as they require massive brute-force calculations. In MD, individual atoms need to be tracked and interatomic interactions need to be computed at every timestep, making it extremely computationally expensive to simulate very small systems ($10^6$ atoms) for very small periods of time ($10^{-6}$ seconds). Additionally, given HIN is a rare event, there is no guarantee that ice formation would occur in any given simulation, and many hundreds of simulations may be necessary, which is impractical. While there are some papers that successfully conducted brute-force simulations of surface icing using all-atom water models, they did so by focusing on specific types of surfaces that favoured nucleation (Glatz and Sarupria, 2016, 2018; Li *et al.*, 2017; Zielke *et al.*, 2016). For surfaces that are not necessarily tuned to promote ice nucleation, or *unfavourable* surfaces, running successful MD simulations of icing remains a challenge.

There are two ways in which the MD community has bypassed these issues: using coarse-grained models (which reduce the interatomic interactions to be computed) or using enhanced sampling (which accelerate the freezing process). The majority of the MD literature uses coarse-grained models, such as the monatomic water (mW) model (Molinero and Moore, 2009), wherein the water molecule is approximated using a single interaction point within a sphere. The use of the mW model, which is an order of magnitude faster than all-atom water models, such as the TIP4P/Ice model (Abascal *et al.*, 2005), has produced an extensive literature on the various factors affecting heterogeneous nucleation, such as surface wettability, surface crystal morphology, surface roughness and water layering (Bi *et al.*, 2016; Cox *et al.*, 2015a; Factorovich *et al.*, 2015; Fitzner *et al.*, 2015; Lupi and Molinero, 2014; Lupi *et al.*, 2014; Singh and

Müller-Plathe, 2014). Alternatively, observable nucleation for all-atom water models can be forced to be observed within reasonable simulation timescales using enhanced sampling methods (Sosso *et al.*, 2016b), including free energy methods (Abrams and Bussi, 2014; Laio, 2002; Laio and Gervasio, 2008) and path sampling methods (Allen *et al.*, 2009; Dellago and Bolhuis, 2009; Dellago *et al.*, 1998).

However, coarse-grained models and (biased) enhanced sampling techniques (Allen *et al.*, 2006; Torrie and Valleau, 1977) have their own drawbacks. The mW model produces ice growth rates that are four orders of magnitude higher than all-atom models, which is inaccurate (Espinosa *et al.*, 2016a). With enhanced sampling methods, the simulations are still computationally expensive and are therefore usually performed at high supercooling, which is suboptimal as these low temperatures are not always representative of real-world applications (Pedevilla *et al.*, 2018). The vast majority of these enhanced simulation methods have only been used for homogeneous ice nucleation (Quigley and Rodger, 2008; Radhakrishnan and Trout, 2003; Reinhardt *et al.*, 2012), and the literature on heterogeneous ice nucleation using enhanced sampling remains sparse. This reduced accuracy and use of artificially-low temperatures limits the real-world relevance of MD simulation results; as a result, the experimental and MD communities working on surface icing have largely operated independently of each other. However, given the important insights that MD simulations can provide to designing new surfaces to combat icing, it is important to be able to run accurate icing simulations on realistic surfaces not artificially designed to promote ice nucleation. This leads to a second important question: *Can highly-accurate all-atom models be used to run unbiased MD simulations of icing on unfavourable surfaces?*

Finally, in recent years, the structure and dynamics of the interfacial region, or the exact location where the ice meets the surface, has gained importance in the heterogeneous icing community. Recent experiments have shown that a nm-thick quasi-liquid layer (QLL) can form at the surface-ice interfacial region (Björneholm *et al.*, 2016). Other studies indicate that the QLL presence leads to extremely low ice adhesion strength values, much lower than what surface-energy models predict (Chen *et al.*, 2013, 2017b). The structure and dynamics of QLL at the ice-solid interface is thus important because it can influence ice formation and growth (Amirfazli and Antonini, 2017; Chen *et al.*, 2017a; Jha *et al.*, 2016; Zeng and Li, 2019). Contrary to the studies of QLL at the ice-vapour interface, the studies of QLL at the ice-surface interface, are exclusively experimental. There have been no MD studies that investigate QLL formation and dynamics at the ice-surface interface. While advancements of experimental techniques

are useful, they need to be complemented with accurate simulations. This leads to the third and final important question: *Can MD simulations be used to study the formation of the QLL at the ice-solid interface?*

## 1.2 Thesis Goals

In the introductory section of the thesis, three important questions relating to surface icing have been identified (reordered here):

1. Can highly-accurate all-atom models be used to run unbiased MD simulations of icing on unfavourable surfaces?
2. What is the role of the surface structure and chemistry in promoting/inhibiting ice growth?
3. Can MD simulations be used to study the formation of the QLL at the ice-solid interface?

This thesis presents a methodology to address the first question raised above, in a way that avoids the difficulties encountered in conventional HIN MD simulations. The proposed approach enables monitoring of the phase transition of liquid-water molecules into ordered ice structures with an unbiased brute-force approach, and without the need for enhanced sampling or coarse-grained models. This approach enables investigation into parameters that influence formation of ice on any surface for which accurate intermolecular potential exist. Following that, a study into the effect of the surface wettability and lattice structure on ice growth is conducted, shedding light on the second question raised above. Finally, the approach can also be used to get molecular insight into the QLL structure and dynamics whenever such structures are observed in the interfacial region. This can be then linked back to the surface type and wettability, enabling insight into the third question raised above. Investigating these three open questions in heterogeneous icing using brute-force MD constitutes the novelty of this thesis.

## 1.3 Thesis Outline

The remainder of this thesis is structured as follows:

**Chapter 2 – Background** describes the objectives of current anti-icing strategies, providing theoretical background and the state-of-the-art in experimental and MD approaches. The need to further investigate the ice-surface interface is justified.

**Chapter 3 – Molecular dynamics methodology** provides the methodological basis underlying molecular simulations, introduces the slab seeding approach, and outlines the key simulation measurements that need to be performed to extract quantitative information from MD simulations.

**Chapter 4 – The influence of surface wettability and structure on ice growth** is the key results chapter of this thesis and studies the influence of surface wettability and structure on ice growth. Additionally, the structure and dynamics of the interfacial region at the ice-surface interface is investigated.

**Chapter 5 – Concluding Remarks** summarises the results of the current study and provides perspectives for future research.

# Chapter 2

# Background

*"To know what you know and what you do not know, that is true knowledge."*

- Confucius

Ice accumulation on solid surfaces has been recognised as a severe problem for safety and functioning of a large variety of systems, and its control is an enormous challenge that influences the safety and reliability of many technological applications (Brigham, 2010; Laforte *et al.*, 1998). The formation of ice on solid surfaces can cause massive damage in diverse areas such as transportation, power and communication systems, and offshore platforms. For instance, the ice accumulation on electric transmission lines can impede the safe transport of electricity, and operation of trains and telecommunication systems (Parent and Ilinca, 2011). Ice aggregation on the surface of aircraft wings affects performance and may significantly alter in-flight dynamics, potentially causing tragic accidents (Amirfazli and Antonini, 2017).

These problems necessitate the development of practical approaches that can prevent or slow ice formation on solid surfaces. The wide scope of applications listed above has motivated a large number of researchers to study the mechanisms of icing and develop techniques to mitigate icing from forming, i.e. anti-icing systems, which are discussed in further detail in section 2.1. Briefly, such techniques traditionally involved using either a) mechanical or thermal means, such as electro-impulse and thermal treatment, or b) anti-freezing chemicals aimed at additionally suppressing icing. These traditional "active" anti-icing techniques were often found to be inadequate, energy-consuming, expensive and potentially environmentally harmful.

The aforementioned limitations in active anti-icing techniques have led to extensive research on "passive" anti-icing systems based on *icephobic* surfaces using coatings that prevent ice build-up or reduce ice adhesion to the surface. However, before dis-

cussing how surfaces can be optimised to combat icing, it is necessary to clarify the definition of icing. Ice is merely water in the solid phase, and there are three paths to the formation of solid-phase water: i) vapour-solid desublimation, ii) vapour-liquid-solid freezing, and iii) direct liquid-solid freezing. In surface icing, the result of the first pathway is usually known as frost, and the result of the other two pathways is called ice. It is generally recognised that freezing is an intricate process where the mechanisms of ice nucleation and growth are related to the different phase transitions. Understanding icing therefore necessitates insight into the fundamental mechanisms of ice nucleation, which are detailed in section 2.2. There are a multitude of strategies that are being studied for icephobic surface design, which are detailed in section 2.3. For the anti-icing strategies to be improved, a better understanding of the ice nucleation process is needed at a microscopic level. Molecular dynamics (MD) is a key microscopic tool that is being used to give researchers a better scientific insights of these processes. Techniques for icing simulations using MD are presented in section 2.4. Finally, in section 2.5, this chapter summarises the information presented in this chapter, and introduces the contents of the next chapter.

## 2.1 Introduction to anti-icing systems

Conventional active anti-icing systems can be classified into three categories: i) de-icing systems with a cyclical function allowing partial ice formation, ii) thermal anti-icing systems, which maintain water in the liquid phase by heating areas of the surface where water impact is concentrated, and iii) evaporative anti-icing systems, which prevent the build-up of water in both liquid and solid phase in the water collection area and therefore avoiding the circulation of liquid water onto other areas. Even though such systems are very effective, they require high energy consumption. As a consequence, more efficient hybrid systems, which combine the active systems with icephobic surfaces, have gained popularity in recent years. Icephobic surfaces are characterised by their capability to delay or inhibit ice formation on a solid surface. The use of such surfaces in combination with active anti-icing systems can reduce energy consumption substantially. To increase the anti-icing performance while maintaining the high durability needed for long-term use in everyday applications, further study is required into: i) the physics of ice nucleation, ii) the thermodynamics of phase transition during ice formation on solid surfaces, iii) the surface chemistry, and iv) the surface structural analysis at the micro and nanoscales.

Recent research into icephobic surfaces can be classified into two primary areas of study. First, research has focused on developing icephobicity in a multi-faceted way, by trying to slow and/or prevent any one of the three steps relevant to ice formation, namely: i) reducing heterogeneous ice nucleation rate, ii) lowering ice adhesion, and iii) increasing the freezing delay, i.e. the time needed before supercooled water freezes on the surface (Kim *et al.*, 2012; Wilson *et al.*, 2013). Second, as hydrophobic materials are less vulnerable to water adherence, a class of non-wetting surfaces known as superhydrophobic surfaces have been used to design icephobic surfaces. Superhydrophobic surfaces hold off water through a combination of surface texture and chemistry. The expectation was that the high water-repellency due to the negligible contact area of water can enable liquid water-shedding before freezing and therefore also reduce the ice formation at the interface (Ramachandran *et al.*, 2016). To gain insight into developing icephobic surfaces using either of these approaches, studies have focused either on experimental testing in realistic icing conditions or on the basic science of water and ice interaction at the interface with a solid surface, mainly using molecular dynamics simulations. Regardless of the method employed, understanding the mechanisms of ice nucleation is key to icephobic surface design, and is elucidated in the next section.

## 2.2 Mechanisms of Ice Nucleation

The mechanism of ice nucleation is a stochastic process, influenced by various factors related to phenomena occurring at different time and length scales. This complicates the analysis of results from experiments, which have to be conducted under rigorous control of temperature, humidity, cooling rate, water purity etc. Thermodynamics states that, for atmospheric pressure conditions, ice phase is stable at $0^{\circ}$ C , while supercooled water is *metastable*, which is to say it can change phase under the right conditions. This metastable state can persist for a long time, however, if it is only subjected to minor disturbances. Metastability is related to the transition from a less ordered phase (liquid water) with high entropy to the highly ordered new phase (solid ice) at lower entropy. Therefore, the entropy of supercooled water must be reduced for ice formation to occur. This entropy requirement manifests as an energy barrier between the metastable state and the equilibrium state. To overcome the energy barrier, a driving force is required, which is the chemical potential difference between the solid and liquid phase, $\Delta\mu = \mu_s - \mu_l$, where $s$ and $l$ indicate the solid and liquid phase, respectively. In the case of liquid-to-solid phase change, the chemical potential is the

difference between the equilibrium freezing temperature, at a given pressure, and the effective freezing temperature at which phase change occurs, i.e. $\Delta T_s = T_f - T$. When this barrier is overcome, *nucleation* occurs, and a cluster of the solid phase forms within the supercooled liquid phase, in this case ice inside supercooled water.

Nucleation is classified into two categories: *homogeneous* and *heterogeneous* nucleation. Most natural nucleation processes are heterogeneous, which means that the stable phase grows on top of an external nucleation seed, such as impurities or a surface; by contrast, homogeneous nucleation takes place entirely in the bulk metastable phase (figure 2.1). The absence of a pre-existing nucleation seed in homogeneous nucleation implies that a cluster of the stable phase must develop spontaneously before the liquid can crystallise. This process requires overcoming a very high free energy barrier, and therefore homogeneous nucleation is an extremely rare event. Since the principal interest in this thesis is ice formation on solid surfaces, the focus will be on the fundamentals of heterogeneous ice nucleation. Homogeneous nucleation is only used to explain the basic concepts of classical nucleation theory, which is the most popular analytical model developed to characterise nucleation phenomena.

### 2.2.1 Classical Nucleation Theory

Classical Nucleation Theory (CNT) was first introduced by Volmer and Weber (1926) for droplet condensation of supercooled water vapour. Subsequent developments by Turnbull and Fisher (1949), Sunyaev (2014) and Becker and Döring (2006) enabled its application to crystallisation of supercooled liquids. Although simplifying assumptions are made in CNT, it does a remarkably good job at reproducing observed trends, and has compared well to molecular dynamics simulation results (Bai and Li, 2005). The main advantage of CNT is that the new phase of ice can be predicted to nucleate using measurable macroscopic quantities. According to CNT, clusters of crystalline atoms of any size are treated as macroscopic objects whose growth or collapse can be predicted using a simple set of equations, as discussed below.

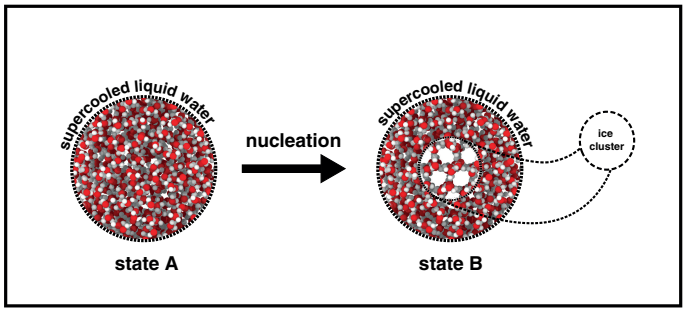


**Figure 2.1:** Homogeneous nucleation explained by presenting two states of a system. In state A the system is composed only of supercooled liquid water. In state B a cluster of water molecules in solid phase (ice embryo) is established within the supercooled liquid water.

### Homogeneous Ice Nucleation

CNT relies on the use of two fundamental concepts, which are introduced here: the Gibbs free energy barrier of freezing, $\Delta G_f$, and the rate of nucleation, $J$, associated with the kinetics of ice nuclei formation. In order to illustrate the Gibbs free energy barrier, we define two states, $A$ and $B$ of the same system (figure 2.1). State $A$ comprises only supercooled liquid water (metastable phase). In contrast, in state $B$, an unstable equilibrium between the supercooled liquid water and a cluster of water molecules in the solid phase (ice embryo) is established. To find the free energy barrier as the system is transformed from state $A$ to state $B$, the Gibbs free energy for each state at a constant temperature and a constant pressure is required. We can evaluate the Gibbs energy of state $A$ as (Atkins and De Paula, 2006):

$$G_A^l = \mu_A^l N, \tag{2.1}$$

and that of state $B$ as:

$$G_B^{l+i} = \mu_B^l N^l + \mu_B^i N^i + \gamma\alpha, \tag{2.2}$$

where $\mu_A^l$ and $\mu_B^l$ are the chemical potential of liquid molecules in states $A$ and $B$, respectively; $\mu_B^i$ is the chemical potential of ice molecules in state $B$; $\gamma$ is the ice-water interfacial tension; $\alpha$ is the surface area of the ice embryo; $N$ and $N^l$ are the numbers of liquid molecules at state $A$ and $B$, respectively; and $N^i$ is the number of ice water molecules.

We assume that the ice embryo is separated from supercooled water by a sharp boundary and that it is sufficiently macroscopic that we can use the Gibbs capillarity approximation (Kelton, 1991) from classical thermodynamics; the Gibbs approximation

states that the interior of the nucleus, despite consisting of very few molecules, can be assumed to have the same properties as the bulk phase. The total number of particles is thus $N = N^l + N^i$. We can then rewrite equation (2.2) as:

$$G_B^{l+i} = \mu_B^l N + (\mu_B^i - \mu_B^l)N^i + \gamma\alpha. \tag{2.3}$$

We can also assume that $\mu_B^l = \mu_A^l = \mu_A$, which is valid because the chemical potential of a phase is a function of the temperature and pressure only. The change of Gibbs free energy in the transition (freezing) from state $A$ to state $B$ is:

$$\Delta G_f = \Delta G_B^{l+i} + \Delta G_A^l = N^i \Delta\mu + \gamma\alpha, \tag{2.4}$$

where $\Delta G_f$ is the Gibbs free energy barrier of freezing, and $\Delta\mu = \mu_i - \mu_l$. Assuming the ice embryo is incompressible, equation (2.4) can be written in terms of its volume (Ruckenstein and Djikaev, 2005), and we get $N = \rho V$, where $\rho$ is the number density. This gives:

$$\Delta G_f = \rho_i V_i \Delta\mu + \gamma\alpha. \tag{2.5}$$

If we further presume that the ice embryo is spherical with radius $r$, the change in Gibbs free energy results in:

$$\Delta G_f = -\left(\frac{4\pi}{3}\right) r^3 \rho \Delta\mu + \gamma 4\pi r^2. \tag{2.6}$$

Since the solid phase (ice embryo) is more stable than that of the liquid phase, $\Delta\mu < 0$. $\Delta G_f$ is thus the sum of two terms: i) a negative volume term, driving towards phase change, and increasing with the volume of ice embryo and ii) an opposing positive surface term, related to the energy needed to produce a new water-ice interface $\gamma 4\pi r^2$, where $\gamma$ is the ice-liquid water interfacial tension.

$\Delta G_f$ is a function of $r$, and by differentiation, we can find that the surface term is dominant up to a critical ice embryo radius $r_{\text{crit}} = 2\gamma \Big/ \rho^i \Delta\mu$, where $\Delta G_f^* = 16\pi\gamma^3 \Big/ 3(\rho^i \Delta\mu)^2$ reaches its highest value. This means that below $r_{\text{crit}}$, an ice embryo is not stable and is required to surmount this critical value to grow further (figure 2.2).

Taking into account that the chemical potential $\Delta\mu$ is proportional to the latent heat of freezing $h_f$, and degree of liquid supercooling $\Delta T_s$, we can write $\Delta\mu = h_f \, \Delta T_s / T_f$. As a result, the growth of ice embryo requires overcoming the critical Gibbs free energy

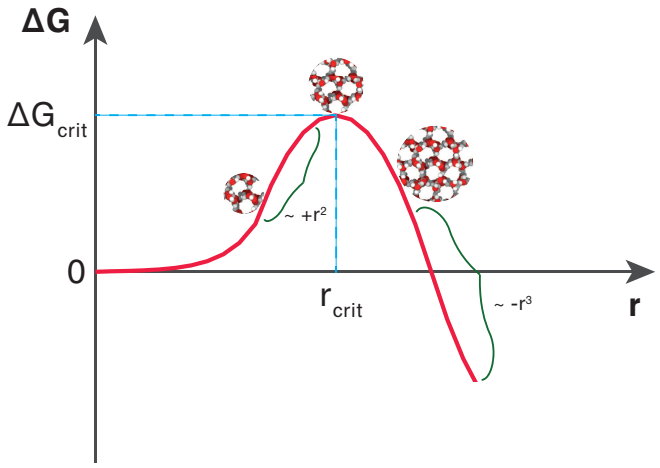


**Figure 2.2:** Change in Gibbs free energy $\Delta G$ as a function of ice embryo radius $r$. The ice embryo is metastable below a critical radius $r_{\text{crit}}$, while freezing takes place when $r > r_{\text{crit}}$ and the free energy barrier $\Delta G_{\text{crit}} = \Delta G_f^*$ is overcome.

barrier, which is expressed as:

$$\Delta G_f^* = \frac{16\pi\gamma^3}{3h_f^2\left(\frac{\Delta T_s}{T_f}\right)^2}. \tag{2.7}$$

Equation (2.7) indicates that the larger the supercooling, the easier it is for the ice embryo to surmount the barrier and grow. Also, it explains why $\Delta T_s$ is a driving force for ice nucleation.

The ice nucleation rate, $J$, is the rate at which molecules are accumulated as part of the ice embryo and consequently is an estimate of the probability per unit time, per unit volume of forming a critical nucleus. This estimation assumes that there is no correlation between successive events increasing or decreasing the number of molecules of the ice embryo. Also, it is supposed that the most active nucleation site dominates ice nucleation; once an ice cluster overcomes the critical size, ice formation in the liquid continues spontaneously. If these conditions are met, $J$ does not depend on the time and is given by the following expression:

$$J \approx \frac{k_B T}{h} \exp\left(\frac{-\Delta G_f^*}{k_B T} - \frac{\Delta g_{\text{act}}}{k_B T}\right), \tag{2.8}$$

where $k_B$ is the Boltzmann constant, $h$ is Planck's constant and $\Delta g_{\text{act}}$ is the activation

energy barrier associated with the transfer of water molecules across the ice-water interface.

Equation (2.8) reveals two crucial aspects of ice nucleation. First, the ice nucleation rate is strongly (exponentially) dependent on temperature. Thus, an increase of 1 K in supercooling increases the ice nucleation rate by 2-3 orders of magnitude. Second, the two terms in the exponent indicate the existence of two energy barriers; the first term is associated with the Gibbs free energy barrier and the second term is related to $\Delta g_{\text{act}}$, an energy barrier connected with self-diffusion in water. The activation energy barrier takes into account the reduced mobility of molecules at the interface, which delays the transport of molecules leaving the liquid phase and joining the solid phase. For low supercooling ($\Delta T_s < 30$ K), $\Delta g_{\text{act}}$ has a negligible effect, and ice nucleation can be considered a one-step mechanism with nucleation rate given by:

$$J \approx \frac{k_B T}{h} \exp\left(\frac{-\Delta G_f^*}{k_B T}\right). \tag{2.9}$$

For high supercooling ($\Delta T_s > 30$ K), the second term needs to be included as well, and ice nucleation is considered to be a two-step mechanism.

### Heterogeneous Ice Nucleation

The most common way in nature for ice to form is through heterogeneous ice nucleation, which occurs when the water is in contact with foreign material. It can take place at temperatures higher than that of homogeneous nucleation, because of the impurities that act as nucleating agents and facilitate the formation of critical ice nuclei. From a thermodynamic standpoint, heterogeneous ice nucleation occurs due to a decrease in energy barrier needed for freezing. Therefore, the energy barrier for heterogeneous nucleation will be smaller than that of the homogeneous freezing barrier, i.e.:

$$\Delta G_{f,\text{het}}^* < \Delta G_{f,\text{hom}}^*. \tag{2.10}$$

The presence of nucleation drivers on a surface favour heterogeneous nucleation. These drivers can result from surface characteristics, such as topography and chemical composition. Therefore, when designing icephobic materials, all the aforementioned factors should be taken into consideration. To account for surface effects, the heterogeneous nucleation barrier is commonly expressed as (Lamb and Verlinde, 2011; Mason,

1954):

$$\Delta G^*_{f,\text{het}} = f\left(\cos\theta_{iw}, \frac{r}{r_i^*}\right)\Delta G^*_{f,\text{hom}}, \tag{2.11}$$

where $f$ is described analytically by:

$$f\left(\cos\theta_{iw}, \frac{r}{r_i^*}\right) = 1 + \left(\frac{1-\cos\theta_{iw}\frac{r}{r_i^*}}{g}\right) + \left(\frac{r}{r_i^*}\right)^3\left[2 - 3\left(\frac{\frac{r}{r_i^*}-\cos\theta_{iw}}{g}\right) + \left(\frac{\frac{r}{r_i^*}-\cos\theta_{iw}}{g}\right)^3\right] + 3\cos\theta_{iw}\left(\frac{r}{r_i^*}\right)^2\left(\left(\frac{\frac{r}{r_i^*}-\cos\theta_{iw}}{g}\right) - 1\right). \tag{2.12}$$

Here, $f$ accounts for surface wettability and texture through the ice-water contact angle, $\theta_{iw}$; the surface radius of curvature $r$, non-dimensionalised through the critical ice embryo radius $r_i^*$, and the function $g = \left(1 + \left(\frac{r}{r_i^*}\right)^2 - 2\cdot\cos\theta\cdot\frac{r}{r_i^*}\right)^{1/2}$. Equation (2.12) predicts that the value of $f$ varies from 0 to 1 and thus, $\Delta G^*_{\text{het}}$ varies from 0 to $\Delta G^*_{\text{hom}}$.

Equation (2.11) is the best theoretical estimate of heterogeneous nucleation and provides comprehensive information of the factors influencing both homogeneous and heterogeneous nucleation. Equation (2.12) indicates that the icephobic performance of a surface can be modified by tuning characteristics, such as topography, crystal structure and chemical composition, in such a way to modify the interfacial tension and contact angle. This information is useful when analysing ice nucleation experiments involving water on surfaces, and evaluating the potential icephobic performance of a surface.

### Shortcomings of classical nucleation theory

One of the most significant advantages of classical nucleation theory is its simplicity. As a consequence, its predictions are not always in agreement with experimental results. A significant criticism directed to CNT is the application of bulk thermodynamic properties to microscopic systems is not accurate. For example, the theory's prediction for the height of the free energy barrier, given by equation (2.7), varies as $\gamma^3$. Therefore, a small change of the interfacial tension of ice-water $\gamma$, leads to significant variation of the free energy barrier. Also, according to the capillary approximation, ice embryos have a spherical shape, while in reality, this is not always true. Depending on shape, the value of interfacial ice-water tension $\gamma$, assumed by CNT, can differ from the

actual value. Several improvements on CNT have been proposed for specific cases, in the form of corrective factors to the CNT equations; moreover, several alternative phenomenological, kinetic and microscopic theories have been developed (Reinhardt, 2013). However, due to its simplicity and accuracy, CNT continues to be a popular framework for the design and analysis of experimental and theoretical work on ice nucleation.

## 2.3 Anti-icing strategies

The discussion on CNT in the previous section provides some insight into passive icephobic surface design. The use of CNT has produced a significant literature aimed at improving surface icephobicity by trying to manipulate the surface characteristic terms in equations (2.11) and (2.12). Early studies in this area were primarily experimental in nature (Jung *et al.*, 2011; Varanasi *et al.*, 2010), but the analysis of results proved challenging. This is because, in addition to the stochastic character of icing, there are difficulties linked to water impurities and heterogeneities of surfaces, which can significantly influence data reproducibility (Zhang and Liu, 2018).

It has been shown that the freezing delay time can be considerably increased given that the system temperatures are slightly higher than the nucleation temperature (Maitra *et al.*, 2014; Schutzius *et al.*, 2015). The median freezing delay time can be expressed as (Li and Guo, 2018):

$$t_{\text{med}} = \left(\frac{5\ln 2}{3J_0}\right)^{3/5}, \tag{2.13}$$

where $J_0 = Jt^{-2/3}$ and $J$ is the nucleation rate. Therefore, the freezing delay time is inversely proportional to the nucleation rate $J$, which according to equation (2.8) depends exponentially on the degree of supercooling. As a consequence, even a relatively small reduction of nucleation temperature may extend the freezing delay time significantly.

Given the complexity of the physical phenomena involved in icing, results from different experiments may not be comparable and can even appear contradictory due to small differences in experimental conditions; for example, the presence of chemical heterogeneities can make it harder to isolate the effect of surface roughness (Nosonovsky and Hejazi, 2012). However, at the same time, many research papers (Eberle *et al.*, 2014; Li and Guo, 2018) indicate that a modest change of the surface morphology could result in large changes in nucleation rates, highlighting the effect of atomic-scale processes

on nucleation and the need for its systematic study at the molecular level. Therefore, while there are challenges in designing icephobic surfaces, there is also strong potential for future developments.

Nucleation mechanisms take place in nano-to-microsecond time scale and length scales of few hundred to thousand molecular diameters. These are difficult to investigate in experiments. In principle, the scales of these mechanisms are ideal for MD simulations. As a result, several computational studies provide valuable information about various factors affecting ice nucleation, such as surface wettability, interfacial structure and interfacial dynamics. Using this information, experiments may be able to improve their design, achieving more reliable performance. Similarly, experimental results can lead to better targeted and useful simulations. This bridging of experiments and molecular simulations is gaining momentum because of recent progress in both micro/nano-fabrication and the increasing computational power of MD.

### 2.3.1 Basic characteristics for icephobic surfaces

As previously stated, researchers had originally assumed that icephobicity and hydrophobicity are closely related, and numerous icephobic coatings were originally derived from hydrophobic or superhydrophobic coatings (Huang *et al.*, 2019). Superhydrophobic surfaces (SHS), under appropriate modifications, can combine high water repellence with low ice adhesion and decreased nucleation rate (Mishchenko *et al.*, 2010; Momen *et al.*, 2011; Saleema and Farzaneh, 2008; Sarkar *et al.*, 2008). However, there has been disagreement reported on the anti-icing performance of SHS. It has been shown that anti-icing efficiency of SHS depends on diverse factors and conditions (Farhadi *et al.*, 2011; Zhou *et al.*, 2012), and occasionally can be significantly reduced in humid conditions (Jung *et al.*, 2011; Varanasi *et al.*, 2010).

Given these developments, there still exists no unique recipe for icephobicity, and further understanding requires the evaluation of many parameters such as the surface structure and the dynamics of water near the surface (Sojoudi *et al.*, 2016). These parameters are interrelated and it is difficult to distinguish between cause and effect. This section will summarise the current limitations as well as the future potential of anti-icing strategies, by highlighting a few relevant parameters relevant to icephobicity.

### Surface wettability

The wettability of solid surfaces has a significant influence on its icephobic behaviour. Wettability can be estimated by quantifying the contact angle ($\theta$) of a water droplet on a surface of interest (figure 2.3). For a surface to be characterised hydrophilic, it has to have a contact angle of $\theta < 90^\circ$. If $\theta > 90^\circ$, then the surface is considered hydrophobic. Superhydrophobic surfaces have contact angles with $\theta > 150^\circ$, where water droplets form beads that roll off these low-wetting surfaces. Such a high degree of water repellence is usually achieved by a combination of surface topography and low surface energy. Referring to the previous section, note that the free energy required for heterogeneous nucleation approaches zero with increasing wettability since:

$$\lim_{\theta \to 0} f(\theta) = 0. \tag{2.14}$$

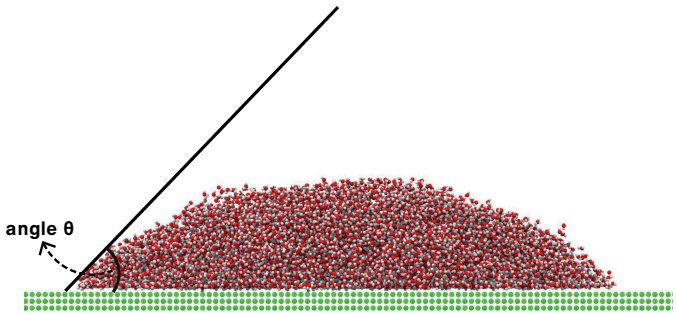


**Figure 2.3:** A water droplet on top of a solid surface, where the contact angle $\theta$ is a measure of the surface's wettability. The energy barrier for ice nucleation $\Delta G^*$ decreases with increasing wettability or decreasing contact angle $\theta$.

Hence, according to equation (2.12), a large contact angle requires a higher free energy $\Delta G^*$ for nucleation, which means a greater degree of supercooling. However, the influence of wettability is more complex since the ice nucleation rate $J$ does not depend only on $\Delta G^*$, as mentioned in section 2.2.1. Li *et al.* (2014) experimentally investigated the freezing behaviour of water on two smooth surfaces, one hydrophilic and one hydrophobic. Reported values of contact angles were $\theta = 55^\circ$ on the hydrophilic surface and $\theta = 114^\circ$ for the hydrophobic surface. They observed the ice nucleation temperature to be slightly lower for the hydrophilic surface when compared to the hydrophobic one. At first, this outcome seemed surprising, since it was expected that

hydrophobicity should make freezing unfavourable. However, this incongruity was resolved when the interface was studied closely, and a layer of interfacial liquid water was observed (Goertz *et al.*, 2007). Li *et al.* (2014) demonstrated that the viscosity of the interfacial liquid water was higher on the hydrophilic surface than that on the hydrophobic one. The increased viscosity on hydrophilic surfaces decreased the self-diffusion coefficient $D$ of water molecules at the interface, leading to a decrease of the activation energy barrier $\Delta g_{\text{act}}$ (which becomes relevant for $\Delta T_s > 30$ K) and consequently to a decrease in the nucleation rate $J$. The scope of this discussion is a demonstration that the influence of surface wettability on ice formation is not straightforward.

Compared to its bulk, surface energy is a measure of the overabundant energy present on a material's surface. Wetting and adhesion between materials may be determined using the surface energy. Surface energy is correlated with the strength of interactions in bulk and the size of the surface exposed. If the bulk interactions or the surface exposure are large, surface energy would also be high. The surface energies of liquids are usually lower than that of solid materials since the forces between their molecules are weak, and as a result liquids typically spread. As a first approximation, surface energies can be evaluated if the internal interactions in the solid can be estimated (Jiang *et al.*, 2020; Liu *et al.*, 2017). Poor wetting of a surface is caused because of its 'low' surface energy and thus, high contact angle. Low surface energy means that the surface cannot form strong bonds with the liquid, so the liquid has no energetic reward for breaking its bulk bonding in favour of surface interaction. The opposite is when a surface has 'high' surface energy, which means that it has good wetting and a low contact angle. In addition to surface energy, the topography of the surface also plays a key role in determining wettability. Indeed, many hydrophobic and superhydrophobic surfaces rely on a combination of surface energy and topography, as discussed below.

**Superhydrophobicity**

Water repellence as a phenomenon has been observed and systematically studied in nature, on the surfaces of many leaves and insect body parts (Gao and Jiang, 2004; Zheng *et al.*, 2007). One well-known case is the lotus leaf surface, for which the mechanism is also called the "lotus effect" (Barthlott and Neinhuis, 1997). Such a mechanism is the result of a combination of rough surface topography (typically micro- and nano-texturing) and low surface energy. Two extreme cases, namely Cassie-Baxter (CB) and Wenzel states, are commonly used to characterise wetting behaviour. The Wenzel state (figure 2.4a) assumes that the water droplets form a continuous wetting

interface matching the topography of the solid surface. Water droplets in this state exhibit low mobility because the contact area is large, which allows them to adhere to the surface. In contrast, water droplets in the CB state (figure 2.4b) only bind partly to hydrophobic surfaces and instead lie on a composite interface. Water droplets therefore have a reduced contact area with the solid surface, and therefore exhibit higher mobility. As mobility is linked to both ice nucleation and adhesion, surface topography in principle could play a role in the reduction of nucleation temperature, freezing delay and nucleation rate.

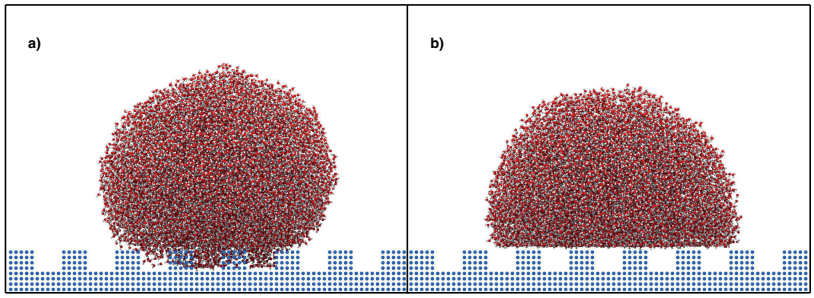


**Figure 2.4:** a) Wenzel's wetting state b) Cassie-Baxter wetting state.

An initial study conducted by Eberle *et al.* (2014) indicated that nanotextured surfaces, spanning a wide range of root-mean-square roughness from 0.1 nm to 100 nm, have a constant nucleation temperature of $\sim$ 249 K. At first glance, this result seems to suggest that surface roughness does not play a role in nucleation. However, Eberle *et al.* (2014) also observed that hierarchical structures with micro *and* nanotexturing showed a lower freezing temperature than the corresponding nanotextured surfaces. There are other studies which show a direct link between surface roughness and surface icing characteristics (Guo *et al.*, 2012).

### Interfacial Region

Another challenging problem that is potentially tractable for MD simulations is the interfacial region characterisation. Unique surface-induced molecular configurations in the interfacial region have also been shown to be key to minimising ice adhesion; examples include: a) a region of reduced density (up to $\sim$1.5 Å thick for self-assembled monolayers (Björneholm *et al.*, 2016)) sometimes referred to as the density-depleted layer (DDL), can form near smooth hydrophobic surfaces (Chattopadhyay *et al.*, 2010), and b) a nm-thick quasi-liquid layer (QLL) has been observed in simulations involving generic crystal surfaces, analogous to the lubricant layer on slippery low surface

energy surfaces. Experiments have shown that the formation of DDL or QLL results in extremely low ice adhesion stress values, far lower than what surface-energy models predict (Chen *et al.*, 2017a). Thus, novel icephobic surfaces can be designed by better understanding of how to induce adhesion-minimising configurations within this nanoscale interfacial region. While the understanding of interfacial region structure has advanced in recent years mostly through experimental studies (Golovin *et al.*, 2016; He *et al.*, 2020), its influence on icephobicity is still not fully understood. Given the limitations of experimental studies, molecular simulations provide a useful alternative tool to reveal nanoscale insights into the structure and dynamics of this region, and probe into the formation of DDL and QLL. Here, the focus will be on the latter, given its key role in icephobic surface design.

In principle, an interface between different phases presents sharp transition properties, changing through a strong, but finite, gradient. A disordered phase will exist and the reduction of the excess total free energy leads to the formation of an intermediate layer of thickness $T_{\mathrm{QLL}}$. The postulation of the QLL can be traced back to Faraday (Faraday, 1859) who observed, even in freezing temperatures, a sheen of liquid water on the ice surface when conducting experiments involving the freezing of two ice cubes in contact. It gained new interest in the 1960s, when Jellinek (1961) performed ice adhesion tests on different surfaces, testing both tensile and shear stresses, and estimated the thickness of QLL in the order of 10 nm and its viscosity ranging several orders of magnitude higher than bulk water. The role of QLL on freezing has been studied in the context of anti-icing strategies (Amirfazli and Antonini, 2017; Jha *et al.*, 2016). Tests performed by Meuler *et al.* (2010), using various combinations of coatings comprising polyethylene glycol (PEG), strongly exhibit reduced ice adhesion. They concluded that this is due to the presence of unfrozen water molecules at the PEG interface, as PEG is known to hydrogen bond with water molecules. These bonded water molecules form a QLL that serves as a lubrication layer at the ice-surface interface, and therefore reduces ice adhesion (Dash *et al.*, 2006; Zeng and Li, 2019). It has been suggested that QLL impedes ice nucleation and growth in proportion to its thickness and dynamics. These results imply a new regime for designing anti-freezing coatings, in which the thickness and dynamics of QLL are of crucial importance.

The thickness of QLL depends on various factors such as temperature and type of interface (Qiu and Molinero, 2018). Several studies on QLL employed experiments, including X-ray and electron scattering, ellipsometry and Atomic Force Microscopy (AFM) (Björneholm *et al.*, 2016; Shultz, 2017). However, their results present large

uncertainties and little consensus (Li and Somorjai, 2007). This is due to the difficulties involved in: a) probing nanoscale molecular features in experiments, and b) isolating pristine surfaces experimentally (Limmer, 2016). Indeed, ice impurities will have an influence on QLL thickness measurements. Using AFM, Döppenschmidt and Butt (2000) compared the QLL thickness of pure ice with ice containing 10 mM of KCl, and showed that the QLL was substantially thicker on the contaminated ice surface. Depending on the measurement procedure, the QLL thickness might vary by up to three orders of magnitude at a given temperature (Zeng and Li, 2019). Given the length scale of the QLL and the difficulty of comparing results from different studies, molecular simulations can be a valuable tool for gaining molecular insight into QLL properties as well as assisting in the interpretation of experimental data.

Kling *et al.* (2018) addressed the molecular structure and also the dynamics of the QLL at the ice-vapour interfaces as a function of temperature by MD simulations. Their results show significant deviations between 2D QLL and bulk water, stemming the impact of the adjacent bulk ice layers. In addition, they indicate the ice surface can be characterised by considering both its structural and dynamical properties.

### Ice Adhesion

Another approach to icephobicity is to develop surfaces that minimise ice accretion or/and exhibit minimal ice adhesion strength. In the latter case, the essential idea is that while ice could build-up as a result of liquid water freezing, ensuring low ice adhesion would mean that the formed ice could be removed by external forces without needing additional energy. Gao and McCarthy (2008) and Meuler *et al.* (2010) have shown that a linear relationship exists between ice adhesion and the work of adhesion, which is given by:

$$W_{\text{adh}} = \gamma\left(1+\cos\theta_R\right), \tag{2.15}$$

where $\gamma$ is the surface tension of the liquid droplet and air, and $\theta_R$ is the receding water droplet contact angle. Using smooth materials, they find that hydrophobicity correlates well with icephobicity when assessed in terms of ice adhesion. However for textured surfaces, equation (2.15) is misleading, since other factors, such as surface roughness, may influence the results of ice adhesion tests. Varanasi *et al.* (2010) investigated the ice adhesion strength on micropillar-textured surfaces and concluded that it was higher than that of a smooth surface of the same materials. Comparing the ice adhesion values from textured surfaces suggested that ice was infiltrating the micropillars, and thus ad-

hering to all available area of the textured surface, which is much greater than a smooth one. This is why, as stated earlier, the relationship between superhydrophobicity and ice adhesion remains an open question.

Chen *et al.* (2013) demonstrated that a hygroscopic coating on a solid interface could liquefy and expand due to water absorption, enabling the development of a self-lubricating liquid water layer at the interface, even in freezing conditions. Adhesion measurements showed that the presence of this layer led to the reduction of ice adhesion by one order of magnitude. An alternative anti-icing approach consists of employing an anti-adsorption layer, by the formation of a liquid layer with low surface tension, impregnating the surface roughness. In this approach, a liquid layer is infused into a micro/nanostructured surface texture. This strategy is inspired by nature and is based on the concept of slippery-liquid-infused porous surfaces (SLIPS) and liquid impregnated surfaces (LIS) (Kim *et al.*, 2012; Rykaczewski *et al.*, 2013; Wong *et al.*, 2011). An advantage of these surfaces is the reduced risk of liquid degradation into the textured surface, since the infused lubricating fluid layer is much more difficult to be displaced than a gas layer. However, it has been shown that gravity can lead to drainage of the infused liquid layer. Consequently, leakage of the infused lubricant fluid can take place over time, rendering these surfaces only effective for limited periods of time, which represents a serious drawback for icephobic applications. Note that this information is provided for reference and ice adhesion is not studied in this thesis.

#### Advances in experimental studies of anti-icing approaches

In addition to the common icephobic strategies mentioned previously, several different experimental approaches have been employed to understand the microscopic mechanisms of freezing. Given that ice nucleation is a dynamic process taking place on a very small length and time scales, the experimental problems are hard to solve because these spatial and temporal scales are challenging to resolve. Some microscopic experimental approaches aim at analysing a large number of independent nucleation events for a whole set of small configurations of the system, and taking an ensemble average. Icing is determined for each nucleation event within the ensemble of obtainable configurations by methods like optical microscopy (Campbell *et al.*, 2015; Li *et al.*, 2012) and femtosecond X-ray (Sellberg *et al.*, 2014). The results of these techniques can be analysed in the framework of CNT and can give estimations of the nucleation rate by measuring the induction time, which is the time taken for ice nuclei to reach a detectable size (Lindenberg and Mazzotti, 2009; Roelands *et al.*, 2004).

Another approach is to use Fourier transform infrared spectroscopy (FTIR) (Bhabhe *et al.*, 2013) and Differential Scanning Calorimetry (DSC) (Davies *et al.*, 2009; Özilgen and Reid, 1993) to analyse larger macroscopic systems. Through these methods, the nucleation temperature can be obtained, and in some cases, the nucleation rate as well (Yang *et al.*, 2008). The emergence of such a large number of microscopic experimental techniques, even with significant limitations, is promising; the bridging of microscopic experimental approaches of icephobicity with corresponding MD simulations remains a key scientific challenge.

## 2.4 Molecular Dynamics Simulation

### 2.4.1 Motivation

Despite improvements in experimental capabilities, it is still extremely difficult to quantify the influence of a variety of factors on the ice nucleation experimentally. MD simulations can complement the experiments, offering alternative means of extracting scientific insights. One of the most critical challenges faced when investigating ice nucleation is to evaluate the impact of the surface structure and the water-surface interface on the ice growth. High-fidelity computer simulations are an essential tool to better understand ice formation and growth at the nanoscale.

Atomistic simulations also provide a bridge between models and accurate descriptions of physical systems, as well as the molecular understanding of the observations in experiments. To be more specific, key parameters that regulate a phenomenon observed in experiments could be isolated with the use of full atomistic simulations. Therefore, MD simulations can disentangle the influence of the parameters and improve the design of new experiments. The rest of this section will focus on research into surface icing using MD simulations.

### 2.4.2 MD simulations of water freezing

Ice nucleation is influenced by several independent factors, such as hydrophobicity (Cox *et al.*, 2015b; Lupi and Molinero, 2014), surface morphology (Cox *et al.*, 2012) and charge distribution (Glatz and Sarupria, 2016). A comparative evaluation of experimental results and computer simulations of ice nucleation indicated that surfaces with a high number of defects at the interface have higher ice nucleation rates (Zhang and Liu,

2018). The objective of many MD simulations of ice nucleation is to find and quantify the relation between ice nucleation rate and the different molecular properties, such as water-surface interactions and surface morphologies. As such, early computational investigations focused on clarifying how a surface affected the first layers of water.

Pruppacher and Klett (1997) summarised the requirements of a good ice nucleation agent (INA). Referring to a solid surface, these are:

1. *Hydrophobicity or chemical bond requirement* — Given that water molecules form ice crystals through hydrogen bonds, it is logical to deduce that ice nucleation will be favoured at surfaces having available similar hydrogen bonds.
2. *Crystallographic requirement* — The closer the crystallographic matching of the surface to ice, the better its ice-nucleating ability.
3. *Active site requirement* — Three types of active sites can be distinguished: i) morphological surface inhomogeneities, including corrugations, cracks or cavities at the surface; ii) chemical inhomogeneities in the surface, usually originated by the presence of foreign ions that are hydrophilic to the rest of the solid surface; and iii) electrical inhomogeneities, such as sharply delimited boundaries between surface regions of different electric field signs.

Although the criteria listed above can be instrumental in identifying whether a surface promotes or inhibits ice nucleation, in many cases these criteria fall short. For instance, the widely accepted notion that ice nucleation agents have surfaces similar to the surface of ice has recently been questioned (Pedevilla *et al.*, 2016), and even amorphous surfaces may act as good ice nuclei (Bi *et al.*, 2016). Recent studies suggest that a surface's ice nucleation ability depends on the interplay of more surface characteristics and cannot be explained by a sole criterion (Cox *et al.*, 2013; Dai *et al.*, 2017; Fitzner *et al.*, 2015; Glatz and Sarupria, 2016, 2018; Lupi *et al.*, 2014).

### 2.4.3 Molecular dynamics of heterogeneous ice nucleation

MD simulations evolve the physical system dynamically in time by numerically integrating Newton's equations of motion (Frenkel and Smit, 2001). MD has an essential advantage over alternative approaches in that it observes the "natural" dynamics of the system. The most direct way to study the heterogeneous ice nucleation is by the so-called *brute-force* MD simulations, which demand cooling the system to below the freezing temperature and then tracking its time evolution until nucleation occurs.

Ice nucleation studies using MD simulations are commonly performed in the isothermal-

isobaric ensemble (NPT), where the pressure $P$ and the temperature $T$ are kept constant through a barostat and thermostat, respectively (see section 3.1.3). Nucleation is an exothermic process, and heat is produced when water freezes. However, within the length scale probed by atomistic simulations, this heat development is neglected due to the use of a thermostat. The determination of the ice nucleation rate from brute-force MD simulation requires the satisfaction of the following conditions:

1. the system must evolve in time until spontaneous fluctuations lead to a nucleation event;
2. the system size must be much larger than the critical ice nucleus;
3. a sufficient number of nucleation events must be realised in order for statistical inference to be enabled.

The first of these conditions is very challenging because as nucleation is a rare event, its occurrence requires a very long simulation time, which depends on the amount of supercooling $\Delta T_s$. According to the published experimental results performed under moderate supercooling, a single nucleation event within a volume of a reasonably-sized computational domain of $50 \times 50 \times 50$ Å$^3$ would take a simulation time of the order of $10^4$ years in a brute-force simulation (Sosso *et al.*, 2016a). Brute-force simulations are therefore unlikely to be successful, at least at supercooling comparable to the ones examined in the majority of experiments. Furthermore, nucleation is a stochastic event, and therefore to obtain the nucleation rate, the collection of a large number of events is needed, which is computationally expensive.

In the literature, research studies in which brute-force simulations have been successfully performed usually use monoatomic coarse-grained models, such as the mW water model (Bianco *et al.*, 2017). The fast dynamics of this simple water model, enabling the use of large numerical timesteps, is the main reason why this model is computational efficient and feasible. However, these models neglect the explicit description of the hydrogen atoms and the incorporation of long-range electrostatic interactions, which are critical to obtaining correct simulation results for different phases (Molinero and Moore, 2009). Nucleation studies with more accurate but computationally demanding all-atom water models, like TIP4P/2005 (Abascal and Vega, 2005) and TIP4P/Ice (Abascal *et al.*, 2005), are challenging because while being more accurate, their dynamics are intrinsically slower than that of coarse-grained models. Therefore, unbiased brute-force simulation studies, using rigid all-atom water models, are being conducted for a limited range of unrealistic surfaces, with carefully chosen surface morphology and/or charge distribution designed to strongly promote ice nucleation (Glatz and

Sarupria, 2016, 2018; Li *et al.*, 2017; Zielke *et al.*, 2016).

All-atom water models can be successfully incorporated in enhanced sampling methods (Yang *et al.*, 2019), which are an alternative to brute-force methods. Enhanced sampling modifies how the system searches its configurational space, and so, nucleation events can be recorded in a much shorter computational time. Of the various enhanced sampling methods, only a few have been successfully applied to calculate ice nucleation rates. When dealing with ice nucleation in supercooled water, free-energy based methods are used, such as metadynamics (Barducci *et al.*, 2008; Laio and Gervasio, 2008) and umbrella sampling (Kumar *et al.*, 1992; Torrie and Valleau, 1977). In almost all enhanced sampling methods, the free energy surface of the system is coarse-grained through one or more order parameters, which is the way of measuring the degree of order in a phase transition system. The application of an external bias potential leads to a modified sampling of the configurational space that enables the computation of the free energy barrier.

Even with the current state-of-the-art free energy methods and advanced sampling techniques, ice nucleation is difficult to simulate due to the slow dynamics of the hydrogen bond network (HBN) within the supercooled water. That makes it very difficult for methods such as metadynamics and umbrella sampling to equilibrate the system as it is advanced along with the chosen order parameter (Reinhardt *et al.*, 2012). Nevertheless, the determination of the free energy barrier is only part of the problem. For the nucleation rate to be obtained, additional methods are needed. These methods usually aim at estimating the probability for the system that reached the nucleation barrier, to evolve into the crystal. Often, such methods require a broad set of MD or kinetic Monte Carlo (KMC) simulations to be performed. The most significant disadvantage of the free energy methods is that they require *a priori* knowledge of the process to define useful order parameters, which is challenging for ice nucleation simulations.

Another option to simulate ice nucleation is by path sampling methods, which can provide direct access to the kinetics of the process. Many different path sampling methods are available, including forward flux sampling (FFS) (Allen *et al.*, 2006, 2009) and transition path sampling (TPS) (Bolhuis *et al.*, 2002; Dellago *et al.*, 2006). TPS methods focus on the transition of a system from a stable state $A$ to a stable state $B$. There are many pathways to this transition and a probability can be assigned for each of them. This can be generated by the ensemble of all transition paths, which compromise all relevant information, such as the transition states and the rate constants.

TPS provide algorithms that can gradually sample the transition ensemble through an iterative procedure. The primary advantage of TPS methods is that they tend to be less sensitive to the choice of order parameter used, and since the Hamiltonian of the system is not modified, the dynamics remains unperturbed, and there is no additional biased potential.

Under certain conditions, path sampling approaches can provide insight into the nucleation mechanism. However, they present high sensitivity to the slow dynamics of highly supercooled systems, which impede the sampling of the paths and immensely increase the computational cost of the simulation. The high computational costs, in unison with the sensitive choice of the order parameter and the underlying framework of CNT, render enhanced sampling simulation of ice nucleation a daunting challenge.

In the last few years, an alternative approach referred to as "seeding", has been used to study nucleation (Espinosa *et al.*, 2016b; Knott *et al.*, 2012; Pereyra *et al.*, 2011; Sanz *et al.*, 2013), to overcome the limitations of coarse-grained and enhanced sampling methods. Seeded MD simulations involve introducing ice nuclei of different sizes into supercooled liquid water prior to starting the simulation (Pedevilla *et al.*, 2018). At a specific temperature, these ice "seeds" would dissolve or grow respectively, enabling the determination of the critical nucleus size. The microscopic information of the critical cluster obtained using seeded simulations is combined with CNT to get estimates of the nucleation rate. This approach is quite simple to implement and allows the estimation of the nucleation rate in mild supercooling. However, it does not provide direct information about the actual nucleation mechanism, and it relies on the validity of both an *a priori* conceived nucleation pathway, the one dictated by the inserted seed, and of CNT.

Finally, the kinetics of ice growth has been investigated by another type of MD seeding approach, in which pre-built patches of water and ice were put together to create an interface. The necessity to simulate the improbable creation of the crystallisation nucleus thus can be avoided. A similar set-up has been used to investigate the freezing of water and salt solutions (Carignano *et al.*, 2006; Vrbka and Jungwirth, 2005, 2007), as well as studying properties of the ice-water interface. In this thesis, a seeding method was developed for the study of ice growth near the water-solid interface, as detailed in section 3.6.

### 2.4.4 The surface and the interfacial region

Extensive research has been focused on understanding how a surface affects the first few layers of water. The surface characteristic known as *lattice mismatch* was introduced, which defines the degree of similarity between a surface's lattice structure and that of ice; a close match of lattices can provide a template for rapid ice growth. Turnbull and Vonnegut (1952) introduced the idea of zero lattice mismatch (within the context of CNT) to explain the excellent nucleating abilities of materials such as AgI crystals. However, others (Croteau *et al.*, 2008; Feibelman, 2008) have since questioned the role, if any, that lattice mismatch plays in ice nucleation. Cox *et al.* (2012) used the grand canonical Monte Carlo method to investigate the role of lattice mismatch by simulating a system with a model for hexagonal-lattice surfaces and the TIP4P water model. They noticed that, for atomically flat surfaces, a nominally zero lattice mismatch generated disordered contact layers containing smaller rings and observed hexagonal ice-like layers (which are associated with ice formation) only for surfaces with larger lattice constants. They concluded that the matching of the surface with the nearest neighbour oxygen-oxygen distance is a more suitable descriptor than its lattice characteristics.

Similar to Cox *et al.* (2012) on lattice mismatch, various studies provided evidence that one surface characteristic alone is insufficient to explain a material's ice-nucleating ability (Fitzner *et al.*, 2015; Glatz and Sarupria, 2018; Lupi and Molinero, 2014; Lupi *et al.*, 2014). Glatz and Sarupria (2018) studied a variety of different surface characteristics to determine how their interactions with other surface features and the interfacial water affect ice nucleation. Additionally, they used all-atom models in their simulations and were, therefore, able to find correlations between the water orientation and the ice nucleation tendency of the surface. They concluded that observing the interfacial water structure could indicate the ice-nucleating propensity of the surface independently of the surface involved, highlighting the importance of the interfacial region.

The interfacial region has been discussed in multiple prominent papers in recent years. Using the coarse-grained mW water model, Lupi *et al.* (2014) showed that rough amorphous surfaces did not enhance ice nucleation, whereas smooth graphite surfaces promoted ice nucleation. That was attributed to the fact that the graphite surface induced a layering in the density profile of water above the surface, while the rough amorphous surface did not. The same research team using the same methodology investigated further the impact of hydrophilicity on the ice nucleation tendency of graphite surfaces (Lupi and Molinero, 2014). The hydrophilicity of the surface was modified in two

different ways: firstly by modifying the water-surface interaction strength and secondly by introducing hydrophilic components at the surface. It was discovered that modifying the interaction potential led to enhanced ice nucleation and extended layering in water's density profile above the surface. Furthermore, an increase in the density of the hydrophilic components had an adverse effect to both layering and nucleation ability. The authors concluded that layering correlated well with ice nucleation efficiency.

Cox *et al.* (2015b) studied the effects of the layering mechanism by examining the nucleation rates, with the change of wettability on two surfaces with different morphologies. They deduced that layering of water over the surface could boost ice nucleation, in particular when the surface shows a rather stable potential to the water molecules. Fitzner *et al.* (2015) investigated the nucleation on generic crystalline, focusing on the rile of the wettability and surface morphology. They indicated three conditions where a crystalline surface can promote heterogeneous ice nucleation:

1. The formation of a water overlayer that acts as an in-plane template.
2. The emergence of a contact layer buckled in an ice-like manner.
3. Nucleation on compact surfaces with very high interaction strength.

Another challenging problem for MD simulations is that of the QLL characterisation. QLL structure has been increasingly investigated, mostly through experimental studies (Dash *et al.*, 2006; Furukawa, 2015; Limmer, 2016; Mochizuki and Molinero, 2018; Murata *et al.*, 2016). Given the QLL length scale and the limitations of experimental studies, MD simulations can be a useful tool to get molecular insight on the QLL properties.

Conde *et al.* (2008) performed NVT simulations and identified the liquid layer with the use of tetrahedral order parameter. More recently, various groups (Hudait *et al.*, 2017; Limmer and Chandler, 2014; Pickering *et al.*, 2018) determined the QLL thickness at the ice-vapour interface by MD simulations using enhanced sampling methods and the mW model. The molecules corresponding to the QLL were identified using the CHILL+ algorithm (Nguyen and Molinero, 2015), which allows the separation of all water molecules into liquid molecules, ice-like molecules, hexagonal ice molecules and cubic ice molecules.

In general, the results of the studies above show consistency between simulations and water models, reporting QLL thickness of at most 1 nm. These calculations are about one order of magnitude below most experiments (Chen *et al.*, 2017a). Although a large number of MD simulations have been performed with the various aspects of

heterogeneous ice nucleation, there are still open questions, especially with regards to the structure and dynamics of the interfacial region in the water-solid surface interface.

## 2.5 Summary

In the introductory section of this chapter, a short description of the advantages and the drawbacks, of conventional anti-icing systems, is given. The second section describes the nucleation mechanisms and the fundamentals of classical nucleation theory, which is the basis of all anti-icing strategies. In the third section, the directions and objectives of the experimental anti-icing approaches are illustrated and the need of a bridge with in-silico studies is revealed. Finally, the state of the art and the main challenges of molecular dynamics simulations of ice, are discussed. In the final section the literature review reveals that there is further clarification necessary of the structure and dynamics of the QLL at the ice-solid interface, which is understood to be a crucial part of the ice-nucleating ability of a surface. In the next chapter, the methodological basis underlying the molecular simulations performed in this thesis are discussed. Information regarding the important simulation measurements are also provided, and the novel approach to slab-seeded ice growth simulations used in this thesis is explained.

# Chapter 3

# Molecular dynamics methodology

*"In real life mistakes are likely to be irrevocable. Computer simulation, however, makes it economically practical to make mistakes on purpose. If you are astute, therefore, you can learn much more than they cost. Furthermore, if you are at all discreet, no one but you need ever know you made a mistake."*

- John H. Mcleod

This chapter describes the molecular dynamics (MD) computational methodology used in this thesis to investigate the three key questions that were highlighted in the Introduction chapter. It is divided in six sections. Section 3.1 describes how the trajectories of atoms are estimated using MD simulations, through solving Newton's equations of motion for a system of $N$ interacting particles. The equations are solved numerically and the forces and potential energies between interacting atoms are determined by interatomic potentials, which are introduced in section 3.2. In section 3.3, the frequently used water models for simulating ice nucleation in molecular dynamics are discussed, while section 3.4 focuses on the crystal structure of the surfaces used in this work. In section 3.5, the novel slab-seeded approach for MD simulations of surface icing is introduced. Finally, the main parameters that characterise the system's structure and dynamics, which can be used to link the microscopic details to macroscopic properties, are detailed in section 3.6.

## 3.1 Introduction to molecular dynamics

Molecular dynamics (MD) simulations calculate deterministically the Lagrangian trajectories (i.e. positions and velocities) in time for a system of interacting molecules and atoms. Due to their high-fidelity, MD simulations are normally required to be run on high-performance computers but can provide a connection between the microscopic world of molecules and the world of laboratory experiments, by averaging macroscale or bulk properties from the MD Lagrangian trajectories. The interaction potentials between atoms need to be setup correctly to ensure that the subsequent simulations are representative of reality. Once well-validated potentials are selected, the benefit of using MD simulations is that they can unravel new insights of a system's at the molecular scale, which are not easily accessible via experiments.

### 3.1.1 Equations of motion

In an MD simulation, the positions and momenta of the $N$ particles in a system are calculated. This is achieved by integrating the equations of motion for all particles. According to Newton's second law, when a force $\vec{f}_i$ is applied to a particle $i$ ($i = 1,2,\ldots,N$) positioned at $\vec{x}_i(t)$, it leads to an acceleration, $\vec{\alpha}_i$, given by:

$$\vec{f}_i(t) = m_i \cdot \vec{\alpha}_i(t), \text{ with } \vec{\alpha}_i(t) = \ddot{\vec{x}}_i(t), \tag{3.1}$$

where $m_i$ is the mass of the particle. Each particle interacts with $N-1$ other particles, and the force applied to each particle due to their interactions can be derived from the potential energy of the system:

$$\vec{f}_i(t) = -\frac{\partial U(\vec{x}_i(t))}{\partial \vec{x}_i}, \tag{3.2}$$

where $U$ is the potential energy. Newton's third law states that if a particle $i$ exerts a force on particle $j$, then particle $j$ will exert a force of the same magnitude on particle $i$ in the opposite direction:

$$\vec{f}_{ij} = -\vec{f}_{ji}. \tag{3.3}$$

The force $\vec{f}_{ij}$ is aligned to vector $\vec{x}_{ij}$, which connects the centers of particles $i$ and $j$, as shown in figure 3.1.

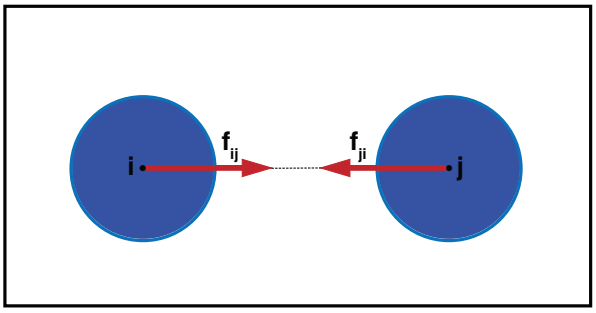


**Figure 3.1:** A representation of Newton's third law using two spheres $i$ and $j$, respectvely. Each sphere imparts an equal and opposite force ($\vec{f}_{ij}$ and $\vec{f}_{ji}$, respectively) on the other.

### 3.1.2 Time integration of equations of motion

Systems studied using MD contain a very large number of particles, with each particle simultaneously interacting with all others. Therefore, it is unfeasible to analytically evaluate the properties of such many-body systems. MD simulations bypass this problem by applying numerical methods. Using finite-difference techniques, the equations of motion are numerically integrated over time $t$ by dividing it into a sequence of time steps $\Delta t$. The forces $\vec{f}_i(t)$ acting on the particles at their current location $\vec{x}_i(t)$ are computed at each time step. During a time step $\Delta t$, $\vec{f}_i(t)$ is considered constant so it can be coupled with the known state of the system (position, kinetic energy, etc) at time $t$. This allows the prediction of the system's new dynamic state in the following time step $t+\Delta t$. Finite-difference methods usually employ the truncated Taylor expansion to provide expressions for positions $\vec{x}_i(t)$, velocities $\vec{v}_i(t) = \dot{\vec{x}}_i(t)$, the acceleration $\vec{\alpha}_i(t) = \ddot{\vec{x}}_i(t) = \vec{f}_i(t)/m_i$, etc. The resulting equations are:

$$\vec{x}_i(t+\Delta t) = \vec{x}_i(t) + \vec{v}_i(t)\Delta t + \frac{\vec{f}_i(t)}{2m_i}\Delta t^2 + \frac{\Delta t^3}{3!}\dddot{\vec{x}}_i(t) + \mathcal{O}(\Delta t^4), \tag{3.4}$$

$$\vec{v}_i(t+\Delta t) = \vec{v}_i(t) + \frac{\vec{f}_i(t)}{m_i} + \frac{1}{2}\dddot{\vec{x}}_i(t)\Delta t^2 + \mathcal{O}(\Delta t^3), \tag{3.5}$$

$$\vec{\alpha}_i(t+\Delta t) = \frac{\vec{f}_i(t)}{m_i} = \vec{\alpha}_i(t) + \dddot{\vec{x}}_i(t)\Delta t + \mathcal{O}(\Delta t^2), \tag{3.6}$$

$$\dddot{\vec{x}}_i(t+\Delta t) = \dddot{\vec{x}}_i(t) + \mathcal{O}(\Delta t). \tag{3.7}$$

$\mathcal{O}(\Delta t^N)$ defines the order of the truncation error and is determined by the first omitted term. These errors can be reduced but not completely eliminated.

The choice of algorithm used to integrate the equations of motion is important for an

accurate molecular simulation. The criteria that need to be considered when choosing an appropriate algorithm derived from equations (3.4) – (3.7) are:

1. *Computational cost*: In an MD simulation, the dominant cost arises from the evaluation of the forces, which usually scales with $N^2$. As these forces need to be computed every timestep, the secondary component of cost comes from having to integrate the equations of motion using a small timestep of the order of femtoseconds for a duration of time stipulated by the problem.
2. *Accuracy*: The algorithm's accuracy is determined by the truncation error, and the time step $\Delta t$ used. Algorithms that use large timesteps, in order to reduce the number of force evaluations within the simulation, require storing increasingly higher-order derivatives of the particle coordinates and consequently reducing the truncation error. Hence, algorithms that try to reduce computational cost, while retaining accuracy in the predictions of the trajectories, demand more memory storage.
3. *Stability*: While longer timesteps decrease the computational expense, they also affect the stability of simulation, due to accumulation of truncation errors.

A simple algorithm that broadly satisfies the aforementioned criteria, is the velocity Verlet algorithm (Swope *et al.*, 1982), which is described below.

### Velocity Verlet algorithm

The velocity Verlet algorithm (Swope *et al.*, 1982) computes positions and velocities at the same time. Let $\vec{x}_i(t)$, $\vec{v}_i(t)$ and $\vec{a}_i(t)$ be the current position, velocity and acceleration of a particle $i$, respectively. In order to define the coordinates of a particle at time $(t+\Delta t)$, the Verlet algorithm uses a Taylor expansion of the coordinates around time $t$:

$$\vec{x}_i(t+\Delta t) = \vec{x}_i(t) + \vec{v}_i(t)\Delta t + \frac{1}{2}\vec{a}_i(t)\Delta t^2 + \mathscr{O}(\Delta t^3). \tag{3.8}$$

The position $\vec{x}_i(t+\Delta t)$ has an error on the order of $\Delta t^3$, where $\Delta t$ represents the timestep used in the simulation. The velocities at the mid-step $t+\frac{1}{2}\Delta t$ can be estimated by using the current values of $\vec{v}_i(t)$ and $\vec{a}_i(t)$ according to the following Taylor expansion:

$$\vec{v}_i(t+\frac{1}{2}\Delta t) = \vec{v}_i(t) + \frac{1}{2}\vec{a}_i(t)\Delta t + \mathscr{O}(\Delta t^2). \tag{3.9}$$

For the updated positions $\vec{x}_i(t+\Delta t)$, the accelerations $\vec{a}_i(t+\Delta t)$ are estimated, and then jointly with the velocity at the mid-step $\vec{v}_i(t+\frac{1}{2}\Delta t)$, they are used to evaluate the

velocity $\vec{v}_i(t+\Delta t)$ according to the following Taylor expansion:

$$\vec{v}_i(t+\Delta t) = \vec{v}_i(t+\frac{1}{2}\Delta t) + \frac{1}{2}\vec{a}_i(t+\frac{1}{2}\Delta t)\Delta t + \mathscr{O}(\Delta t^2). \tag{3.10}$$

Therefore, the velocity Verlet algorithm enables the simultaneous evaluation of both positions and velocities at $t+\Delta t$. Following that, properties such as the kinetic and potential energy can be calculated at the same timestep, which is useful for calculating macroscopic properties, as discussed in the next section.

### 3.1.3 Thermodynamic ensembles

While MD simulations are unable, for computational reasons, to simulate systems larger than a few nanometres, some macroscopic properties can still be estimated from them. These properties are evaluated using information extracted from the microscale, with the caveat that multiple similar configurations in the microscale can provide the same macroscopic properties. An example is the evaluation of temperature of a macroscopic system. Temperature is a statistical quantity associated with the average of the kinetic energy of each single particle. The same average, and therefore the same temperature, can be obtained by different consecutive runs of the same MD simulation.

The idea of a thermodynamic ensemble is based on the fact that macroscopic characteristics are not affected by exact microscopic details. An ensemble can be defined as a collection of a significant number of microstates that together represent a state at which the system of interest can be. This means that the averages determine the macroscopic characteristics of the systems described by the ensemble. Thus, an ensemble is a crucial concept that allows us to relate the microscopic behaviour of many-body systems to their macroscopic observable behaviour. There are a few common ensembles used in MD and their choice depends on the constraints of the problem, as discussed below:

1. The canonical ensemble (NVT), is utilised when $N$ the number of particles, $V$ the volume of the system of interest and $T$ its temperature are kept constant. In the canonical ensemble every microstate is considered a closed system. This means that energy is allowed to transfer to and from the system, but the exchange of particles or mass is not.
2. The microcanonical ensemble (NVE), consists of microstates with the same number of $N$ particles, a fixed volume $V$, and have the same internal energy $E$. In the NVE ensemble the system is considered isolated, which means that there can be no interaction with the surrounding environment.

3. The grand canonical ensemble ($\mu$VT), corresponds to a collection of microstates that have a fixed volume $V$, temperature $T$ and chemical potential $\mu$. The $\mu$VT ensemble represents a system that allows the fluctuation of the amount of particles, and both mass and energy can be exchanged with the environment.

For an ensemble to enable evaluation of macroscale quantities, it needs to relate them with the microscopic functions of the positions and momenta. Let $O$ be a macroscale quantity of a system in a state of equilibrium, and $o(x)$ is the space function at the microscale, used to determine $O$. In accordance with the definition of an ensemble, it should be noted that the relationship between $O$ and $o(x)$ also depends on the number particles in the ensemble, $N$. For example, $O$ is calculated in an ensemble with $N$ particles using the formula:

$$O = \frac{1}{N}\sum_{k=1}^{N} o(x_k) \equiv \langle o \rangle. \tag{3.11}$$

For MD simulations, this equation is fundamental since it states that by conducting an average over the ensemble, every macroscopic observable $O$ can be measured from $o$. Thus, ensembles provide us with the ability to simulate systems that resemble real ones. Indeed, while we cannot solve the equations of motion for 1 mole of a substance as there are too many particles ($\sim 10^{23}$ particles), we can solve them for systems with hundreds to a few millions of particles, and run these simulations for long time periods to improve the statistics of computed quantities. Although the size of the simulating systems that are currently used cannot be considered macroscopic, their size is large enough to enable MD calculations to estimate the macroscopic properties. Therefore, MD simulations can be characterised as computer "experiments" that provide crucial insight regarding phase change phenomena, like ice growth, from the microscale regime.

### 3.1.4 Nosé Hoover thermostat

As mentioned previously, the comparison of MD results with their experimental counterparts frequently requires that the simulations be performed at constant temperature. This is achieved by the use of thermostats, which fix the temperature of the atoms. In the literature, there are various thermostats, with different effects on the system, and their use must fit the process studied. A deterministic approach to generate a canonical distribution (NVT) was developed by Nosé (1984). This was achieved by expressing the thermal heat bath in contact with the system with an extra degree of freedom $s$.

In this system, $m_T$ and $p_s$ represent the effective mass and momentum of variable $s$, respectively. With the introduction of this variable, the system's temperature was regulated by scaling the particles' momenta. The temperature of a molecular system is related to the average kinetic energy of the particles in the system. By scaling the particles' momenta we regulate the system's temperature. Also, the timestep $\Delta t$ is rescaled because of the scaling of the momentum. The scaled momentum $\vec{p}_i$, which is referred to as the real momentum, is defined by this relation $\vec{p}_i = \frac{\vec{p}_i^*}{s}$ , and $\vec{p}^*$ is characterised as the virtual momentum (Frenkel and Smit, 2001). The following relations associate the variables $\vec{x}_i$, $\vec{p}_i$, $\Delta t$ with the virtual variables, which are the result of the extended Lagrangian formulation associated with the thermal heat bath:

$$\vec{x}_i = \vec{x}_i^*, \tag{3.12}$$

$$\vec{p}_i = \frac{\vec{p}_i^*}{s}, \tag{3.13}$$

$$\Delta t = \frac{\Delta t^*}{s}, \tag{3.14}$$

$$\frac{dp_s^*}{dt^*} = \sum_{i=1}^{N} \frac{\vec{p}_i^{*2}}{m_i s^3} - \frac{N_f k_B T}{s}. \tag{3.15}$$

Since $s$ is a dynamic variable, the time step $\Delta t$ in real time fluctuates in accordance to equation (3.14). To overcome this inconvenience, Hoover (1985) introduced a friction parameter $J$, defined by:

$$J = \frac{1}{s} \cdot \frac{ds}{dt} = \frac{ds}{dt^*} = \frac{p_s^*}{Q_T}. \tag{3.16}$$

In the resultant Nosé-Hoover formulation, the effective mass $Q_T$ is responsible for the coupling between the heat bath and the system, making $Q_T$ an adjustable parameter for the simulation. Therefore, the slow exchange of energy between the heat bath and the system can be achieved by a high value of $Q_T$.

### 3.1.5 Periodic boundary conditions

MD systems contain an extremely small number of particles compared to experiments. In order to approximately resemble the behaviour of quasi-infinite bulk liquids and gases in MD simulations, Periodic Boundary Conditions (PBCs) are used. PBCs mimic the presence of bulk systems by surrounding the simulation box by an infinite number of identical copies, as shown in figure 3.2. The goal of PBCs is to minimise the simulation domain size and conserve the number of particles, and the linear momentum

and energy of incoming/outgoing particles in the simulation domain. When a particle leaves the domain during the simulation, it reappears near the face of the opposite boundary from where it left.

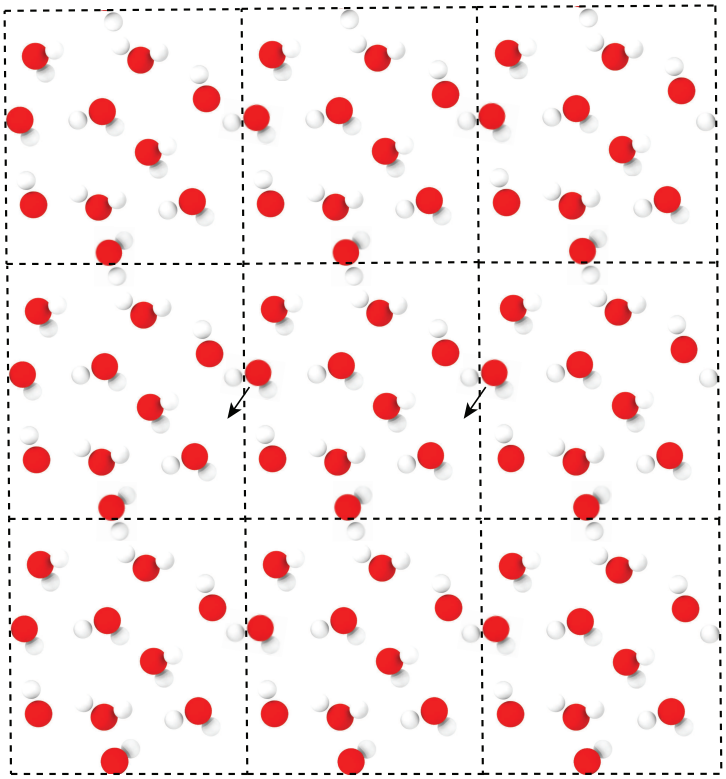

**Figure 3.2:** In periodic boundary conditions, the box in the middle is copied in all directions. The size of the box should roughly be 2-3 times the cut-off distance of the potential used, $r_{\mathrm{cut-off}}$. In this thesis $r_{\mathrm{cut-off}}$ = 12 Å.

The size of the periodic box will normally need to be big enough to avoid finite-size effects in the MD simulation. One molecule should, at least, not interact with its own image across the boundaries. Potential energy functions, such as the Lennard-Jones (LJ) potential, rapidly decrease to zero with distance between pairs of molecules (see section 3.2.1). The LJ potential is normally truncated to prevent interaction with all molecules in the system, localising the interaction with only neighbouring molecules within a cut-off distance $r_{\mathrm{cut-off}}$. This process is implemented through neighbour lists (see section 3.5). In the context of PBCs, it is common to set the size of the box to $2-3\times r_{\mathrm{cut-off}}$. The minimum image convention is used for PBCs to implement numerically a similar neighbour list algorithm to determine the potential energies due to images of molecules from across the PBCs.

### 3.1.6 Advantages and limitations of MD simulations

Statistical mechanics and the advent of modern computers has made it possible to develop fast molecular dynamics simulations codes and to apply almost directly to "real" problems. A molecular simulation is a powerful tool that enables us to study complex physical phenomena in many scientific and engineering disciplines. One example, which is the core of this thesis, is the behaviour of water. Experiments show that the behaviour of water at solid surfaces is intricate, with different freezing characteristics even at superficially similar surfaces. However, experiments cannot resolve the fast dynamics of molecules in ice growth processes. Computer simulations offer an advantageous way to study heterogeneous ice growth, as they allow us to understand how water molecules act at surfaces, often under conditions unattainable by surface science experiments. Like any numerical technique, molecular dynamics has its limitations and simplifying assumptions. The major approximations limiting the use of molecular simulations are: a) the accuracy of the adopted interaction model, and b) the computational cost inherent in the algorithm itself, such as the timestep used and how the equations of motion are integrated.

First, the accuracy of the interaction model can be improved using ab initio quantum mechanics calculations to generate potential energy functions. Ab initio simulations, however, are limited to systems with a few hundred atoms and are unable to estimate properties in a condensed phase. When we consider molecules consisting of multiple atoms, the forces applied on these atoms arise not only from intermolecular interactions but also from intramolecular bonding forces, i.e. within the molecule. In practice, however, MD simulations are mainly performed using simplified potential functions, or so called "force fields", that can approximate the influence of the aforementioned forces. Within the limitations in space and time that are intrinsic to molecular dynamics, the simulations try to reproduce "exact" results, which are normally thermomechanical properties validated or calibrated with experiments. In most cases, a failure by the simulation to reproduce an observable should be attributed to the deficiencies in the interaction model.

The second major approximation involves MD integration of the equations of motion. All MD integration algorithms (Allen and Tildesley, 2017) sample discrete points in time along a trajectory, meaning that the choice of algorithm used (e.g. velocity Verlet), and the size of time step $\Delta t$ adopted are both important. This results in a trade-off between accuracy and efficiency. For example, if $\Delta t \to 0$, equation (3.4) becomes exact and the trajectories are smooth, but this is computationally prohibitive,

while for large time steps it will diverge from the true trajectory resulting in a loss of accuracy. Furthermore, if $\Delta t$ is too large, the stability of the simulation is affected, leading to simulation "blow up". This happens when molecules with large timesteps are tracked too deep and too quickly into the repulsive part of the potential energy field of neighbouring molecules, leading to large unphysical forces, that propagate into the system.

## 3.2 Interparticle potentials

In MD simulations, the potential energy of the system $U(\vec{x}^N)$ is used to derive the individual forces $f_i$ exerted on the particles. The position of the atoms is given here in Cartesian coordinates, and the potential energy is a function of these positions. The potential function is the sum of two parts: one part is the bonded interactions, such as the bonds, angles and torsion in a molecule, and the second part is the non-bonded interactions, which are the intermolecular forces between molecules:

$$U(\vec{x}^N) = U(\vec{x}^N)_{\text{bonded}} + U(\vec{x}^N)_{\text{non-bonded}}. \tag{3.17}$$

In this thesis, the non-bonded interaction potentials are the van der Waals forces and electrostatic charges. In theory, non-bonded interactions have a non-local nature and also involve weak interactions between particles. Therefore the potential energy is the sum of 1-body, 2-body, 3-body ... n-body terms:

$$U(\vec{x}^N) = \sum_{i}^{N} u(\vec{x}_i) + \sum_{i,j}^{N} u(\vec{x}_i,\vec{x}_j) + \sum_{i,j,k}^{N} u(\vec{x}_i,\vec{x}_j,\vec{x}_k) + ... + \sum_{i,j,k,..,n}^{N} u(\vec{x}_i,\vec{x}_j,\vec{x}_k,...,\vec{x}_n). \tag{3.18}$$

In this thesis, the focus is on pairwise potentials $u(\vec{x}_i,\vec{x}_j) = u(\vec{x}_{ij})$, since these are the ones used in the simulations presented in the next chapter (see chapter 4), and neglect 3-body and higher order interactions (Allen and Tildesley, 2017). In this thesis, the pairwise non-bonded Lennard Jones and Coulomb potentials are used for water, solid and their interactions. The Stillinger-Weber potential, which is a 3-body potential, can also be used for water, ice and solid structures, but was not adopted in the current thesis for reasons described in section 3.3.2. The Lennard Jones and Coulombic pair potentials are described in the remainder of this section.

### 3.2.1 Lennard-Jones potential

The Lennard-Jones (LJ) potential has been studied extensively and it is considered as a prototype model for simple, realistic intermolecular interactions between non-bonded atoms or molecules (Jones, 1924a,b). The most common form of the LJ potential is:

$$U_{\mathrm{LJ}}(r) = 4\varepsilon\left[\left(\frac{\sigma}{r}\right)^{12} - \left(\frac{\sigma}{r}\right)^{6}\right], \tag{3.19}$$

where $r$ is the distance between two interacting particles and $\varepsilon, \sigma$ are the LJ parameters representing the depth of the potential well and the distance at which the potential energy is zero (often referred to as the diameter of the particle), respectively. The term $(\sigma/r)^{12}$ accounts for the short-ranged repulsion of the interacting particles due to Pauli's exclusion principle while $-(\sigma/r)^{6}$ describes their long distance attraction due to van der Waals forces. The graphical representation of equation (3.19) is provided in figure 3.3. The potential minimum appears at $r = 2^{1/6}\sigma$, where the force is zero. The maximum attractive force takes place at $r = (26/7)^{1/6}\sigma$.

When the interaction between two different type of atoms $i$ and $j$ is not known, the Lennard-Jones parameters are usually calculated using the Lorentz-Berthelot mixing rules (Lorentz, 1881):

$$\varepsilon_{ij} = \sqrt{\varepsilon_i \varepsilon_j}, \tag{3.20}$$

$$\sigma_{ij} = \frac{\sigma_i + \sigma_j}{2}. \tag{3.21}$$

The LJ potential have a long range interaction component $(\sigma/r)^{6}$, and so a particle should interact with all others in the simulating system. However, this would be extremely computationally expensive and limits the size of the simulation domain. Instead, it is common to truncate interactions beyond a finite cut-off radius $r_{\mathrm{cut-off}}$. This can be done by the use of modified versions of Lennard-Jones potentials, such as the Lennard-Jones truncated potential $U_{\mathrm{LJT}}$ (see figure 3.3b), which is defined as:

$$U_{\mathrm{LJT}}(r) = \begin{cases} U_{\mathrm{LJ}}(r), & r \leq r_{\mathrm{cut-off}} \\ 0, & r > r_{\mathrm{cut-off}} \end{cases} \tag{3.22}$$

The $U_{\mathrm{LJT}}$ potential is truncated at $r_{\mathrm{cut-off}}$ (Plimpton, 1995). The usual criteria for selecting $r_{\mathrm{cut-off}}$ in the literature is $r_{\mathrm{cut-off}} \geq 2.5\sigma$ (Toxvaerd and Dyre, 2011); in this thesis $r_{\mathrm{cut-off}} = 12$ Å, which meets this requirement. The use of truncated potentials re-

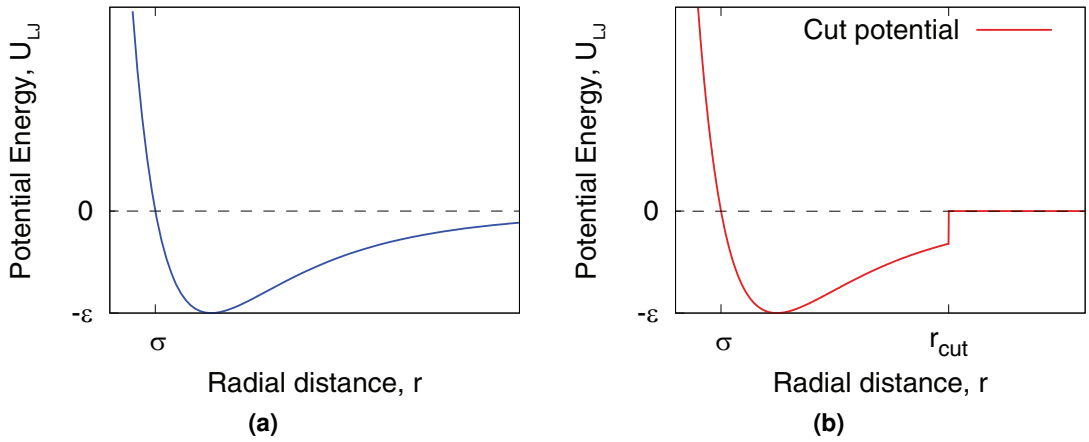


**Figure 3.3:** (a) The Lennard-Jones potential energy function from equation (3.18) and (b) the Lennard-Jones potential energy after applying a cut-off radius.

duces the computational cost of calculating $U_{\mathrm{LJ}}(r)$ by allowing the particles to interact only with their neighbours inside the $r_{\mathrm{cut-off}}$ distance, instead of the full domain $N$. In this work, this is implemented using the neighbour list algorithm. For each particle, a neighbour list is generated in the MD implementation which stores a list of all neighbouring particles within the cut-off radius. A thin skin $r_{\mathrm{cut-off}} + r_{\mathrm{skin}}$ introduces a buffer region outside $r_{\mathrm{cut-off}}$ that allows molecules to move freely between the skin and the internal cut-off region, thus delaying the computationally costly neighbour list rebuilds. The size of the skin is normally a fraction of $\sigma$, and is a compromise between infrequent neighbour list rebuilds and the increase in pair force calculations.

### 3.2.2 Coulomb potential

The electrostatic interactions are modelled in MD simulations through the Coulomb potential. The charges $q_1, q_2, q_3, \ldots, q_n$ on $N$ particles, which are located at positions $\vec{x}_1, \vec{x}_2, \vec{x}_3, \ldots, \vec{x}_n$, respectively, produce an electrostatic potential given as:

$$U_E = \sum_{i,j}^{N} \frac{q_i q_j}{4\pi\varepsilon_0 r_{ij}}, \tag{3.23}$$

where $\varepsilon_0$ is the permittivity of free space, and $r_{ij}$ is the distance between the atomic charges $q_i$ and $q_j$. In figure 3.4 the graphical representation of equation (3.23) is shown. Since the Coulomb interactions are long-range forces, their implementation in MD present similar difficulties as was the case for the LJ potential. The Particle-Particle-Particle-Mesh (PPPM) method (Hockney and Eastwood, 1988; Pollock and Glosli,

1996) is usually employed to enable the use of long-range forces in MD. The PPPM method maps the atom charges into a 3D mesh and divides the interparticle interactions into two parts. The first part ($F_{ij}^{\mathrm{sr}}$) is the short-range contribution of forces, and the second part is the forces that can be represented on a mesh ($F_{ij}^{\mathrm{m}}$), thus producing a total force $F_{ij}$:

$$F_{ij} = F_{ij}^{\mathrm{sr}} + F_{ij}^{\mathrm{m}}, \tag{3.24}$$

If the simulating systems are considered spatially infinite, this method provides a reasonable approximation. In MD simulations these long range interactions are only applied when periodic boundary conditions exist.

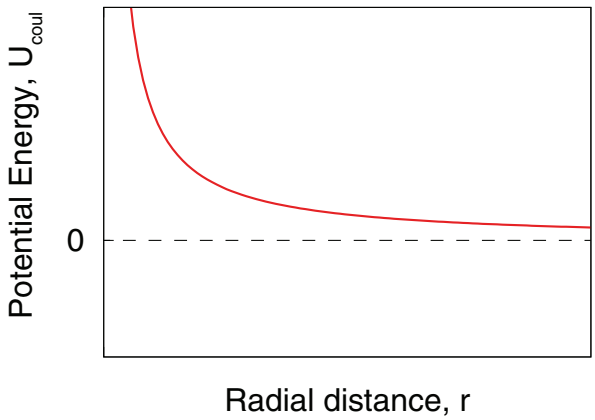


**Figure 3.4:** The Coulomb potential in equation (3.23) as a function of distance between two charged particles.

### 3.2.3 Stillinger-Weber potential

The Stillinger-Weber (SW) potential is the combination of two interactions. One is a two-body interaction, which accounts for the non-bonded interactions and the other is a three-body interaction that accounts for angle bending. The SW potential considers the bond energy not only based on the distance between the particles, but also from the bond angles subtended with two other particles. The standard form of the SW potential is as follows (Stillinger and Weber, 1985):

$$\begin{aligned} U_{\mathrm{SW}} = & \sum_i \sum_{j>i} A\varepsilon \left[ B\left(\frac{\sigma}{r_{ij}}\right)^p - \left(\frac{\sigma}{r_{ij}}\right)^q \right] \exp\left(\frac{\sigma}{r_{ij}-\alpha\sigma}\right) \\ & + \sum_i \sum_{j\neq i} \sum_{k>j} \lambda\varepsilon \left[\cos\theta_{ijk} - \cos\theta\right]^2 \exp\left(\frac{\gamma\sigma}{r_{ij}-\alpha\sigma}\right) \exp\left(\frac{\gamma\sigma}{r_{ik}-\alpha\sigma}\right), \end{aligned} \tag{3.25}$$

where the distance between particles $i$, $j$ and $i$, $k$ is $r_{ij}$ and $r_{ik}$, respectively; the angle formed by the triplet of particles $i$, $j$ and $k$ is $\theta_{ijk}$; $\varepsilon$ and $\sigma$ are the depth of the potential well for the pair-wise interaction and the distance where the potential is minimum, respectively.

Equation (3.25) includes the parameters $A, B, \alpha, p, q, \lambda, \theta$ and $\gamma$, which are fitting constants. Thus, accurate parametrisation is key to the usefulness of the SW potential, which is an iterative procedure that requires a gradual refinement of parameters (Raabe, 2017). Details of the parametrization have been described by several authors (MacKerell *et al.*, 1998; Mackerell, 2004; Xu *et al.*, 2007) and won't be discussed here. The original SW potential (Stillinger and Weber, 1985) takes the "ideal" tetrahedral angle ($\theta = 109.4712206...^\circ \approx 109.5^\circ$) as the reference value in its configuration, that makes it applicable to water, which forms a similar tetrahedral crystal (Bernal and Fowler, 1933). Exploiting this similarity, the SW potential is used in the development of the coarse-grained model of water (mW), which mimics the hydrogen-bonded structure of water through the introduction of a non-bonded angular dependent term that promote tetrahedral configurations (Molinero and Moore, 2009).

## 3.3 Water models

Several water models have been developed that try to reproduce specific macroscopic properties of water, depending on the application. Water models, which can vary by the number of atomic sites and potential interaction models used, are carefully calibrated in order to: i) reproduce the structural characteristics of water, such as the radial distribution of liquid water, the oxygen-oxygen distribution function and the internal energy of the liquid; and ii) accurately fit the most crucial macroscopic parameters of water, e.g the reduction of density during phase transition, and the melting point. The models must also exhibit robustness so that small changes in their parameters does not produce strong deviations in the model's predicted dynamics.

In general, existing water models can be classified into three categories:

1. *Rigid models*, where the atom positions are fixed and only non-bonded interactions are considered;
2. *Flexible models*, where the atom positions are tethered using spring constants, and their interparticle potentials include bond stretching and angle bending to accurately reproduce the crystal vibration spectra; and

3. *Polarizable models*, which include explicit polarizable terms and improve the capacity to reproduce water in different phases and interaction between phases.

Classical rigid water models are most widely used due to their computational efficiency. The most common water models are the SPC (Berendsen *et al.*, 1987), TIP3P (Jorgensen *et al.*, 1983), TIP4P/2005 (Abascal and Vega, 2005), TIP4P/Ice (Abascal *et al.*, 2005), TIP5P (Mahoney and Jorgensen, 2000) and the mW model (Molinero and Moore, 2009). These are simple rigid models and their computational cost in MD simulations increase with the number of interaction sites. The models most suitable to ice nucleation studies are the TIP4P/Ice model and mW model.

### 3.3.1 TIP4P/Ice water model

TIP4P/Ice model is based on the class of 4-sited TIP4P water models, and is particularly designed to reproduce the solid phase properties of water. TIP4P/Ice adopts the geometry and most characteristics of the TIP4P/2005 water model (Abascal *et al.*, 2005). There are four interaction sites contributing to the potential energy. Three of the sites are located at the oxygen and hydrogen atom positions, respectively. The fourth site, which is a massless site, denoted by the symbol M is coplanar with the oxygen O and hydrogen H atom positions and is placed at the bisector of the H-O-H angle (see figure 3.5). As with earlier TIP4P models (Dick and Madura, 2005), the O-H distance and H-O-H angle are fixed to the experimental values 0.9572 Å and 104.52°, respectively. The total potential energy of the system has two contributions, resulting from Lennard-Jones and electrostatic interactions. A key remark about the model is that the O site carries no charge, and thus contributes to the LJ force only, while the H and M sites are charged but have no LJ potential.

The interaction energy between two water molecules $i$ and $j$, $U_{ij}$, is given by:

$$U_{ij} = 4\varepsilon_{\mathrm{OO}}\left[\left(\frac{\sigma}{r_{\mathrm{OO}}}\right)^{12} - \left(\frac{\sigma}{r_{\mathrm{OO}}}\right)^{6}\right] + \frac{1}{4\pi\varepsilon_0}\sum_{a,b}\frac{q_a q_b}{r_{ab}}, \tag{3.26}$$

where $r_{\mathrm{OO}}$ is the distance between the oxygen sites of the two molecules, $\varepsilon_0$ is the permittivity of vacuum, and $a$ and $b$ stands for the charged sites of molecules $i$ and $j$, respectively. Other parameters in the TIP4P/Ice model, such as the site charges, and the geometrical distances are given in table 3.1.

While the TIP4P/Ice water model aims to represent the solid phase of water, it also gives an adequate representation of the liquid structure. However, the most important

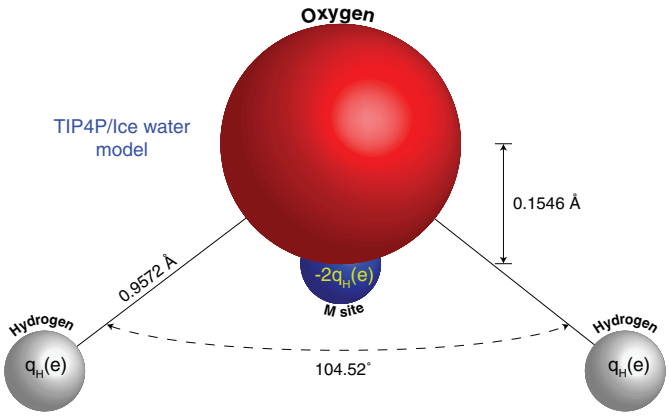


**Figure 3.5:** Schematic of the TIP4P/Ice water model (Abascal *et al.*, 2005), showing the two hydrogen atoms with charge $q_H = 0.5897\,(\mathrm{e})$, the oxygen atom which contains no charge, and a massless M site with a negative charge, equal to $q_M = -2q_H$.

| TIP4P/Ice water model parameters | Values |
|---|---|
| $\varepsilon$ | $0.21085\,(\mathrm{Kcal/mol})$ |
| $\sigma$ | $3.1668\,(\mathrm{\AA})$ |
| $q_H$ | $0.5897\,(\mathrm{e})$ |
| $q_M$ | $-2q_H(e)$ |
| $d_{OM}$ | $0.1577\,(\mathrm{\AA})$ |
| $\rho_l$ | $0.993\,(\mathrm{g/cm^3})$ |

**Table 3.1:** TIP4P/Ice water characteristics (Abascal *et al.*, 2005) as described in section 3.3.1.

advantage of the model is that it significantly improves the melting properties when compared to alternative TIP4P-based potentials (Abascal *et al.*, 2005).

### 3.3.2 Monoatomic water model (mW)

The mW model is a single-site coarse-grained water model governed by the Stillinger-Weber potential, which has a specific set of parameters and includes only short-range interactions (Molinero and Moore, 2009). As already mentioned in section 3.2.3, the first term of the SW potential is a pair-wise potential and the second term represents a three-body interaction and includes a parameter $\lambda$, which controls the hydrogen bond angles towards tetrahedrality. A higher value of $\lambda$ indicates a more tetrahedral model.

All other parameters of the Stillinger-Weber potential, calibrated for the mW model, are given in table 3.2.

| mW water model parameters | Values |
|---|---|
| $A$ | 7.049 556 27 |
| $B$ | 0.602 224 558 4 |
| $a$ | 1.8 |
| $p$ | 4 |
| $q$ | 0 |
| $\lambda$ | 23.15 |
| $\theta$ | 109.47° |
| $\gamma$ | 1.2 |

**Table 3.2:** These are the values used for parametrisation of equation 3.25 that produce the mW coarse-grained model (Molinero and Moore, 2009; Stillinger and Weber, 1985), which is described is sections 3.3.2 and 3.2.3.

Although mW does not take into account the long-range forces, it still outperforms many of the popular single-site water models in reproducing macroscopic properties of water (Molinero and Moore, 2009), and substantially increases the possible length and time- scale of an MD simulation (Sosso *et al.*, 2016a). This fact, in combination with its high speed in computing time, makes it particularly valuable for the investigation of slow processes in supercooled water, such as the mechanisms of ice growth. However, because of the lack of explicit hydrogen atoms and the absence of electrostatic forces, the mW model is unable to take into account charge effects occurring from the surfaces that affect the growth rates of these systems (Yan and Patey, 2011). As a result, the mW model produces ice growth rates that are four orders of magnitude higher than all-atom TIP4P models, which is inaccurate (Espinosa *et al.*, 2016a). Finally, unlike the TIP4P/Ice model, liquid formation at the solid/liquid interface is suppressed (Haji-Akbari and Debenedetti, 2017; Haji-Akbari *et al.*, 2014; Li *et al.*, 2013), so it cannot accurately investigate interfacial phenomena.

Various tests were performed to trial the use of the mW model, and the results were compared with the TIP4P/Ice model. The results obtained by the two water models in the investigation of interfacial phenomena strongly differed. In particular, the mW model underestimated the density differences between ice and liquid water (Haji-

Akbari and Debenedetti, 2017; Haji-Akbari *et al.*, 2014; Li *et al.*, 2013) as well as overestimated the self-diffusion coefficient (Haji-Akbari *et al.*, 2014). Therefore, while mW is particularly valuable for the investigation of ice nucleation, it is not suitable to study the structure and dynamics of ice growth at the ice-vapour and ice-solid interface, as carried out in this thesis.

## 3.4 Structures of FCC, BCC and HCP crystals

The process through which surfaces facilitate ice growth is not well understood. Although ice growing ability is different for different surfaces, the relation between the water behavior on a surface at supercooled temperatures and ice formation is still an open question. However, numerous studies (Cox *et al.*, 2012; Glatz and Sarupria, 2018; Pedevilla *et al.*, 2016, 2018) reveal the crucial role of the surface crystal structure in the promotion or inhibition of ice nucleation. In the majority of these studies, as well as in the framework of this thesis, the investigated crystal structures were of three types: Face-Centred Cubic (FCC), Body-Centred Cubic (BCC) and Hexagonal Closed-Packed (HCP) crystal structures. The characteristic parameters of these crystal types have a strong impact on their physical properties and are instrumental in the design of the MD simulations of heterogeneous ice nucleation. In this section, a short description of FCC, BCC, HCP and hexagonal ice ($I_h$) structures is given.

### 3.4.1 Face-Centered Cubic Structure

The FCC structure is composed of an atom at every cube corner and an atom in the center of every cube face. A representation of an FCC unit cell is shown in figure 3.6a. The relation between the cubic side length $a$ and the atomic radius $r$ is given by:

$$a = 2r\sqrt{2}. \tag{3.27}$$

The FCC comprises eight corner atoms ($N_c = 8$) and six face atoms ($N_f = 6$) while there are no interior atoms ($N_i = 0$). The number of atoms in a unit cell ($N_u$) for FCC crystal structure is four, and can be calculated by this equation:

$$N_u = N_i + \frac{N_f}{2} + \frac{N_c}{8}. \tag{3.28}$$

In FCC structures the number of nearest-neighbour atoms is 12, which is called the crystal coordination number. The coordination number in crystallography represents

the number of neighbouring unit cell atoms to a central atom. Another characteristic parameter of crystal structures is the atomic packing factor (APF), which indicates the total of the sphere volumes of all atoms contained in a unit cell divided per unit cell volume. The FCC structure has the most dense arrangement of atoms corresponding to an APF value approximately equal to 0.74.

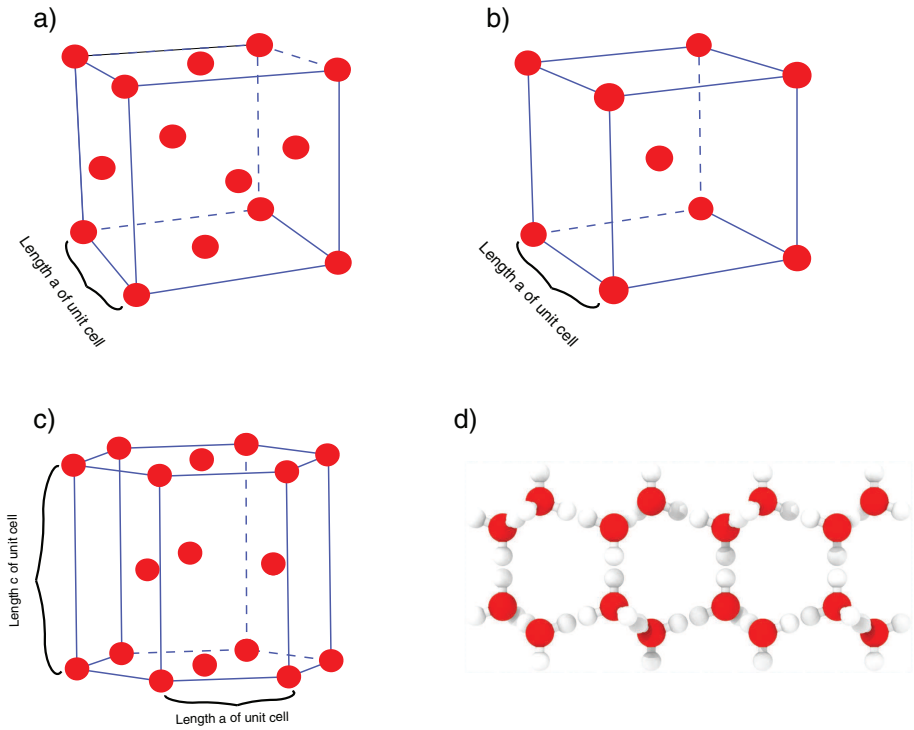


**Figure 3.6:** (a) FCC unit cell structure defined by unit cell $a$. (b) BCC unit cell structure defined by unit cell $a$ and $a/2$. (c) HCP unit cell structure defined by unit cell $a, c$. (d) Molecular structure of ice $\mathrm{I_h}$.

### 3.4.2 Body-Centered Cubic Structure

In this structure every cube corner is occupied by an atom, and one atom is situated at the centre of the cube, as can be seen in figure 3.6b. BCC structures have no face atoms ($N_f = 0$) and contain one internal atom ($N_i = 1$) at the cube's centre, and eight corner atoms ($N_c = 8$), each of which is shared between eight neighbouring cells. Thus, according to equation (3.27), the unit cell contains 2 atoms. For an atomic radius $r$, the length of the diagonal is $4r$. In addition, if $a$ is the cube's side length, then the length of the diagonal is $a\sqrt{3}$. It follows that:

$$a = \frac{4r}{\sqrt{3}}. \tag{3.29}$$

The coordination number of BCC is 8. Indeed, the nearest neighbours of every centre atom are its eight corner atoms. The APF of BCC is equal to 0.68, which shows that the FCC structure is more dense than BCC.

### 3.4.3 Hexagonal Close-Packed crystal structure

The HCP structure is presented in figure 3.6c. The top and bottom planes of the unit cell comprise six atoms arranged to produce regular hexagons and encompass a single central atom. They are separated by a midplane consisting of 3 atoms, which have as nearest-neighbours atoms in the bordering two planes, and consequently the coordination number of HCP is 12. As can be seen in figure 3.6c, 12 corner atoms are shared by 6 unit cells each ($N_c = 12$), 2 centre face atoms are shared by 2 cells ($N_f = 2$), and 3 atoms are internal at the unit cell. Thus, according to equation (3.30), the unit cell contains 6 atoms:

$$N_u = N_i + \frac{N_f}{2} + \frac{N_c}{6}. \tag{3.30}$$

As shown in figure 3.6c, the unit cell is a hexagonal prism, where the side length of its base is $a = 2r$ and its height $c$ is, by geometry, equal to $c = 4\sqrt{\frac{2}{3}}r$. Therefore, the volume of the unit cell is $24\sqrt{2}r^3$ and the APF is approximately equal to 0.74, similar to that of FCC.

### 3.4.4 Ice crystal structure of hexagonal ice

The crystal structure of ice is foundational to analysing its formation and its interaction with solid surfaces. Figure 3.6d shows a 3D molecular model of ice $I_h$, the form occurring most frequently and naturally on Earth. As can be seen, two hydrogen atoms closely adjoin every oxygen atom, so the triplet builds an intact $H_2O$ molecule. Strong covalent bonds firmly bind the two hydrogens while O-H bonds connect neighbouring water molecules. The two O-H bonds in a free $H_2O$ molecule form an angle of 104.5°, which approximates the tetrahedral angle of 109.5°. The distance between oxygen centers is 2.76 Å for the water molecules that are directly bonded, and the distance between the next-nearest neighbour is $\approx 4.51$ Å.

## 3.5 Ice Slab Seeding

This section provides an introduction to the slab-seeded approach where ice formation meets the surface, which underpins all simulations performed in this thesis.

The goal of this thesis is to study ice growth on FCC, BCC, and HCP surfaces, and investigate the role of surface wettability. However, this is challenging because ice nucleation is a rare event, and therefore there is no guarantee that ice formation would occur in any given simulation; in fact, many hundreds of simulations may be necessary, As mentioned previously, there are two ways to overcome the fact that nucleation is rare: use coarse-grained models (which reduce the interatomic interactions to be computed) or enhanced sampling (which accelerate the freezing process). It has been already established in section 3.3.2 that monoatomic water models do not simulate ice growth correctly (Espinosa *et al.*, 2016a). Enhanced sampling methods have their own set of issues, as described in section 2.4.3. In addition, both methods are typically limited to high supercooling, to minimise computational expense, which is impractical.

In this thesis, an alternative approach is used, namely 'seeded' MD, to overcome the limitations associated with coarse-grained or enhanced-sampling. Note that seeding approaches are used to bypass the challenges associated with ice nucleation. Seeding methods involve the inserting ice nuclei, or a 'seed', into the supercooled liquid water at the start of the simulation. If the seed is ensured to be larger than the critical nucleus at that temperature, it will grow and ice growth will proceed as would be the case following heterogeneous nucleation. This approach is computationally very efficient and, unlike the alternative approaches, can produce ice at mild supercooling comparable to experiments. Note that seeded MD does not provide insight or information into the mechanism of nucleation itself, as it assumes that the water molecules have already formed a critical nucleus at the start of the simulation. Instead of studying ice nucleation or ice adhesion which are separate topics, the focus of using seeded MD in this thesis is to study the mechanism of ice growth.

The background theory of seeded MD originated over 20 years ago. Nada and Furukawa (1996, 1997) performed ice-water interfacial simulations using the TIP4P water model, and their central conclusion was that the basal plane grows by a layer-by-layer process, while the primary prismatic plane grows through a collective molecular process. However, they did not provide a complete description of the crystallisation mechanism, since equilibrium was not reached due to computational cost. The first systematic simulation of ice growth in the presence of water and vacuum was presented

by Carignano *et al.* (2005). They adopted an initial configuration consisting of an ice layer in contact with a water layer. They observed the evaluation of the system until it arrives at an equilibrium state, consisting of an ice slab at the center of the system, and almost identical quasi-liquid layers at both free surfaces. A similar approach was also used recently to investigate the effect of freezing on a nanoparticle deposited on the surface (Uchida *et al.*, 2020).

### Slab-seeding growth

The simulation setup used in this thesis relies on ideas introduced by Carignano *et al.* (2005) and others (Uchida *et al.*, 2020). The system developed by Carignano *et al.* (2005) used here consists of a region of liquid water, an ice slab and vacuum on both sides of the simulation box. The choice of the ice slab dimensions is not trivial. If the slab contains too few molecules, there is a risk that it can melt when placed in contact with water. On the other hand, if it has too many molecules, the simulations would become more computationally expensive than necessary. In this thesis, the slab dimensions were determined to satisfy certain constraints as described below.

First, it is known that the number of molecules contained in a *spherical* ice nucleus must be higher than the critical cluster size of $N_c$ molecules, which can be estimated from CNT using the equation (Espinosa *et al.*, 2014; Sanz *et al.*, 2013; Zaragoza *et al.*, 2015):

$$N_c = \frac{32\pi\gamma^3}{3\rho_i^2|\Delta\mu|^3}, \tag{3.31}$$

where $\rho_i$ is the number density of ice, $\Delta\mu$ the chemical potential and $\gamma$ the interfacial energy. Note that here $\Delta\mu$ depends on the degree of supercooling $\Delta T_s$ discussed previously. While $N_c$ is tricky to compute analytically (due to challenges with obtaining $\Delta\mu$), a dataset relating $\Delta T_s$ and $N_c$ has been previously tabulated by Pereyra *et al.* (2011). For the value of supercooling used in this thesis ($\Delta T_s = 32$ K), $N_c$ was estimated to be 600 molecules. While this estimate is for a spherical cluster and not the slab used in thesis, it does provide a reasonable lower bound on the number of molecules needed to ensure ice growth in the simulations of this thesis.

Second, the thickness of the ice slab must be sufficient to prevent melting because of the interactions at the ice-water interface. Previous work has indicated that the critical interfacial region has a thickness of approximately 10 Å (Karim and Haymet, 1988; Nada and Furukawa, 1996). This means that the ice slab must be thicker than 10 Å, thus providing a lower bound on its vertical dimension (it is periodic in the other

two dimensions). Using these estimates and following a series of tests, the ice slab thickness was set to 14.7 Å, containing 640 water molecules. This slab was shown to freeze the adjacent liquid water molecules in all our simulations.

Figure 3.7 shows a schematic representation a freezing simulation setup using this ice slab, and an illustration of the freezing process (which is termed 'slab-seeding'). Note that as there is no surface involved, this setup only applies to homogeneous ice growth, and cannot provide any insight into the role of surface characteristics in inhibiting/enhancing ice growth. It can be noticed in figure 3.7a that there is a gap between the ice slab and liquid water. This is to avoid any overlapping between the water molecules at the start of the simulation. The system is first equilibrated using an NVT thermostat at 240 K. Once the system is equilibrated, the thermostat applied to the supercooled water is turned off allowing phase transition to begin. Figure 3.7b shows the state of the system at $t = 0$ when the thermostat was turned off, and figure 3.7c illustrates the steady-state structure of the system after $t = 65$ ns.

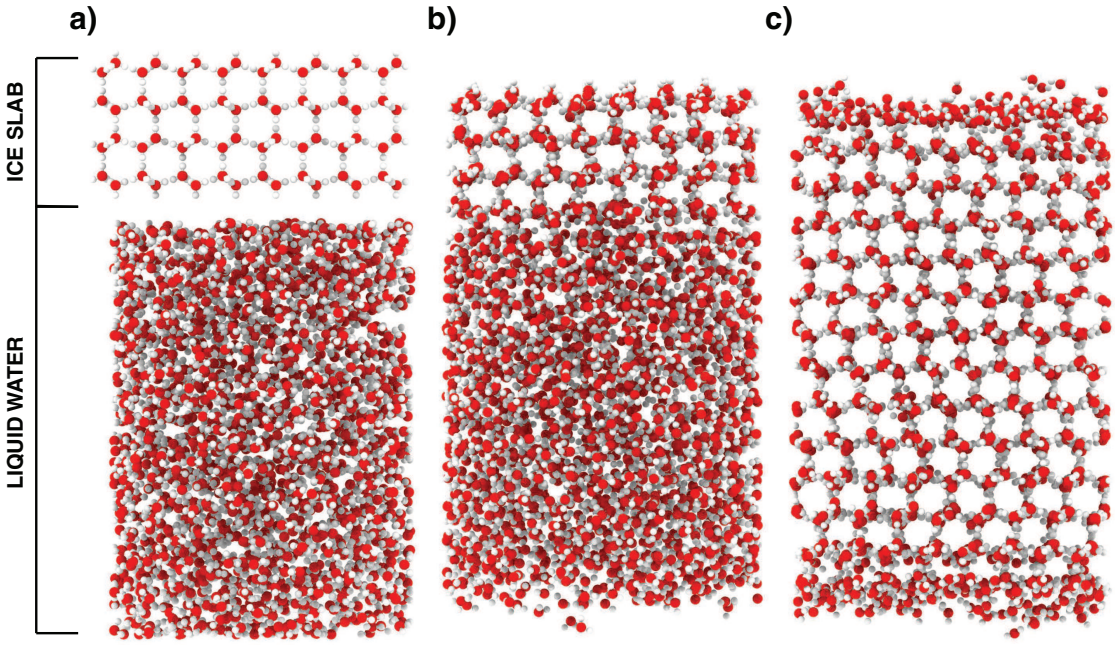


**Figure 3.7:** (a) Initial system setup before equilibration starts, showing two slabs of disconnected liquid and ice. (b) Water-ice configuration after equilibration, with time reset at $t = 0$. (c) The system after reaching a steady state at $t = 65$ ns

The present thesis uses a setup identical to the one shown in figure 3.7 with an important modification — namely the surface. The addition of the surface such that the supercooled liquid is sandwiched between the ice slab and the surface allows the study of growth at the surface. This is called 'heterogeneous slab-seeding' or 'slab-seeding'

for short (as there are no homogeneous ice growth simulations presented in this thesis). The results of the slab-seeding ice growth simulations are presented in chapter 4.

## 3.6 Key Simulation Measurements

There are a number of parameters that can be used as indicators of ice promotion or inhibition, namely: i) the wettability of the surface, evaluated by measuring the contact angle of a water droplet on the surface; ii) the diffusivity of water molecules, estimated using the self-diffusion coefficient $D$; iii) the thickness, $T_{\mathrm{QLL}}$, of the quasi-liquid layer at the water-surface interface; and iv) the layering $L$ of the interfacial water. The measurement process for each of these is outlined in this section.

### 3.6.1 Measurement of contact angle

Wettability captures the balance between adhesive and cohesive forces when a liquid is in contact with a solid surface. It is quantified by the solid-water contact angle (see figure 3.8 and figure 2.3). A popular method to estimate contact angles in experiments is the sessile droplet approach where a water droplet is positioned on a solid surface. The droplet geometry acquired by a camera and the contact angle is then determined from the droplet's geometry.

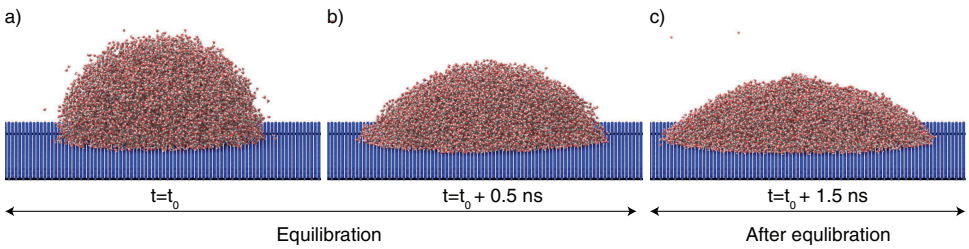


**Figure 3.8:** (a) Initial state of a semi-spherical droplet on top of an FCC hydrophilic structure, (b) new positions all water molecules during equilibration, and (c) final position of the droplet after equilibration.

The calculation of the contact angle in MD simulations is usually designed to mimic the experimental procedure (Jiménez-Ángeles and Firoozabadi, 2016; Santiso *et al.*, 2013; Wei *et al.*, 2014). 2D axisymmetric slices of the droplet are taken, in which density is measured. This density is evaluated from the coordinates of all oxygen atoms, assuming axisymmetry around a centroidal axis normal to the solid surface. The whole

domain was divided in cells, each of size 1 Å and the local number density of every subcell was calculated. The interface of the droplet varies from bulk to vapour very rapidly as can be seen in figure 3.9. The isocontour lines are fitted to the density field and the isocontour with 50% the bulk liquid density is chosen. From this isocontour, a circle is fitted and the tangent near the wall surface is measured. Multiple values of contact angles for different-sized MD droplets are obtained and averaged, which is described in section 4.2.

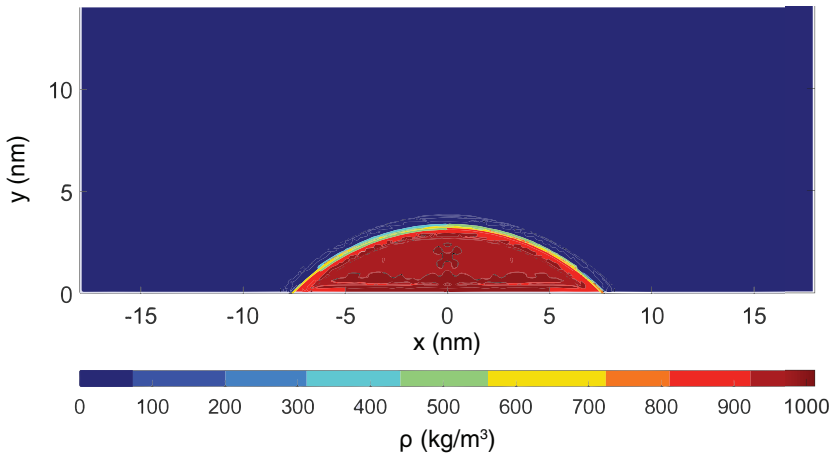


**Figure 3.9:** The simulations box is divided into 2D cells of 1 Å size and the local density of these cells is measured. The contact angle, $\theta$ is found as being the angle of the tangent with the horizontal axis from the circular fit through the 50% isocontour of density. This figure represents the case of an FCC structure with solid/solid interaction energy of $\varepsilon_{ss} = 0.91$ kcal/mol.

### 3.6.2 Measurement of water self-diffusion coefficient

The water self-diffusion coefficient ($D$) can be used as an indicator of the ordering of the water molecules. Calculation of $D$ depends on the molecule ensemble size and on the molecular simulation time. A standard approach used in MD simulations of water is based on the Einstein equation, that relates the mean square displacement (MSD) of a particle to the time interval in which this displacement occurs, using the equation:

$$D = \frac{1}{2n} \frac{\langle \mid \vec{x}(t) - \vec{x}_0 \mid^2 \rangle}{t}, \tag{3.32}$$

where $n = 3$ is the diffusion space dimensionality, and:

$$\langle \mid \vec{x}(t) - \vec{x}_0 \mid^2 \rangle = \frac{1}{N} \sum_{i=1}^{N} \mid \vec{x}^{\,i}(t) - \vec{x}_0^{\,i} \mid^2, \tag{3.33}$$

where $N$ is the number of particles of the ensemble, and $\vec{x}_0^{\,i}$ is the initial position of the $i$th particle.

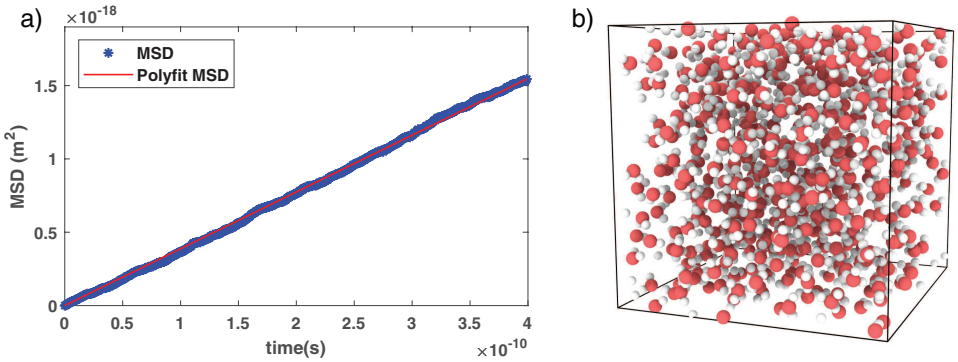


**Figure 3.10:** (a) The MSD calculation of 550 water molecules. The self-diffusion coefficient was obtained by calculating the slope of the linear graph and then dividing its value by 2. (b) The simulation box containing the 550 water molecules at $T = 300$ K.

For a steady-state system in equilibrium, MSD varies linearly with $t$, and $D$ can then be obtained from the slope of this plot. In Figure 3.10, the MSD of an equilibrium system of 550 TIP4P/Ice water molecules at a temperature of $T = 300$ K is presented. The value of the self-diffusion coefficient obtained using equation (3.32) is $D = 1.94 \times 10^{-9}$ $\mathrm{m}^2/\mathrm{s}$ which is close to the experimental value of $D_{exp} = 2.3 \times 10^{-9}$ $\mathrm{m}^2/\mathrm{s}$ (Price *et al.*, 1999). The approach based on Einstein's equation is the best choice for long simulations, whereas for small molecular ensembles and very short times, the fluctuations intrinsic in the calculation of Einstein's equation can influence the reliability of the results. In the framework of this thesis the Einstein method is applied to relatively long simulation timescales with a sample size larger than 100 molecules, which is considered sufficient for calculating the water self-diffusion coefficient (Li *et al.*, 2008; Meier *et al.*, 2001).

### 3.6.3 Identification of ice molecules

Classification of water molecules belonging to the solid or liquid phase during the process of ice growth is a crucial step in analysing the simulation results. This classification is achieved using the CHILL+ algorithm, developed by Nguyen and Molinero (2015). CHILL+ relies on the correlation of bond-order parameters to identify and count the number of staggered and eclipsed O-O bonds in the HBN, which distinguish hexagonal/cubic ice and non-ice molecules (Steinhardt *et al.*, 1983; Ten Wolde *et al.*, 1996). The local order near every water molecule $i$ is defined by the local orientational

bond order parameter vector $q_l(i)$ with $2l+1$ complex components close to the four nearest neighbours (Nguyen and Molinero, 2015):

$$q_{lm}(i) = \frac{1}{4}\sum_{j=1}^{4} Y_{lm}(r_{ij}). \tag{3.34}$$

In this equation, $q_{lm}(i)$ expresses the orientational arrangement of the four neighbours closest of a molecule derived from spherical harmonics $Y_{lm}(\hat{r}_{ij})$, and $\hat{r}_{ij}$ is the unit vector that connects $i$ with its neighbors $j$ (Nguyen and Molinero, 2015). CHILL+ is very efficient at identifying liquid water molecules, hexagonal ice, cubic ice, interfacial ice and clathrate hydrate, as shown in literature (Hudait *et al.*, 2017; Lupi *et al.*, 2016; Mochizuki and Molinero, 2018; Qiu and Molinero, 2018).

### 3.6.4 Measurement of Quasi-Liquid Layer thickness

Numerous experiments indicate the presence of a quasi-liquid layer (QLL) at the surface of ice, as discussed in section 2.3.1. However, the experimental quantification of its structure and dynamics is quite difficult (Dash *et al.*, 2006; Zeng and Li, 2019). Molecular dynamics simulations present a useful alternative as they are able to access the relevant length scales and provide information about the structure of these regions at the nanoscale. MD simulations could analyze the behaviour of ice at the interface with vacuum, and report QLL thickness below what experiments provide (Limmer and Chandler, 2014).

The quantification of whether a region is solid, liquid or QLL can be determined by estimating the self-diffusion coefficient ($D$), as $D$ varies significantly between liquid and QLL layers. QLL can also be studied from a structural perspective, which requires the distinction between liquid-like and ice-like molecules using algorithms such as CHILL+ (Moore *et al.*, 2010; Nguyen and Molinero, 2015). Once the total number of liquid molecules at an interface are found, the thickness $T_{\mathrm{QLL}}$ (units Å) is estimated using the following equation (Conde *et al.*, 2008):

$$T_{\mathrm{QLL}} = \frac{N_{\mathrm{liquid}} M}{\rho N_{AV} L_x L_y 10^{-24}}, \tag{3.35}$$

where $N_{\mathrm{liquid}}$ is the average number of liquid-like molecules throughout the simulation run, $M$ is the mass of one water molecule, $N_{AV}$ is Avogadro's number, $\rho$ is the density of liquid water and $L_xL_y$ is the area of the interface in $\mathrm{Å}^2$. A typical representation of $T_{\mathrm{QLL}}$ can be seen in figure 3.11, where an ice slab containing 3200 molecules was

simulated at temperature $T = 240$ K for 10 ns using the TIP4P/Ice water model. This simulation gives $T_{\mathrm{QLL}} = 5.92$ Å, which is very close to the value reported by Conde *et al.* (2008) for this given temperature, $T_{\mathrm{QLL}} = 5.93$ Å, thus validating the ice setup and measurement technique.

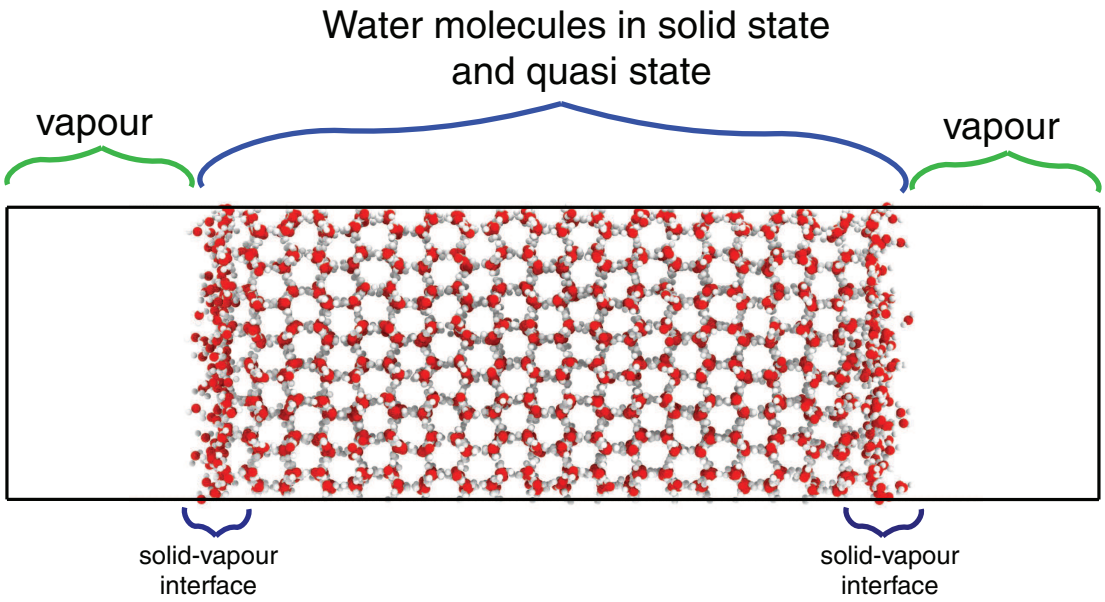


**Figure 3.11:** All of the liquid-like water molecules are gathered close to the ice-vapour interface region, with some exceptions of defects inside the ice slab. So by calculating the number of liquid-like water molecules we are able to estimate the QLL thickness at the ice-vapour interface.

### 3.6.5 Measurement of interfacial water layering

The density layering of interfacial water plays a significant role in analysing ice formation on surfaces. The parameter quantifying density layering is defined by Lupi *et al.* (2014) as:

$$L = \int_0^{z_{bulk}} \left| \frac{\rho(z)}{\rho_{bulk}} - 1 \right|^2 dz, \tag{3.36}$$

where $\rho(z)$ is the local density of water at a distance $z$ above the surface, $\rho_{bulk}$ is the density of bulk liquid water and $z_{bulk}$ is the distance at which $\rho(z)$ approximates $\rho_{bulk}$. Cox *et al.* (2015a) showed that $L$ increases monotonically with adsorption energy ($E_{ads}$), while the dependence of nucleation rate on $E_{ads}$ is not monotonic. Nevertheless, they observed that for high values of $E_{ads}$, the first layer of interfacial water is inactive to ice nucleation. Because of this, they proposed an alternative parameter, $L^*$, to

compute layering of interfacial water, excluding the contribution of the first layer:

$$L^* = \int_{z_0}^{z_{bulk}} \left| \frac{\rho(z)}{\rho_{bulk}} - 1 \right|^2 dz, \tag{3.37}$$

where $z_0$ varies in dependence of the surface. In doing so, they found a better correlation of $L^*$ on nucleation rate including surfaces with high adsorption energy. Both these measures are found to be useful in the analysis in this thesis, as detailed in the next chapter.

## 3.7 Summary

This chapter starts with an introduction to the computational method used in this thesis (MD). Then, the interparticle potentials, water models and surfaces used in simulations in this thesis are discussed. Finally, the parameters and procedures characterising the water freezing over a surface are described. The aim of this chapter is to setup the tools and measurements needed to answer the open questions identified in chapter 1. The simulation results will be discussed in the next chapter.

# Chapter 4

# The influence of surface wettability and structure on ice growth

*"The ability to perceive or think differently is more important than the knowledge gained."*

- David Bohm

Heterogeneous icing has been studied over a large variety of surfaces, with the goal of developing effective anti-icing strategies. As stated in chapter 2, these studies have commonly focused on determining: a) the role of surface characteristics on the reduction of ice nucleation (Eberle *et al.*, 2014); b) the delay of freezing time (Kim *et al.*, 2012; Wilson *et al.*, 2013), the lowering of freezing point (Mishchenko *et al.*, 2010); or c) the reduction of ice adhesion (Ling *et al.*, 2016). Depending on the specific application, the surface can be optimised on one or two of these objectives, but design trade-offs inevitably mean that it is very difficult to achieve all three simultaneously. It is clear that designing an optimal anti-icing surface is complex both because there are several ways to achieve anti-icing based on the application at hand, and because the mechanisms of icing are not well understood. Molecular simulations provide an alternative to experiments in understanding icing mechanisms, but heterogeneous ice nucleation and growth is challenging to simulate.

The present thesis overcomes the limitations of heterogeneous nucleation by devising an alternative approach, which is termed as "slab-seeded" ice growth and was introduced in chapter 3. In this setup, supercooled water is placed between a slab of ice and the surface, and the ice front grows in time until the water is frozen completely. This allows the monitoring of the phase transition of the enclosed liquid-water molecules into ordered ice structures with an unbiased brute-force approach, without the need of enhanced sampling. As the nucleation of water starts in the interface between ice

and liquid water, the presence of the slab means that a critical nucleus for ice growth is present from the beginning of the simulation (Nada and Furukawa, 2005; Schutzius *et al.*, 2015; Vrbka and Jungwirth, 2005). Note that this seeded approach can be used to simulate ice growth because once the ice is nucleated, it is the surface-water interaction that determines the ice formation at the liquid-solid interface. Therefore, the present method can be used to investigate the influence of wettability and surface crystal morphology on the formation and structure of interfacial ice. Following this approach, it is possible to investigate a number of parameters characterising ice formation on top of any surface for which accurate intermolecular potentials exist.

In this chapter, the effect of the surface wettability and lattice structure on the crystallisation of water molecules, interfacial ordering, and QLL formation is studied. The slab-seeded method introduced here and can in the future be applied to studying other factors relevant to heterogeneous ice nucleation as well.

## 4.1 Simulation Setup

The main MD setup in this thesis is shown in figure 4.1 with three distinguishable layers. From top to bottom the case consists of: a seeding ice slab, a region of supercooled liquid water, and a surface-of-interest. The size of the simulation box in the $x \times y \times z$ directions is $45.215 \times 31.326 \times 90$ Å$^3$ and periodic boundary conditions are applied in all three directions. An empty space of height 24 Å above the ice slab is introduced in the computational domain in order to avoid the interaction of the ice slab with the surface through the top periodic boundary. This top region will be referred to as the vapour region of the system in the following analysis. The ice slab consists of 80 hexagonal ice cell units each composed of 8 water molecules totalling 640 molecules (1920 atoms). The approximate thickness of the ice slab is 14.7 Å. The liquid region initially comprises 1632 molecules (4896 atoms) with height 40 Å. This setup was designed to contain a minimum amount of atoms, while operating beyond the scale of finite size effects. As a result, the MD simulations are computationally efficient enough to run within 300 ns on 24 processor cores on ARCHER (the UK's national supercomputing service), in which ice growth is observed reaching the surface in all the simulations.

Hexagonal ice is an anisotropic crystal, consisting of stacked hexagonal rings in the basal planes, and the primary and secondary prismatic faces perpendicular to it. Ice

growth in the basal plane occurs layer-by-layer (Nada and Furukawa, 1996, 1997), which is not the case for the prismatic plane where less organised ice growth is observed. Consequently, the growth kinetics depends on which plane the ice-liquid interface grows from. Here, the ice growth is considered from the basal planes due to the aforementioned reason. Furthermore, ice formation is expected to be slower from basal plane than from the prismatic plane (Carignano *et al.*, 2005).

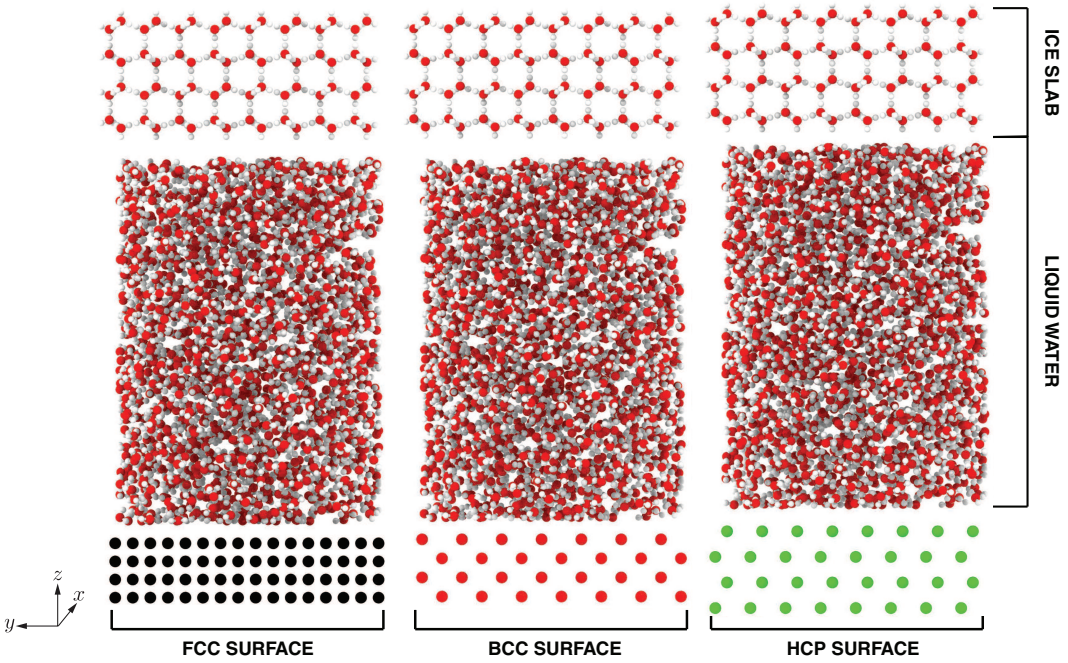


**Figure 4.1:** Schematic of the MD simulation setup for ice growth on three different surfaces.

In this work, three different types of surfaces (see section 3.4) with different crystal morphologies and lattice mismatch indexes ($\delta$) are used, i.e FCC (based on aluminium), BCC (based on sodium), and HCP (based on yttrium), respectively, where $\delta$ is defined as:

$$\delta = \frac{a_s - a_i}{a_i}, \tag{4.1}$$

where $a_s$ and $a_i$ are the lattice parameters of the surface unit cells and the basal face of ice, respectively (Cox *et al.*, 2012). $\delta$ quantifies the difference between the crystal structure of the surface when compared to the structure of ice. A low lattice mismatch is associated with a higher propensity for heterogeneous nucleation. The values of $\delta$ for the three surfaces used in this work are 9% (FCC), 1% (BCC) and 9% (HCP), respectively.

The lateral dimensions of the surfaces are equal to that of the ice slab and their thick-

nesses are determined by their unit cells, with two stacked layers used for all lattices. As the ice slab dimensions are fixed ($45.215 \times 31.326 \times 14.7$ Å$^3$), the lattice spacing was adjusted to match the lateral dimensions of the ice slab exactly. Specifically the lattice spacing in the X-axis was adjusted by 1.59% in the FCC surface, 4.1% in the BCC surface and 3.3% in the HCP surface. Similarily, the Y-axis it was adjusted by 3.21% in the FCC, 4.3% in the BCC and 4.5% in the HCP surface. The details of these adjustments are provided in table 4.1. This results in surfaces comprising of 704 (FCC), 308 (BCC), and 352 (HCP) atoms, respectively. Note that the planes of the surfaces exposed to the liquid are the FCC(001), BCC(001), and HCP(0001), respectively. The effect of varying the crystal plane facet was not explored in this thesis, and all results presented are for the facets listed above.

The wettability of the surface was varied by selecting four values of $\varepsilon_{ss}$ (solid-solid), while keeping a fixed $\sigma_{ss} = 2.573$ Å. This resulted in a total of twelve different surfaces with surface properties listed in table 4.2. The $\varepsilon_{ss}$ values were chosen in order for the surfaces to be characterised as supherhydrophilic, hydrophilic, hydrophobic and superhydrophobic, respectively. It was also important to ensure that the same $\varepsilon_{ss}$ values were fixed for all three surfaces to enable easier comparison between them. Hence, while calibration was initially performed for FCC surfaces and then used for all surfaces, the resulting values of $\varepsilon_{ss}$ do not correspond exactly to the wettability specified for BCC and HCP surfaces. The Lennard-Jones parameters for solid-water (*so*) interactions are also shown in the table. As ice growth is a stochastic process, four independent realisations are run for each surface, resulting in a total of 48 simulations. All results presented in this work are obtained by averaging across the realisations.

| type of surface | $a_x$ (Å) | $a_x$ modified (Å) | $a_y$ (Å) | $a_y$ modified (Å) |
|---|---|---|---|---|
| FCC | 4.04 | 4.11 | 4.04 | 3.91 |
| BCC | 4.29 | 4.11 | 4.29 | 4.47 |
| HCP | 3.64 | 3.76 | 3.64 | 3.48 |

**Table 4.1:** Table showing the adjustments made to each of the surface to match the overall X-Y dimensions of the ice slab.

The ice growth mechanism has been simulated by means of brute-force molecular dynamics (MD) simulation, using the open-source LAMMPS simulation package (Plimpton, 1995). Simulations were run on ARCHER, the UK's national supercomputer service using 24 processors per simulation. Note that, due to the long-range nature of the potentials used, the system of equations solved in molecular dynamics simulations is

stiff and can produce complications if not properly treated. For example, in the absence of any constraints, the internal vibrational oscillations of the water molecules would exceed the Nyquist limit for the timesteps used in our simulations, at which point the simulations would become unstable. Decreasing the timestep is not feasible as this would make the simulations computationally intractable. This problem is resolved in this thesis by removing the internal degrees of freedom in the water molecules and instead treating them as rigid molecules.

All MD simulations presented in the thesis use the rigid TIP4P/Ice model introduced in section 3.3.1, and the SHAKE algorithm (Ryckaert *et al.*, 1977) was used to constrain the geometry of the water molecules, and allow for the use of timesteps on the order of femtoseconds. Moreover, a spring force is applied independently to each atom of the surface to tether it to its initial position (i.e., position at the first timestep). The applied spring force correctly takes into account any crossings of periodic boundary by the atom since it was in its initial position. The magnitude of the force on each atom, at each timestep, is given by this equation:

$$F = -K \cdot r, \tag{4.2}$$

where $K$ is the spring constant and $r$ is the displacement of the atom from its current position to its initial position (Ryckaert *et al.*, 1977). In this thesis, $K$ was set to be 10 $\mathrm{eV}/\mathrm{\AA}^2$.

The equations of motion were integrated using the velocity Verlet algorithm with a time step of 2 fs. The cut-off distances for all Lennard-Jones (LJ) and Coulombic interactions are $r_{\mathrm{cut-off}}$ = 12 Å and 10 Å, respectively, and the skin distance for the neighbour lists is 2 Å. Long-range Coulombic interactions are computed using the Particle-Particle-Particle-Mesh (PPPM) method.

System equilibration was performed using the NVT canonical ensemble thermostatted at 240 K. After an equilibration time of 2 ns, the thermostats applied to the surface and the liquid region were turned off, while the thermostat applied to the seeding ice slab remained for the remaining part of the simulation to prevent it from melting. Given that the planar area of the ice interface is larger than ten molecular diameters in each direction, the simulations are not expected to have finite size effects on the interface properties (Conde *et al.*, 2008). In appendix A, the LAMMPS script for a sample simulation case is provided.

| $\varepsilon_{ss}$ (kcal/mol) | $\varepsilon_{so}$ (kcal/mol) | $\sigma_{ss}$ (Å) | $\sigma_{so}$ (Å) |
|---|---|---|---|
| 6 | 1.12 | 2.573 | 2.870 |
| 0.91 | 0.44 | 2.573 | 2.870 |
| 0.27 | 0.24 | 2.573 | 2.870 |
| 0.017 | 0.06 | 2.573 | 2.870 |

**Table 4.2:** Table showing the different solid-solid (ss) and solid-water (so) Lennard-Jones interactions tested in all three MD surfaces in this chapter. The $\sigma_{ss}$ (also $\sigma_{so}$) was fixed for all cases. Lorentz Berthelot mixing rules were used to calculate columns for $\varepsilon_{so}$ and $\sigma_{so}$.

## 4.2 Contact angle measurements for all surfaces

Consistent with previous MD studies, the calculation of the contact angle in MD simulations was designed to mimic experimental procedures. 2D axisymmetric slices of the droplet were taken, in which density was measured. This density was evaluated from the coordinates of all oxygen atoms, assuming axisymmetry around a centroidal axis normal to the solid surface (see section 3.6.1). The whole domain was divided in cells, each of size 1 Å and the local number density of every subcell was calculated. The interface of the droplet varied from bulk to vapour, and isocontour lines were fitted to the density field. Then, the isocontour with 50% of the bulk liquid density was chosen, and using a circular fit the tangent near the wall surface was drawn giving the contact angle. This process was then repeated for three droplet sizes, comprising of 5000, 8000, and 11000 molecules, respectively. The exception was the very low-energy surfaces ($\varepsilon_{ss} = 0.017$ kcal/mol) for which a larger droplet comprising 30000 molecules was used (as the smaller droplet cases tended to lift off the surface spontaneously). Negligible variation in measured values of $\theta$ was observed for all droplets in all cases, confirming that the measurements reported here are independent of droplet size.

Figure 4.2 shows the variation of contact angle $\theta$ with $\varepsilon_{so}$ for FCC, BCC and HCP respectively (the case with $\varepsilon_{ss} = 6$ kcal/mol is excluded for all surfaces as it corresponds to $\theta \sim 0^{\circ}$). It is important to make clear that, once a value of $\varepsilon_{ss}$ is chosen that is high enough that it correspond to $\theta \sim 0^{\circ}$, further increases to $\varepsilon_{ss}$ increase the interaction strength but this is no longer reflected in the contact angle measurement. However, the increase in $\varepsilon_{ss}$ past this threshold only produces minor changes in the plotted density, as seen in figure 4.3. More specifically the small variations are only observed in the height of the peak in the first overlayer. The physical significance of this is that there is a small difference in the number of water molecules occupying the same volume (since

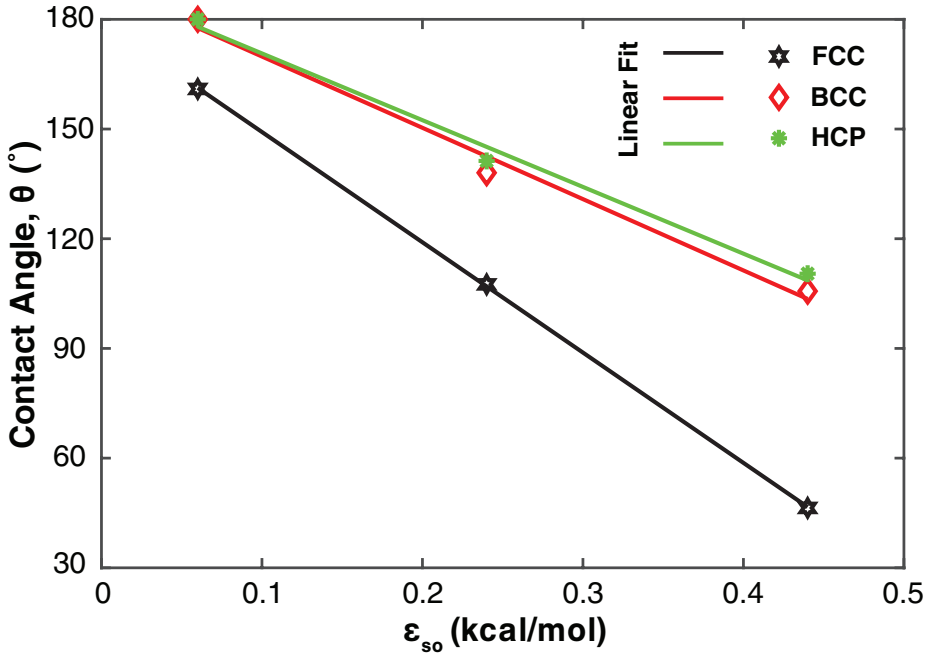


**Figure 4.2:** Macroscopic contact angles of water droplets on different surfaces (FCC, BCC, and HCP) when varying the solid-water interaction potential $\varepsilon_{so}$.

the thickness of the first peak is the same). Finally, as can be seen in figure 4.3 these rate of change of first overlayer height reduces as the values of $\varepsilon_{ss}$ is increased.

It is clear that $\theta$ monotonically decreases with increasing $\varepsilon_{so}$ for all three surfaces. However, the linear fit shows that the rate of decrease of $\theta$ is steeper for FCC when compared to BCC and HCP (which have similar slopes). This indicates that the wettability of the surfaces depends not only on the surface energy but is also affected by the crystal morphology. In fact for $\varepsilon_{ss} = 0.91$ kcal/mol the FCC surface becomes hydrophilic ($\theta \sim 46°$, i.e much lower than 90°), while the BCC and HCP remain conventionally hydrophobic with $\theta > 90°$. These differences likely arise from the fact that, for the same structure, the FCC surface is denser with more atoms than the other two surfaces. As a result, the same value of $\varepsilon_{so}$ results in a greater attractive force for the droplet placed on the FCC surface when compared to BCC/HCP surfaces, thus reducing the contact angle (see figure 4.2). This indicates that there is a critical value of $\varepsilon_{so}$ for a hydrophilic to hydrophobic transition, which depends on the crystal morphology of the surface. Therefore, to disentangle the effects of crystallography from wettability, $\theta$ is instead used and not $\varepsilon_{so}$ for all results presented in this chapter.

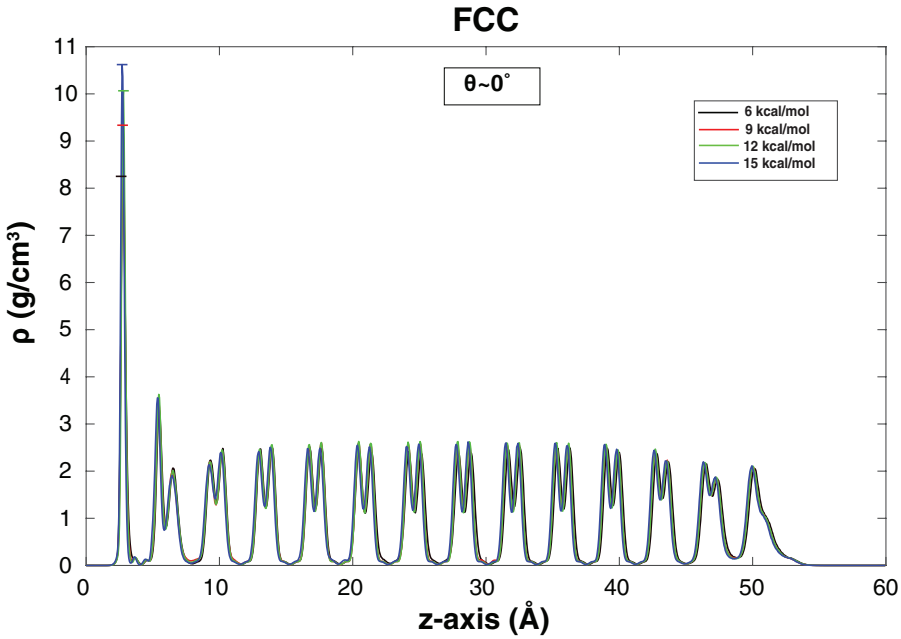


**Figure 4.3:** Steady-state density profiles according to different values of $\varepsilon_{ss}$ that correspond to $\theta \sim 0^{\circ}$.

## 4.3 Density profiles of interfacial layers

### 4.3.1 Mechanisms involved in freezing

When we consider tetrahedral molecules such as water, structural order between groups of molecules can be quantified by an 'order parameter'. An order parameter quantitatively compares the water molecules with relevant crystalline structures containing local tetrahedral coordination (Russo and Tanaka, 2012). Using this comparison, one can distinguish ice molecules from supercooled water, as ice molecules are arranged in an ordered crystalline structure. Order parameters for water take into account the structure of water up to the second nearest-neighbour shell, defined in terms of the hydrogen bond network (HBN). Water molecules initially agglomerate at nucleation sites, and then connect to each other using hydrogen bonds, leading to the evolution of a HBN. Thus, the formation of a stable HBN is is strongly associated with the presence of ice nuclei. The presence of the surface tends to both promote and inhibit ice nucleation through two competing physical phenomena both of which involve the HBN: a) the interactions of the surface and water break the hydrogen bonds between water molecules, thus destabilising the HBN; b) however, as the same interactions also modify the position and orientation water molecules at the interface, they can generate a configuration of orderly hydrogen bonds (in the form of hexagonal structure), and

as a result accelerate the HBN development. Therefore, ice formation relies on the competition between these two distinct surface effects on the HBN (Li *et al.*, 2017).

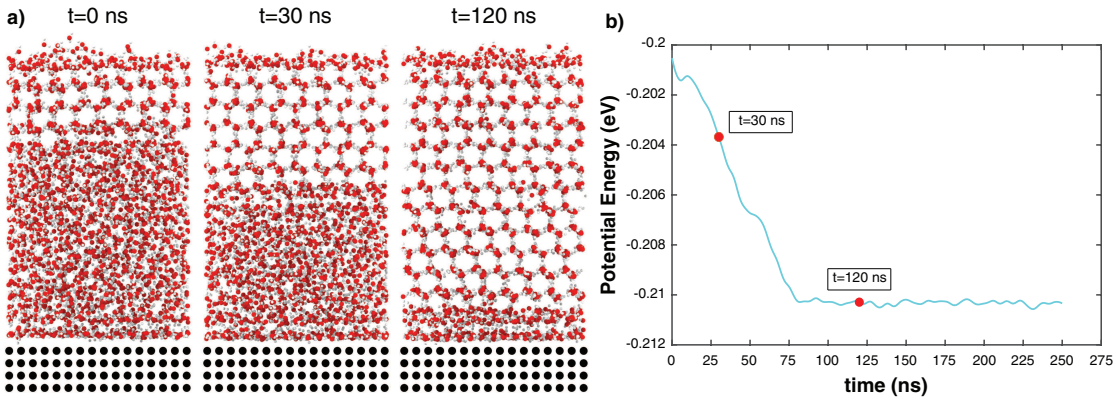


**Figure 4.4:** a) MD time-lapse of the ice growth process near a solid surface using the top-down ice-slab seeding approach. b) The mean molecular potential energy of water molecules during phase transition from liquid to solid. A plateau in the potential energy is reached when freezing is completed; steady state measurements are taken within the plateau.

Figure 4.4 illustrates the freezing process for a typical case in this chapter. In figure 4.4a, the simulation is initiated (at $t = 0$ after initial equilibration) with an ice seeding slab directly in contact with the supercooled water below it. The subsequent time evolution shows that the ice front propagates towards the surface, eventually reaching it. The potential energy of the water molecules during the freezing process is shown in figure 4.4b. As expected, the drop in density of the water from the liquid state (0.993 $\mathrm{g/cm^3}$) to the solid state (0.909 $\mathrm{g/cm^3}$) results in a corresponding decrease in the potential energy of the system as seen in figure 4.4b, until it reaches a final steady state value at roughly $t = 80$ ns. This corresponds to the completion of the freezing process as all available water molecules have been transformed into a hexagonal ice structure (see image at $t = 120$ ns in figure 4.4a). There is a small layer of liquid-like molecules at the bottom even though the system is at steady state; this results from the influence of the surface on the HBN and will be discussed in more detail in later sections.

### 4.3.2 Molecular arrangements in the interfacial region

As the intermolecular forces studied here act at the nanoscale, the molecular structure of the interface gains importance. The interfacial dynamics do not, in reality, occur on the surface but over a region less than a few nanometres thick adjacent to the surface. The first few layers of water at the surface-ice interface are required to bind to both to the structure of the metal surface below as well as the bulk ice above. Inside bulk ice, water molecules typically are arranged into a hexagonal network, with molecules oriented to optimise hydrogen bonding with layers above and below. This is commonly known as an ice *bilayer* when viewed from the basal face, as two peaks are observed in the density distribution (see 4.5), each corresponding to the most probable location of the oxygen atoms (with the hydrogen atoms concentrated in the valley between the peaks). However, pristine ice bilayers showing well-developed double peaks are not observed in the interfacial region (Björneholm *et al.*, 2016). Instead, depending on the type and temperature of the surface, water can form any number of one-dimensional chain networks (pentamers, hexamers, etc) or two-dimensional HBNs (commonly known as *buckling*). Typically, the molecular structure of the surface greatly influences the layer of water adjacent to it, known as the *first overlayer*. Between the first overlayer and bulk ice, there are usually one or more *intermediate layers* which are closer in structure to the bulk ice bilayer, but still distinct from it due to the influence of the surface and the first overlayer (Carrasco *et al.*, 2012).

The complex balance between water-water and water-surface interactions produces diverse molecular arrangements in interfacial layers. For example, on surfaces to which water molecules bond very strongly, such as ruthenium (a reactive metal), experiments have observed 1D flat (or planar) hexamers in the first overlayer. These hexamers optimise the interaction between the water and the metal molecules, as all water molecules in the first overlayer are placed as close to the surface as possible (Haq *et al.*, 2006). In contrast, on metals for which the bond with water molecules is weaker, such as copper and silver (noble metals like the surfaces simulated in this chapter), 2D buckled hexamers are favoured; buckled structures optimise the bonding within the water molecules (Michaelides and Morgenstern, 2007). The transition between a flat (1D) to a buckled (2D) first overlayer results when water molecules favour bonding to each other over bonding to the surface.

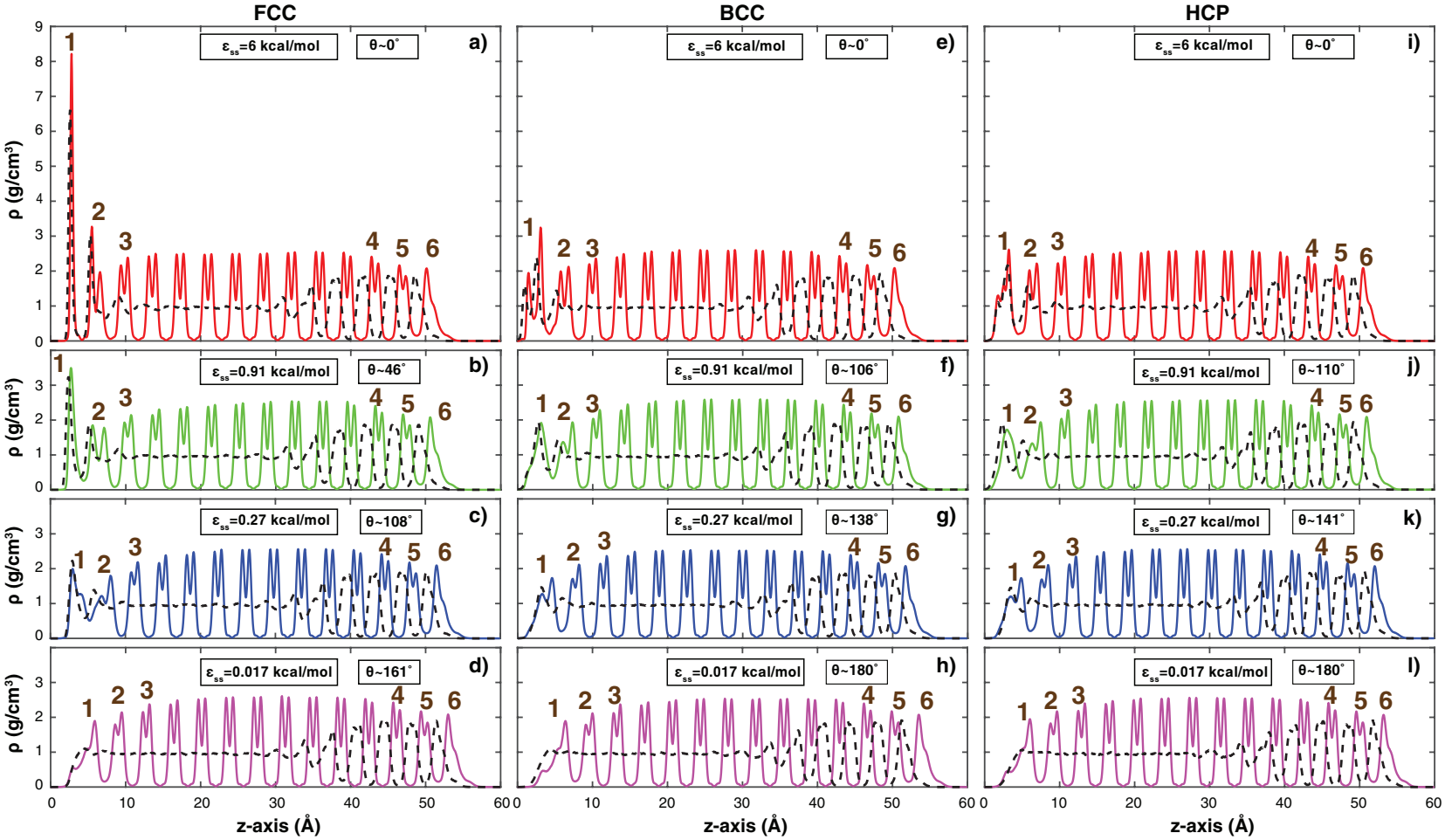


**Figure 4.5:** Steady-state density profiles organised according to $\theta$ (rows) and surface topography (columns) after freezing. For example, figures a-d are the density profiles on an FCC surface for increasing wettabilities. The dotted lines represent the density profiles of liquid water before crystallisation and the solid lines represent the steady state profiles. The numbers 1-6 inset in each graph represent the layers closest to the surface (1-3) and vapour (4-6) interface, respectively, which are subject to investigation.

### 4.3.3 Overview of the density distribution

This understanding of the interfacial region structures is highly-relevant to the results presented in this chapter. In figure 4.5, the steady-state density is plotted for frozen water on all surfaces (FCC, BCC, HCP) for all contact angles (going from superhydrophilic to superhydrophobic) considered in this work. Note that the black dotted lines, representing the density of the supercooled water prior to the initiation of the freezing process, is also provided for reference. All steady-state properties reported in this work were obtained by averaging results for 80 ns after the potential energy had become constant (as freezing had completed). To compute density, the domain was divided along the $z$-axis into 1100 cells, and number of molecules in each cell was divided by the cell volume.

To facilitate discussion, the interfacial region at both the surface-ice and ice-vapour interfaces have been separated into three distinct layers each, which comprise the first overlayer and any intermediate layers. As can be seen in figure 4.5, they are labelled from $1-6$, with 1 being the closest to the surface and 6 closest to the vapour region. The reason these layers are of interest is because they are not identical to the bulk region of water (liquid or solid). Additionally, in the absence of a surface, layers 1, 2 and 3 would be identical to layers 6, 5 and 4, respectively. Therefore the differences between corresponding layers can also help shed light on the influence of the surface on the interfacial region.

Focusing on the FCC surface first (figures 4.5a-d), a few observations can be made:

1. In figures 4.5a, 4.5b, for low values of the contact angle ($\theta \sim 0^\circ$ and $\theta \sim 46^\circ$), i.e for superhydrophilic and hydrophilic FCC surfaces, the peak in layer 1 is very sharp and appears at $\sim 2$ Å from the surface, indicating a flat first overlayer where the water molecules bind strongly to the surface due to its high wettability (despite the surface not being reactive). While the peak height varies in figure 4.5a and figure 4.5b as $\theta$ increases, in both cases the unimodal peak corresponds to the first hydration layer. For increasing values of $\theta$, the height of layer 1 peak is strongly reduced. Thus, the density of the flat first overlayer decreases as the surface wettability decreases.
2. In figure 4.5c ($\theta \sim 108^\circ$) the peak of layer 1 occurs at $\sim$2 Å and a smaller shoulder is seen at $\sim 3$ Å, while in figure 4.5d ($\theta \sim 161^\circ$) the inverse is observed, with a shoulder at $\sim$2 Å and layer 1 peak at $\sim$5 Å. This implies that the first overlayer has now *transitioned from a flat to a buckled configuration*, as hydrogen bonds between layers of water begin to be favoured as wettability is reduced.

3. The appearance of well-developed double peaks, representing the formation of ice bilayer structure, occurs further from the FCC surface, approximately at 10 Å in figures 4.5a, 4.5b. These bilayers are observed at 12 Å from the surface in figures 4.5c and 4.5d, implying that the ice bilayer starts further from the surface as $\theta$ is increased.
4. Comparing the density profiles of ice with that of supercooled water over the four modified FCC surfaces before freezing (dotted black line), it is observed that the density of ice and water are similar very close to the surface, and only start to differ at $z > 4$ Å. This indicates that the molecules closest to the surface are minimally influenced by the freezing process, and their structure is largely determined by the surface-ice interface regardless of whether they form part of supercooled water or ice.

Figures 4.5e-l show the density profiles over the other two structures, BCC and HCP. There is a key difference when compared to FCC, which is that the first overlayer is not flat for any of the wettabilities studied, and some type of buckling is always observed. Layer 1 on the superhydrophilic BCC and HCP surfaces is consequently thicker than that of the FCC with a first peak at $\sim 1.2$ Å and a second peak almost double in height at $\sim 3$ Å, and the onset of double peaks starting at $\sim 6$ Å. In figures 4.5f, 4.5j ($\theta \sim 106^\circ$ and $\theta \sim 110^\circ$, respectively) the hydrophobic layer 1 has a large peak at $\sim 3$ Å, and layer 2 comprises a degenerated double peak consisting of a shoulder at $\sim 6$ Å and a peak at $\sim 7.5$ Å.

Well-developed double peaks (indicating ice bilayers) are observed on BCC/HCP surfaces at $\sim 10$ Å and beyond. Comparing the profiles beyond 12 Å, a small shift towards the right of the profile in figure 4.5j is noted, but for the others, BCC and HCP shows similar profile to FCC with equal distance between the bilayers ($\sim 3.8$ Å) and similar bilayer height. Comparing the density profiles over BCC and HCP surfaces, for increasing values of $\theta$, layer 1 is observed to move further away from the surface (i.e. towards larger values of $z$), indicating the first overlayer is situated further away from the surface. Moreover, when compared to the density profile of supercooled water, differences are observed on the superhydrophobic surfaces at $z \sim 3$ Å, which is lower when compared to superhydrophilic surfaces. This can be understood from the waning influence of the surface on the molecules near it as wettability is reduced, and the intermolecular interactions between the surface and water become weaker.

In summary, the decrease of $\varepsilon_{so}$ results in a decrease in the first overlayer density (lower layer 1 peak), as the surface is unable to accommodate the same number of liquid

molecules. Additionally, the density of the surface also plays a role. As discussed in section 3.4, the FCC surface has more atoms and therefore a higher wettability for the same value of $\varepsilon_{so}$ than BCC and HCP. As a result, there is a stronger resultant attractive force towards the water molecules producing a flat first overlayer for FCC, which eventually transitions to a buckled overlayer at lower wettabilities. Note that the differences observed in the steady-state density profiles in figure 4.5 are limited to the vicinity of the surface-ice interface. The ice bilayers and the layers $4-6$ (which constitute the ice-vapour interface) are identical on all surfaces. This is expected since the influence of the surface wanes considerably as you get further away from it.

## 4.4 Looking closely at the layers

### 4.4.1 Density heat maps

To probe further into the behaviour of layers $1-3$, 2D density "heat maps" were created for each layer, wettability and structure. In each case, density was computed by dividing the domain of each layer along the $x$-axis and $y$-axis into 5670 cells, and number of molecules in each cell was divided by the cell volume. It has been noted in the previous section that the water molecules on a FCC structure for $\theta \sim 0^\circ$ forms a flat first overlayer. Note that water molecules in the bulk of the liquid have multiple hydrogen bonds per molecule, but this is not the case for the flat first overlayer where water-water interactions are reduced as the molecules instead adsorb to surface atoms at fixed sites. This flat structure can be understood as water maximising its interaction with the surface with only a slight cost in hydrogen bond energy. In figure 4.6, the heat map of the first overlayer is placed alongside the heat map of the FCC structure itself. It is well-known that the surface can play a key role in templating the structure of water layers adjacent to it, sometimes forcing the first layer to mimic its registry rather than that of ice (Gerrard *et al.*, 2019). Figure 4.6 shows distinct similarities between the FCC surface heat map and that of first overlayer with many FCC atoms binding adjacent water molecules, which indicate some surface templating in this layer. However, unlike the cubic structure of the surface, hexamer and pentamer rings are observed, consistent with experimental observations for water overlayers on FCC platinum surfaces (Nie *et al.*, 2010).

As we move to higher values of $\theta$, we see significant changes in layers 1 and 2 in figure 4.5. To isolate the effect of the surface, heat maps of layers $4-6$ have been produced,

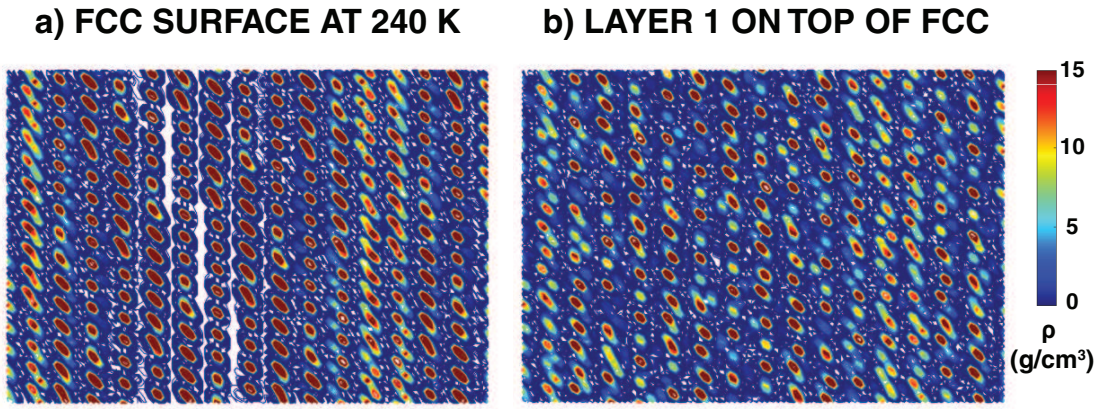


**Figure 4.6:** a) Two-dimensional heat map of the surface atoms of the FCC surface at 240 K, and b) two-dimensional heat map of water molecules in layer 1 on top of the FCC surface for $\theta \sim 0^{\circ}$ or the highest value of $\varepsilon_{so}$.

which also constitute an interface but are not within interaction reach of the surface. As was the case for density, layers 1, 2 and 3 would, in the absence of the surface, be identical to 6, 5 and 4, respectively. It can be seen in figure 4.5g-l that the intermediate layer 2 appears visually similar to layer 5 (for $\theta \geq 138^{\circ}$), as both consist of poorly-formed bilayer-like structures, with asymmetrical peaks. This implies that the surface likely plays a much weaker role in water ordering in layer 2 once $\theta$ exceeds a critical value.

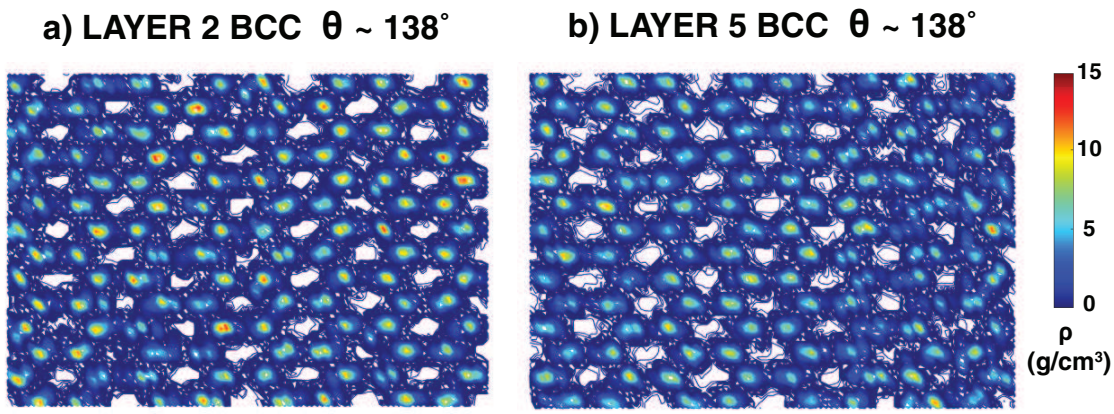


**Figure 4.7:** In the case of the second lowest $\varepsilon_{so}$ (hydrophobic surfaces), layers 2 and 5 for BCC and HCP morphologies show similarities in their density plot (see figure 4.5). This figure shows how similar the heat maps are for layers 2 and 5 in the case of just BCC.

In figures 4.7 and 4.8, heat maps are shown for layers 2 and 5 on BCC (for $\theta \sim 138^{\circ}$) and on layer 2 and 5 on FCC (for $\theta \sim 161^{\circ}$), respectively. All four heat maps broadly

show similar structures, which is somewhat expected given the similarity in the density distribution of water molecules in these layers from the relevant panels in figure 4.5. This similarity is observed despite the different crystal structure of the underlying surface, thus indicating that the registry of the underlying surface is no longer discernible. In addition, hexagonal patterns reminiscent of bulk ice start forming, with areas of extremely low density in between (coloured in white), with some defects.

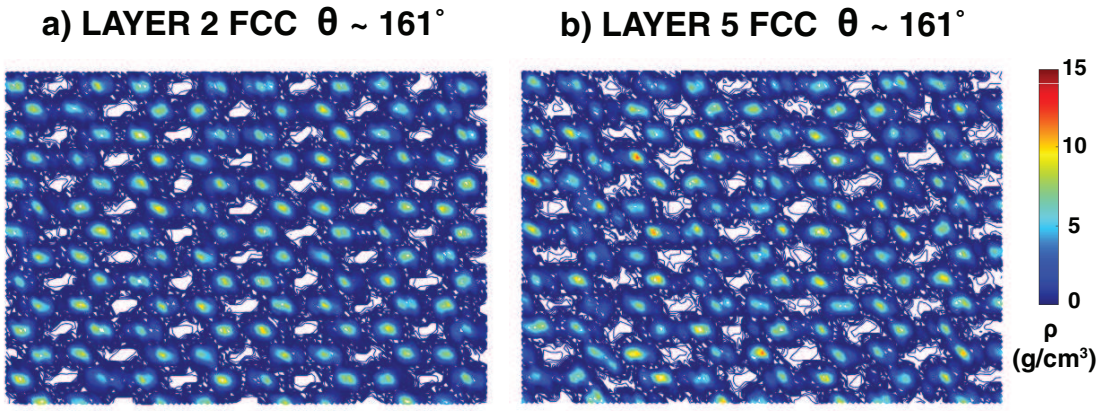


**Figure 4.8:** In the case of the lowest $\varepsilon_{so}$ (superhydrophobic surfaces), layers 2 and 5 for all structure morphologies show similarities in their density plot. This figure shows the comparison in water density heat maps for the FCC surface ($\theta \sim 161^{\circ}$) between a) layer 2 and b) layer 5. The heat maps across both layers are very similar.

When the contact angles are high enough for our surfaces to be characterised as superhydrophobic ($\theta \geq 150^{\circ}$), layer 1 starts to resemble layer 6, as seen in figure 4.5 d,h,l. Hence, it would be expected that the surface-ice interface heat maps resembling those for the ice-vapour interface. To confirm this, heat maps of layer 1 and 6 of water molecules on the HCP surface are presented in figure 4.9. No structure or patterning is observed, indicating that these layers feel neither the registry of the surface below it nor the ice above. This verifies that, for superhydrophobic surfaces, the surface-ice interface is nearly identical to the ice-vapour interface.

### 4.4.2 Density layering

In the previous chapter (section 3.6.5), equation (3.36) was introduced (Lupi *et al.*, 2014) to quantify the deviation of the local density of liquid water compared to the bulk density of liquid water. In this work, a different $L_1^*$ parameter is used to quantify

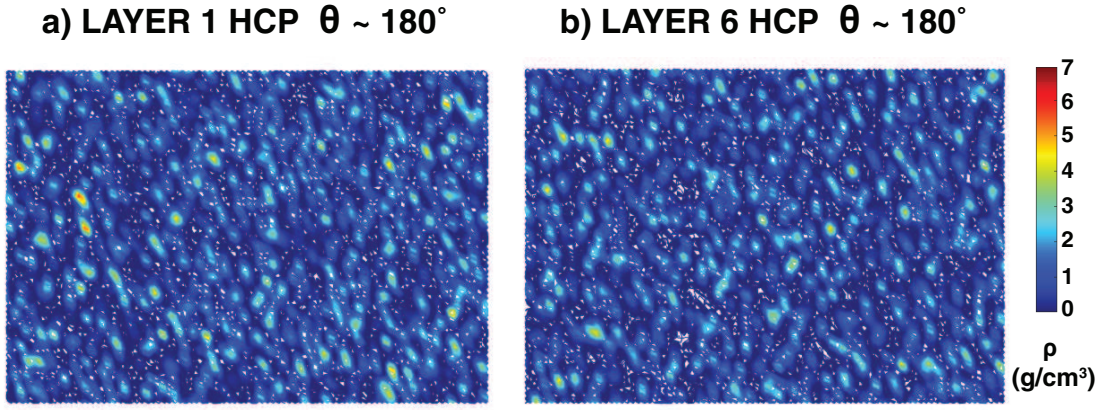


**Figure 4.9:** In the case of the lowest $\varepsilon_{so}$ (superhydrophobic surfaces), layers 1 and 6 for all structure morphologies are showing similarities in their density plot (see figure 4.5). This figure shows the comparison in water density heat maps for the superhydrophobic HCP surface ($\theta \sim 180^{\circ}$) between a) layer 1 (closest to surface-ice interface) and b) layer 6 (closest to ice-vapour interface). The heat maps across both layers are very similar.

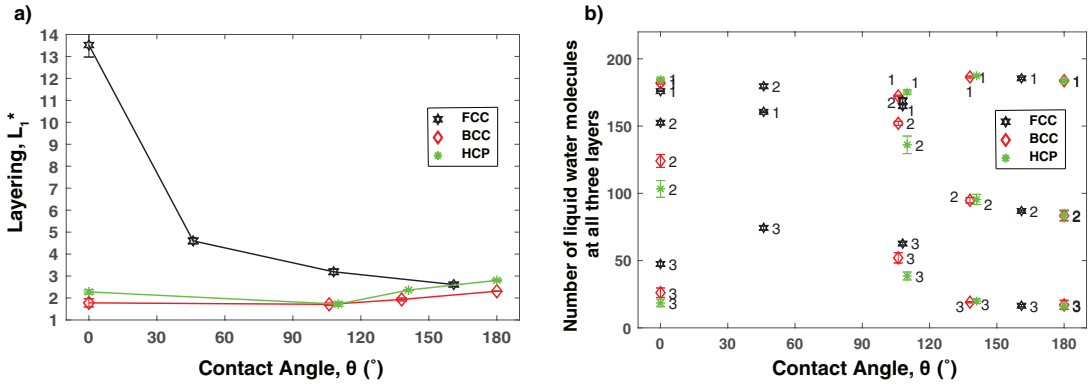


**Figure 4.10:** a) Layering of liquid water molecules before crystallisation starts, in layer 1. b) Number of non-ice molecules in all three surfaces for all wettabilities; indices inset indicate the layer number as defined in figure 4.5.

the density layering in the region comprising layer 1 using the formula:

$$L_1^* = \int_0^{z_{layer1}} \left( \frac{\rho(z)}{\rho_{bulk}} - 1 \right)^2 dr, \tag{4.3}$$

where $\rho$(z) is the local density of water at a distance $z$ above the surface, $\rho_{bulk}$ is the density of bulk liquid water and $z_{layer1}$ is the distance from the surface at which layer 1 ends. Figure 4.10a shows the average values of $L_1^*$ on FCC, BCC and HCP structures for all wettabilities. For $\theta < 90^{\circ}$, the previously highlighted differences in layer 1 structure between FCC and the other two surfaces are observed here as well. Note that

$L_1^*$ is very similar for BCC and HCP across the entire range of contact angles. For FCC, $L_1^*$ is much higher for the flat first overlayer at $\theta \sim 0°$, but as this transitions to a buckled overlayer as $\theta$ increases, $L_1^*$ starts to decrease and approach the corresponding values for BCC/HCP.

While the discussion so far has focussed on the first overlayer across surfaces and studying the transition from flat to buckled configurations, it is important to note that the thickness of this layer, $t_L$, is slightly different for the three surfaces, with FCC having the highest local layer density ($t_{L,FCC} = 4.1$ Å, $t_{L,BCC} = 4.3$ Å and $t_{L,HCP} = 4.4$ Å). This means that the greater wettability of the FCC surface creates a denser and thinner surface coverage. Figure 4.10b quantifies this, by plotting the average number of non-ice molecules in layers $1-3$ for all structures and wettabilities. Despite the significant difference in $L_1^*$ of layer 1 between FCC and BCC/HCP for $\theta \sim 0°$, the number of non-ice molecules in layer 1 is similar ($\sim 180$) in all three surfaces. This indicates that the FCC surface is capable of adsorbing and saturating the first overlayer to a greater degree especially in the flat configuration, and this layer is adsorbed closer to the surface when compared to BCC/HCP.

In conclusion, this section focused on analysing the density profiles, heat maps, and density layering of the interfacial layers of water. The interfacial region was found to consist of a first overlayer and additional intermediate layers. A flat to buckled transition was observed on the FCC surface as $\theta$ was increased. The first overlayer was buckled for BCC and HCP surfaces, regardless of $\theta$. These differences arise due to the combined influence of the wettability and the crystal structure of the surfaces. To understand the transition from ice-like structures in the interfacial layers to bulk ice, we need to examine the structure of these layers in more detail, which is the goal of next section.

## 4.5 Structure of Interfacial Region

### 4.5.1 CHILL+, ice, and non-ice molecules

Thus far, the focus was on the ordering of interfacial water molecules on all three surfaces, without distinguishing between ice molecules and non-ice molecules. In this section, the CHILL+ algorithm (Moore *et al.*, 2010; Nguyen and Molinero, 2015; Sayer and Cox, 2019) was adopted to identify ice molecules using the HBN between them. In particular, CHILL+ relies on the correlation of bond-order parameters to

identify and count the number of staggered and eclipsed O-O bonds in the HBN, which distinguish hexagonal/cubic ice and non-ice molecules. Note that here the term "non-ice molecules" is used and not "liquid molecules" because not all non-ice molecules are necessarily liquid water; CHILL+ also includes any poorly-formed bilayers, or structures with pentamer/hexagonal rings that do not resemble ice.

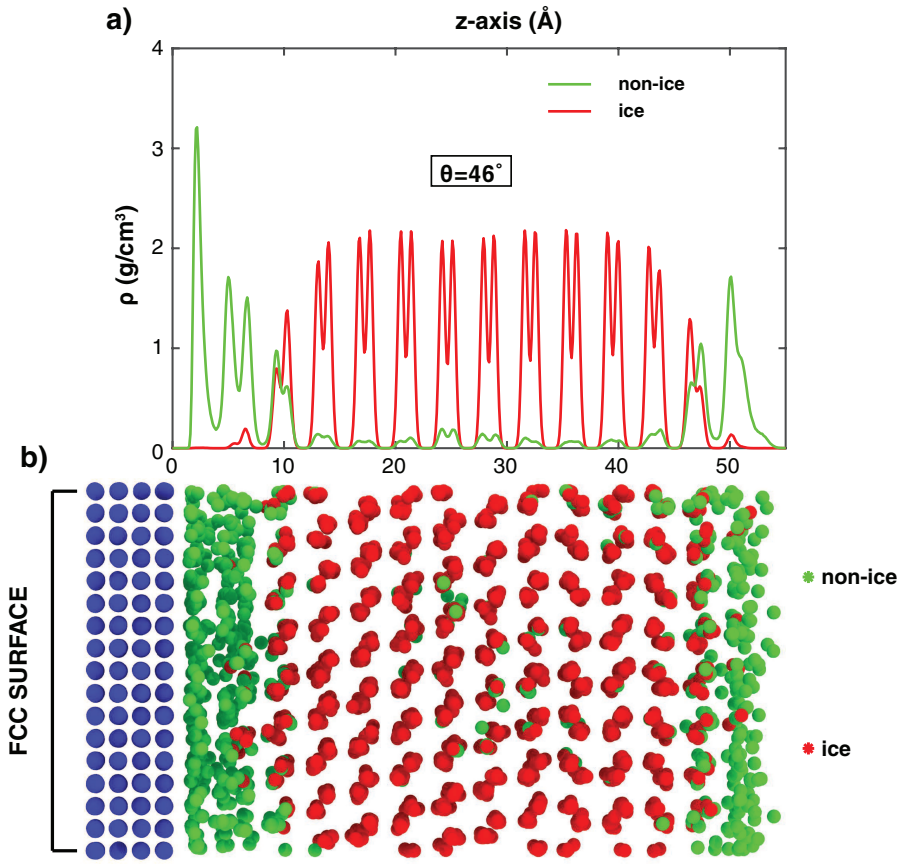


**Figure 4.11:** a) The 1D density plot of non-ice (green) and ice (red) water molecules as a function of distance from the wall using the CHILL+ algorithm, and b) an MD snapshot of their distribution in the system.

Figure 4.11 illustrates how CHILL+ is applied to a typical case (FCC, $\theta \sim 46°$). The top part of the figure is the same density plot as before, but with ice molecules separated using CHILL+. The bottom part of the figure shows the distribution of ice and non-ice molecules in the domain. The minimal presence of conventional ice molecules in the interfacial layers (between $0-10$ Å) is expected.

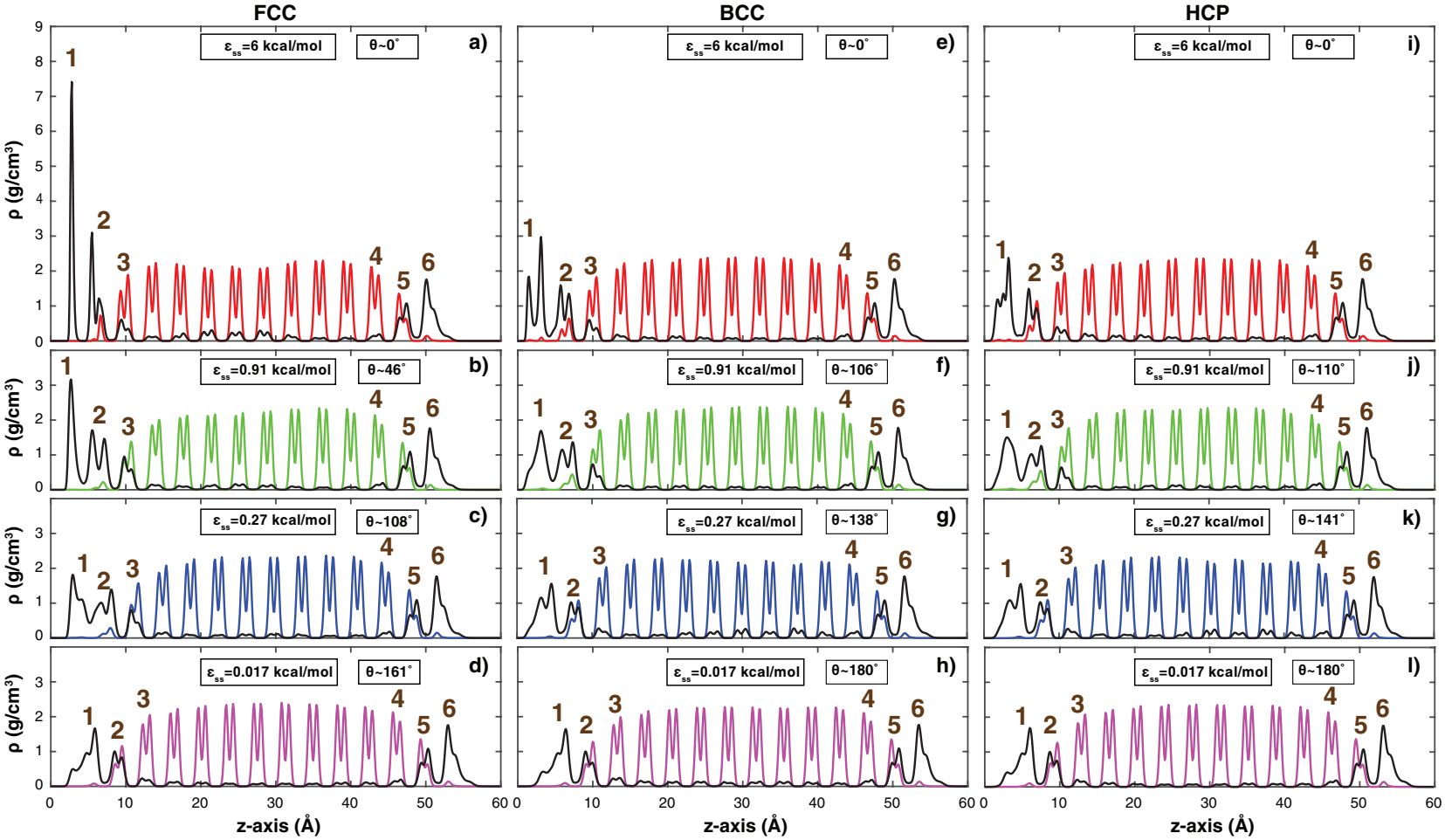


**Figure 4.12:** Steady-state density profiles similar to figure 4.5, but here the profiles are split into ice (colour solid lines) and non-ice (black solid lines) molecules using the CHILL+ algorithm. See figure 4.5 for definition of indices 1-6.

A similar zone, but reduced in size, is present in the ice-vapour interface in this instance (between $48-55$ Å). CHILL+ also identifies a few non-ice molecules in the frozen bulk region (between $20-40$ Å). This indicates the presence of defects in the formed ice, as the density plot shows that these water molecules are arranged in the form of imperfectly-developed (slightly asymmetrical) bilayers.

In figure 4.12, the water densities in figure 4.5 are replotted, but with ice and non-ice molecules separated using CHILL+ (with non-ice molecule density shown as a black line). It is apparent that layers $1-3$ near the surface-ice interface and layers 5 and 6 at the ice-vapour interface are the only layers where the majority of the molecules are identified by CHILL+ to be non-ice. Note that for the superhydrophobic cases (panels d,h,l in 4.12), layer 3 freezes as well, thus resembling the bulk ice layers. In fact, as $\theta$ increases, the surface-ice interface starts to resemble the ice-vapour interface. Once we reach the superhydrophobic cases, we see that layer 1 resembles layer 6 in all three cases (recall figure 4.9), showing the expected absence of attractive forces from the surfaces to the liquid molecules. This is why distinguishing between ice and non-ice molecules is important, as comparing the surface-ice and ice-vapour interfaces gives insight into the influence of the surface on the layers adjacent to it. For example, the heat maps for BCC layer 2 and FCC layer 5 (for $\theta \geq 138°$) are seen to be similar in figure 4.7 and figure 4.8, respectively. Here, it can be seen that the peaks forming the bilayers in layers 2 and 5 can be subdivided into a peak which is identified to be non-ice (close to either interface), and the peak identified as ice (closer to the bulk ice). This highlights both why the heat maps showed hexagonal structures but also had defects (as these layers are only partly frozen).

### 4.5.2 Quantifying quasi-liquid layers

In the previous chapter, quasi-liquid layers (QLL) were defined, and an established way of quantifying QLL in MD simulations was introduced. Essentially, the interfacial region is referred to as QLL in this work, as long as the molecules in it are not frozen (i.e. they are identified by CHILL+ to be non-ice). In cases where any molecules in any one of the three interfacial layers forms ice, it is excluded from our QLL calculations. This protocol enables the measurement of QLL thickness, providing a quantitative estimate of non-frozen molecules, and enables comparisons between the difference simulated cases. Here, two estimates of QLL thickness, $T_{\mathrm{QLL}}$ are provided, using a numerical and graphical approach, respectively, as discussed below.

### The analytical approach

The first method used to quantify QLL in MD (discussed in the previous chapter) was introduced by Conde *et al.* (2008) (see section 3.6.4). This method depends solely on the number of non-ice molecules existing in the interfacial region of interest. As no previous MD simulations have quantified QLL at the surface-ice interface, the $T_{\mathrm{QLL}}$ at the ice-vapour interface is used as a reference value for comparison. Figure 4.13a plots $T_{\mathrm{QLL}}$ at the surface-ice interface (symbols) and ice-vapour interface (blue dotted line) for all surfaces and wettabilities.

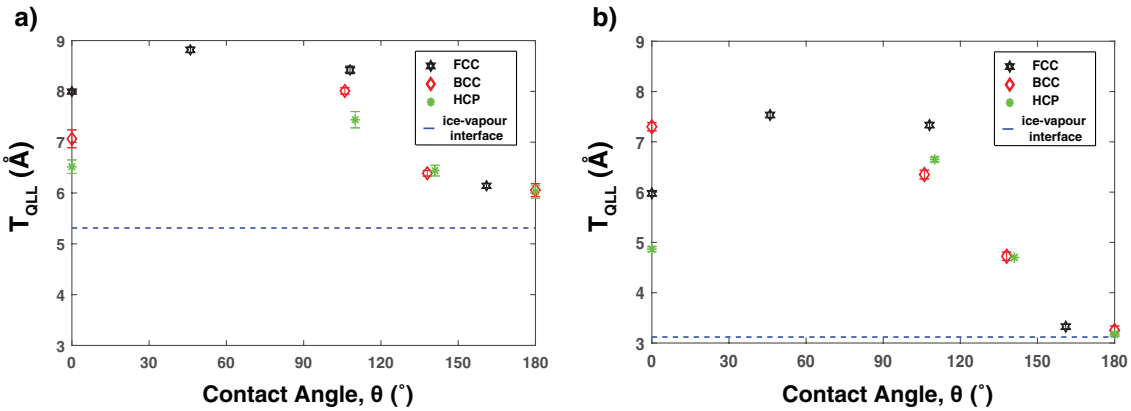


**Figure 4.13:** The thickness of the quasi-liquid layer, $T_{\mathrm{QLL}}$, is plotted using: a) the analytical approach, and b) the graphical approach. In both cases, the blue dotted line shows the corresponding value of $T_{\mathrm{QLL}}$ at the ice-vapour interface.

### A graphical approach

The second method used to estimate $T_{\mathrm{QLL}}$ is a graphical approach illustrated in figure 4.14, which relies on the density plots in figure 4.12. Two measurement lines are drawn in a way that the intersection point determines the location where the non-ice molecules end, which then gives $T_{\mathrm{QLL}}$. The first line is drawn from the last peak for which non-ice molecules exceed ice molecules, and pointed towards the next peak of non-ice molecules away from the surface. The second line is drawn from the first peak where ice molecules exceed non-ice molecules and pointed towards the next peak of ice molecules towards the surface. The $z$ value of the first overlayer is then subtracted from the $z$ value of the point where these two lines meet, which gives an estimation of $T_{\mathrm{QLL}}$ (see figure 4.14 for an illustration of this process). Figure 4.13b plots $T_{\mathrm{QLL}}$ using this approach for all surfaces and wettabilities, with the ice-vapour interface results again plotted as a dotted blue line.

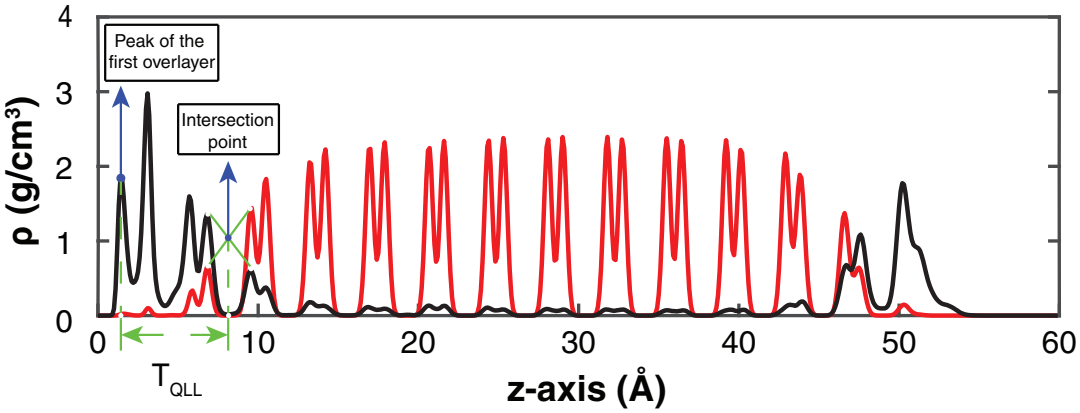


**Figure 4.14:** Schematic of the graphical approach to estimate $T_{\mathrm{QLL}}$ for the BCC surface for $\theta \sim 0^{\circ}$.

Both approaches produce similar results, with $T_{\mathrm{QLL}}$ shown to be higher for moderate values of $\theta$ (between $40^{\circ} - 120^{\circ}$) and lower for both superhydrophobic and superhydrophilic surfaces. This is an interesting result that deserves further scrutiny. For low values of $\theta$, the surface overlayer (be it flat or buckled) is strongly bonded to the surface molecules, and therefore is identified by CHILL+ to be non-ice, which then means it contributes to $T_{\mathrm{QLL}}$. Therefore, a thicker $T_{\mathrm{QLL}}$ for low $\theta$ can be understood as resulting from the fact that the surfaces force molecules in layers $1-3$ to adopt non-hexagonal configurations. What is less apparent is why $T_{\mathrm{QLL}}$ peaks for moderate values of $\theta$ and then drops off at higher $\theta$. This will be investigated in the next section.

Secondly, $T_{\mathrm{QLL}}$ is shown to approach the value of the ice-vapour interface at high values of $\theta$. This is expected as the surface plays a minimal role at high $\theta$, and this convergence can be considered to be a validation of these measurement techniques. Note that the $T_{\mathrm{QLL}}$ values approach but do not actually achieve the ice-vapour interface values. The only significant difference between figures 4.13a and 4.13b is seen at $\theta \sim 0^{\circ}$; the graphical approach indicates that $T_{\mathrm{QLL}}$ is largest on the BCC surface whereas the quantitative approach suggests that $T_{\mathrm{QLL}}$ is largest on the FCC surface.

## 4.6 Dynamics of the interfacial region

### Calculation of MSD and *D*

There have been two key observations made in the previous sections: a) a flat-to-buckled transition in the first overlayer occurs on the FCC surface as the $\theta$ is increased from 46° to 108°, while the BCC and HCP surfaces show buckled overlayers throughout; and b) the thickness of the interfacial region is largest for moderate values of $\theta$ (between $40° - 120°$), and is lower for superhydrophobic ($\theta \geq 160°$) and superhydrophilic ($\theta \sim 0°$) surfaces. To clarify these two points further, additional investigation into the dynamics of the interfacial region is conducted in this section. This is achieved by estimating the self-diffusion coefficient $D$ for each layer in steady state using the mean square displacement (MSD) formulas detailed in section 3.6.2.

The MSD was calculated separately for layers $1-3$ by averaging over the molecules that belong to each layer. Note that molecules can freely travel between the layers during this measurement, but the entrance and exit times for each molecule as it moves between layers are tracked, allowing for an accurate estimate of MSD. This means that if a molecule leaves the layer, it stops being incorporated into the MSD calculation at that exact timestep. Instead, its velocity contributes to the MSD of the layer it has entered. If this molecule then re-enters the original layer at a future timestep, its entry point is treated as the starting position for MSD calculations for that timestep. Thus, all the molecules within a given layer are included in the MSD calculation. Additionally, to reduce noise that is inevitable when calculating MSD for a long simulation time, the MSD is calculated separately for every 1 ns. This means that each and every nanosecond produces a separate calculation of the MSD.Then these individual values are then averaged at the end of the measurement period of 80 ns. As the MSD is approximately linearly over time when the system is in steady state, then $D$ can be calculated from the slope of the MSD plot. Validation of the method described above was performed by calculating $D$ for bulk supercooled water at 240 K, and the value obtained ($D = 0.199 \times 10^{-9}$ m$^2$/s) is close to the experimental value of $D_{exp} = 0.204 \times 10^{-9}$ m$^2$/s at 239.8 K (Price *et al.*, 1999).

As discussed in section 3.6.2, the self-diffusion coefficient $D$ is a direct measure of the mobility of water molecules. A high value of $D$ implies that there is significant molecular motion, whereas a very low value of $D$ implies that molecules are locked into a crystalline structure (for example, in a solid). Figure 4.15 shows the values of $D$ for all surfaces and wettabilities. For reference, the values of $D$ for layer 5 and

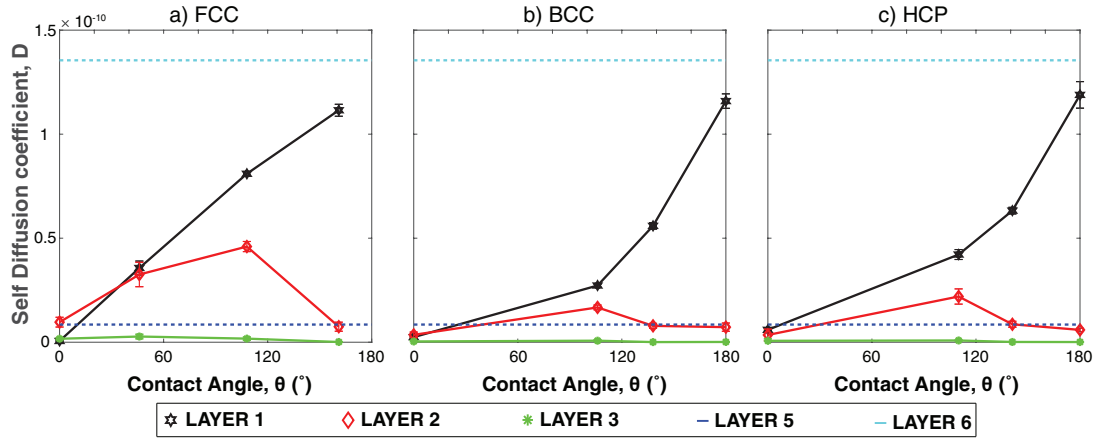


**Figure 4.15:** The self-diffusion coefficient $D$ plotted for all values of $\theta$ for layers $1-3$ on a) FCC; b) BCC; and c) HCP surfaces. The $D$ values of layers 5 and 6 are provided as dotted lines for comparison.

layer 6 (at the ice-vapour interface) are also included. Note that as layer 5 and 6 are unaffected by the surface, their respective $D$ values are constant ($D = 8.486 \times 10^{-12}$ $\mathrm{m}^2/\mathrm{s}$ and $D = 1.355 \times 10^{-10}$ $\mathrm{m}^2/\mathrm{s}$, respectively). At the surface-ice interface, $D$ for layer 3 is similarly almost unaffected by $\theta$ or surface type, and fluctuates around $D = 1.277 \times 10^{-13}$ $\mathrm{m}^2/\mathrm{s}$. On the other hand for layers $1-2$ (first overlayer and intermediate layer), the surface influences the self-diffusion characteristics significantly, and a strong dependence on $\theta$ is seen.

### Untangling the effects of surface templating

Focusing on layer 1 first (plotted as black lines in figure 4.15), the variation of $D$ as surface wettability $\theta$ is varied is qualitatively similar for all three surfaces; $D$ is negligible at low $\theta$, and rises with $\theta$ with its highest value of $D$ for the superhydrophobic surfaces considered here. Essentially, the molecules in the first overlayer are solid-like at low $\theta$ ($D \sim 0$) as they are strongly adsorbed onto the surface atoms. However, as the influence of the surface atoms wanes (as $\theta$ increases), these molecules are freed from their binding sites, gain mobility, and move more freely, resulting in a rising $D$. Thus, the higher the wettability of a surface, the lower the mobility the molecules will have in the first overlayer. However, there are quantitative differences between the FCC surface and the BCC/HCP surfaces. For the FCC surface, the slope of $D$ with $\theta$ appears almost linear, whereas both the BCC and HCP surfaces show a power-law behaviour, with a steep rise in $D$ as $\theta$ is increased from $100^\circ - 180^\circ$. For superhydrophobic cases, the surface-ice interface resembles the ice-vapour interface as previously mentioned,

and this is reflected in the values of $D$ as well.

Moving on to the intermediate layer 2 (plotted as red lines in figure 4.15), the variation of $D$ with $\theta$ is more complex. $D$ is almost negligible for both extremely low ($0^\circ$) and extremely high ($160^\circ$ and above) values of $\theta$. In between those extremes, non-monotonic behaviour is observed, with a rise in $D$ as $\theta$ is increased from $0^\circ - 100^\circ$, and then a subsequent drop in $D$ beyond that when $\theta$ rises from $100^\circ - 180^\circ$. Conceptually, this can be understood as resulting because of two competing mechanisms: a) the surface and the first overlayer (collectively called the surface *templating layers* here) attempting to structure layer 2 from below, and b) the ice-like layer 3 structured like bulk ice (collectively called the *freezing layers* here) attempting to freeze it from above. The value of $\theta$ determines the relative strength of these two effects. At very low values of $\theta$, the layers are dominated by surface templating, resulting in a highly structured solid-like layer 2. Similarly, at very high values of $\theta$, the surface has very little influence, and it is instead the freezing layer 3 that structures layer 2 into an ice-like structure. In either of these extreme cases, when the freezing layers or the templating layers dominate, the mobility of the water molecules is greatly hindered. This reduces the number of possible configurations the water molecules in layer 2 can explore, as they are constrained to specific binding sites. These sites correspond to either the location of surface/overlayer atoms (low $\theta$) or a structured ice-like HBN (high $\theta$). Hence, $D \to 0$ when $\theta \to 0^\circ$ or $\theta \to 180^\circ$.

However, for moderate values of $\theta$, both the templating and the freezing layers are of similar importance, and as a consequence, layer 2 molecules are not strongly manipulated by either effect. This means that the motion of these molecules is not hindered that significantly, and they are able to continuously move in and out of template-like and ice-like configurations. This is reflected in their higher mobility, and therefore a higher $D$, which appears to peak at $\theta \sim 100^\circ$. Note that this competition between the templating and the freezing layers is also seen in the non-ice molecule count in figure 4.10b. Looking at the variation in non-ice molecule count for layer 2 with $\theta$, it is clear that it drops significantly as $\theta$ increases and the freezing layers gain importance. This therefore explains one of the two key observations, which is why $T_{\mathrm{QLL}}$ peaks at moderate values of $\theta$. It is now clear that this change in $T_{\mathrm{QLL}}$ is driven primarily by changes in layer 2. Note that layers 1 and 3 in figure 4.10b do not show the same variation with $\theta$ as there is no surface-mediated freezing occurring in these layers.

### Understanding layer 2 on the FCC surface

While the above explanation is sufficient to explain the qualitative nature of the three MSD plots, it still does not touch on the quantitative differences *between the surfaces*, as $D$ is far higher in layer 2 for FCC when compared to the other surfaces. This can be understood by the structural uniqueness of the FCC surface, which produces a flat overlayer at low $\theta$ and a transition to a buckled overlayer at higher $\theta$. It is crucial to appreciate that the dynamic behaviour of water molecules in a flat overlayer is distinct from that in a buckled overlayer. In a flat 1D overlayer, the water molecules are restricted to motion in a particular plane, and the space that the molecules can explore is effectively reduced by one dimension relative to the layers above. This means that they bind more effectively to any adsorption sites available on the surface, which impacts upon the structure of the water molecules in the layer above it. Specifically, the molecules in layer 2 experience a much smoother energy landscape, and the locations of the surface atoms are more smeared out when compared to the BCC/HCP surfaces.

This is evident in figure 4.16 where density heat maps of layer 2 of the interfacial region on the FCC surface is compared to that on the BCC and HCP surfaces. To remove any effect of wettability and ensure that the differences observed result from the surface structure, cases with very similar wettabilities are selected for all surfaces ($\theta$ between $106-110^{\circ}$). It is clear that the FCC surface produces far fewer binding sites for the water molecules, as both the BCC and HCP surfaces show some degree of water ordering in layer 2, whereas the FCC structure has minimal ordering. This means that the mobility for molecules in layer 2 of FCC is less hindered by the corrugations in the overlayer below, allowing for greater mobility (and thus a greater $D$). An important consequence of this result is that FCC surfaces are not representative of all crystalline structures; indeed they behave very differently from the BCC and HCP surfaces studied in this chapter. In particular, they demonstrate a flat-to-buckled transition in the first overlayer with $\theta$ and a comparative lack of ordering in the second layer allowing for greater $D$ for middle values of $\theta$. This is not observed for BCC and HCP surfaces.

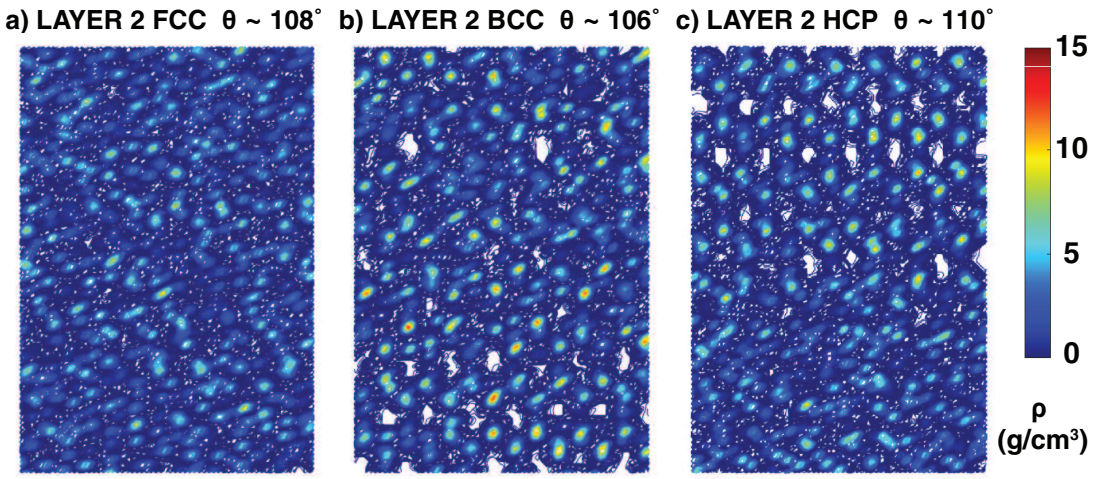


**Figure 4.16:** Density heat maps for layer 2 on a) the FCC surface with $\theta \sim 108°$, b) the BCC surface with $\theta \sim 106°$, and c) the HCP surface with $\theta \sim 110°$.

## 4.7 Conclusions

In this chapter, slab-seeded ice growth was studied on a selection of crystalline structures using a novel slab-seeding approach, which involved sandwiching supercooled water between a seeding ice slab and the surface. This enabled ice growth to be successfully observed on FCC, BCC, and HCP surfaces. The effect of surface wettability was tested by varying the surface-water interatomic potentials $\varepsilon_{so}$. It was shown that the relationship between $\varepsilon_{so}$ and the contact angle $\theta$ was surface-dependent; in particular the FCC surface consistently showed lower contact angles for the same value of $\varepsilon_{so}$. This was attributed to the greater density of the FCC surface, which meant that the number of solid-liquid interactions are larger.

Looking at the densities of the water post-freezing on all surfaces, it became apparent that the FCC surface also differed in terms of the structure of the first hydration layer, or the first overlayer, on it. The first overlayer was always buckled for the BCC and HCP surfaces; in contrast, the FCC surface induced a flat first overlayer for high wettabilities ($\theta < 50°$), and this transitioned to a buckled overlayer as the wettability was decreased ($\theta > 100°$). It was also shown that the number of molecules contained in the first overlayer was similar for all three surfaces, but the FCC is able to suppress water-water hydrogen bond formation and accommodate them in one single flat layer at high wettabilities, whereas the other surfaces were unable to do so and formed buckled overlayers instead.

The molecules in the interim region were separated into water and ice molecules using

CHILL+, and the thickness of the interfacial region was quantified ($T_{\mathrm{QLL}}$). It was shown that $T_{\mathrm{QLL}}$ peaked for moderate wettabilities, and decreased for both extremely high and extremely low wettabilities. When the self-diffusion coefficient $D$ for the interfacial layers was calculated, a similar trend was observed there as well with $D$ values peaking for moderate wettabilities and decreasing at both extremes. This can be understood as resulting from the fact that the first overlayer and the surface competed with the third layer and the bulk ice to simultaneously apply their influence on the structure in layer 2, which was found to be important when wettability was modified. For low wettabilities, the influence of layer 3 dominated and layer 2 displayed ice-like structures, whereas for high wettabilities the surface constrained the water molecules in layer 2, and they adopted positions consistent with the surface adsorption sites. In either case, $D$ of the layer 2 molecules was lowered compared to when the freezing and surface templating layers were balanced at moderate values of $\theta$. $T_{\mathrm{QLL}}$ also peaked in the same range of moderate $\theta$ as the molecules were more likely to be identified to be non-ice when they were not constrained by the surface or the bulk ice.

Finally, while the qualitative behaviour of $D$ with $\theta$ was similar across surfaces, there were significant quantitative differences. Importantly, the values of $D$ were higher in layer 2 on the FCC surface at moderate wettabilities. This was shown to result from the screening effect of the flat overlayer below, which prevented layer 2 water molecules from being bound to the surface adsorption sites. Consequently, this meant that the layer 2 molecules on the FCC surface were able to move more freely compared to their counterparts on the BCC and the HCP surfaces. This is relevant to the MD studies of heterogeneous nucleation/growth in the literature, which have been predominantly conducted on FCC surfaces. Our results show that FCC surfaces induce qualitative and quantitative differences in the interfacial region when compared to other common crystalline structures, which may be relevant depending on the application.

# Chapter 5

# Concluding Remarks

*"Any knowledge that doesn't lead to new questions quickly dies out: it fails to maintain the temperature required for sustaining life."*

- Wislawa Szymborska

This chapter concludes this thesis on the study of ice growth on metal surfaces. At the outset of this work, three important questions relating to surface icing were identified. Here, at the end of the thesis, the insights developed in this work in response to each of these questions are summarised. Some potential areas for future work are also identified.

**1. Can highly-accurate all-atom models be used to run unbiased MD simulations of icing on unfavourable surfaces?**

A new simulation methodology for surface icing, termed the "slab-seeded" ice growth method, is presented in this thesis. This approach builds on existing work (Carignano *et al.*, 2005) and overcomes the limitations of both coarse-grained and enhanced sampling methods, and does not require the surfaces to be designed to favour nucleation. In this setup, supercooled water is placed between a slab of ice and the surface, and the ice front grows in time until the water is frozen completely. This allows the monitoring of the phase transition of the enclosed liquid-water molecules into ordered ice structures with an unbiased brute-force approach. As the nucleation of water starts in the interface between ice and liquid water, the presence of the slab means that a critical nucleus for ice growth is present from the beginning of the simulation. Although this method cannot provide direct information about the mechanism of ice nucleation, it does make it feasible to study ice formation and growth on top of any surface for which accurate intermolecular potentials exist. Indeed, many such simulations have been run over the course of this thesis work; these would not have been possible using conventional MD techniques.

**2. What is the role of the surface structure and chemistry in promoting/inhibiting ice growth?**

Using the slab-seeded approach, the influence of wettability was investigated in this thesis for three lattice structures: FCC, BCC, and HCP. Even for such simple surfaces, many interesting surface effects on ice growth were observed. The relationship between the surface-water interaction and the contact angle was surface-dependent; in particular the FCC surface consistently showed lower contact angles for the same surface-water interaction due to its higher density. The first overlayer was always buckled for the BCC and HCP surfaces; in contrast the FCC surface induced a flat first overlayer for high wettabilities, and this transitioned to a buckled overlayer as the wettability was decreased. Density heat maps also produced insights into the molecular behaviour in the layers on all surfaces, which ranged from liquid-like to ice-like depending on the layer, surface type, and wettability. The underlying mechanisms for these observed differences were also discussed in detail. While these results do not provide a definitive answer to whether a surface promotes or inhibits ice growth, they do provide a greater level of detail into *how* ice forms adjacent to surfaces, and hints at the role that surface characteristics play on its formation and growth.

**3. Can MD simulations be used to study the formation of the QLL at the ice-solid interface?**

Using the slab-seeded approach, the QLL at the surface-ice interface could be studied in microscopic detail. The molecules in the interfacial region were separated into water and ice molecules using an established algorithm, which enabled the thickness of the QLL to be quantified. It was shown that this thickness peaked for moderate wettabilities, and decreased for both extremely high and extremely low wettabilities. A similar trend was observed with the self-diffusion characteristics of the molecules inside these layers as well. This was understood as resulting from the fact that the the surface below and the bulk ice above were simultaneously trying to influence the structure of the QLL, and these competing mechanisms changed as surface wettability was varied. For either very low or very high wettabilities, one of these two effects dominated, and the QLL was therefore suppressed to a greater extent. Additionally, it was shown that the FCC surface had distinct interfacial region dynamics when compared to the other surfaces. This is relevant to the MD studies of heterogeneous nucleation/growth in the literature, which have been predominantly conducted on FCC surfaces, and implies that the results obtained may not be generalisable.

### Future Work

While this thesis focused on simple crystal lattice surfaces, in theory this approach can be used to observe ice growth on a diverse variety of surfaces of engineering interest; some examples would be surfaces with varying roughness (Zhang *et al.*, 2014) or charge distribution (Glatz and Sarupria, 2016). The only requirement would be that accurate intermolecular potentials need to exist for the surface atoms. It is envisaged that, using this approach, extensive libraries of ice growth data can be created for varying surface parameters, which may be of practical significance to macroscopic experiments. Furthermore, the proposed approach can allow for of MD simulations to be performed at lower supercooling than that encountering in existing HIN studies, which allows for more reliable comparison with experimental results.

Another interesting area of future work would be the modelling of ice adhesion, with the stated aim of reducing surface adhesion stress. Indeed, it is largely accepted (Amirfazli and Antonini, 2017; Golovin *et al.*, 2016; He *et al.*, 2020) that a QLL can act as a self-lubricated layer which can decrease ice adhesion; the creation of a QLL is being considered as a promising anti-icing solution. Future MD simulations may focus on relating ice adhesion behaviour with surface characteristics and subsequent QLL structure and dynamics. Additionally, icing cycles of surface melting-refreezing are frequent in industrial anti-icing systems as well as in nature. The simulation of these icing cycles which involve multiple phase change processes can also be pursued in future MD studies. Thus, the slab-seeded ice approach can simulate many icing mechanisms encountered in both: a) anti-icing systems for the avoidance of industrial hazards; and b) natural phenomena in which ice propagation meets surfaces.

Finally, it must be acknowledged that this thesis merely scratches the surface of the unknown as far as ice growth on surfaces is concerned. Bartels-Rausch (2013) famously titled his *Nature* article on open problems in ice as “Ten things we need to know about ice and snow”. If the evidence of this author is anything to go by, there are probably many more than ‘*ten*’ important open problems!

# Appendix A

# Sample LAMMPS code of the slab-seeding approach

```
#########################################################################
##   Slab-seeding approach
#########################################################################
##       TIP4P/Ice model, LAMMPS
##       Initialization
log       log.ice_growth   #   the name of the output log file
units       metal   #   metal units. See LAMMPS documentation
dimension       3   #   3D geometry
boundary       p p p   #   Periodic boundary condition in all 3-dimensions
neighbor       2.0 bin   #   2 Å skin distance
neigh_modify       delay 1   #   How often neighboring list is modified
processors       6 4 *   #   Number of processors in each dimension
read_data       data.ice_growth   #   Read the data file

##################### INTERACTION PARAMETERS ##########################

## Groups based on atoms types and IDs
group       oxygen type 1
group       hydrogen type 2
group       surface type 3
group       water id 1:4896   #   group of the supercooled water molecules
group       ice id 4897:6816   #   group of the ice molecules
group       wall id 6817:7520   #   group of the surface atoms
group       molecules union water ice   #   union of the groups that contain all water
molecules

## Bond and angle parameters
```

```
bond_style      harmonic
bond_coeff      1 0.0 0.9572
angle_style     harmonic
angle_coeff     1 0.0 104.52

## Pair coefficients
pair_style      hybrid/overlay lj/cut/tip4p/long 1 2 1 1 0.1577 12.0 10.0 lj/cut 12.0   # Use of more than one pair styles in the simulation
kspace_style    pppm/tip4p 1.0e-5   #   Long-range interaction using PPPM
pair_coeff      2 2  lj/cut/tip4p/long 0.0 0.0   #   H-H
pair_coeff      1 1  lj/cut/tip4p/long 0.009143361 3.1668   #   O-O
pair_coeff      1 2  lj/cut/tip4p/long 0.0 0.0   #   O-H
pair_coeff      2 3  lj/cut 0.0 0.0   #   H-Al
pair_coeff      1 3  lj/cut 0.04875729545 2.87023   #   O-Al
pair_coeff      3 3  lj/cut 0.26 2.57366   #   Al-Al

###################### COMPUTE PARAMETERS ##############################

## Compute of temperatures and energies
compute     Tliq water temp/com   #   Temperature of supercooled water
compute     Tslab ice temp/com   #   Temperature of ice slab
compute     Tsurf wall temp/com   #   Temperature of the surface
compute     Kliquid water ke/atom   #   Kinetic energy of supercooled water
compute     Kw water reduce sum c_Kliquid
compute     Poperatom water pe/atom   #   Potential energy of supercooled water
compute     Pope water reduce sum c_Poperatom

fix     shake_H2O molecules shake 1.0e-4 200 0 b 1 a 1   #   Use of SHAKE algorithm for water molecules to be rigid
fix     spring_force wall spring/self 10.0   #   Spring force between the surface atoms

## Output log file
thermo_style    custom step temp c_Tliq c_Tslab c_Tsurf c_Pope c_Kw pe ke etotal
thermo      1000   #   Output every 1000 time steps
thermo_modify       flush yes   #   Make sure output is updated and not buffered if LAMMPS stops before completion
timestep    0.002   #   Time step in femto-seconds

## Velocities randomly generated for a specified temperature
velocity    water create 240.0 82184 mom yes rot yes
```

```
velocity        ice create 240.0 82184 mom yes rot yes
velocity        wall create 240.0 82184 mom yes rot yes

## Output trajectory files
fix         waterconstt water nvt temp 240.0 240.0 0.1   #   Apply canonical ensemble at
the supercooled water
fix        iceconstt ice nvt temp 240.0 240.0 0.1   #   Apply canonical ensemble at the ice
slab
fix        wallconstt wall nvt temp 240.0 240.0 0.1   #   Apply canonical ensemble at the
surface
dump        1 all custom 1000 240K-equlib.lammpstrj id type x y z vx vy vz
run         1000000
undump        1
unfix        waterconstt   #   Turn off canonical ensemble at the ice slab
unfix        wallconstt   #   Turn off canonical ensemble at the surface

reset_timestep        0
fix        waterconstt water nve   #   Apply micro-canonical ensemble at the ice slab
fix        wallconstt wall nve   #   Apply micro-canonical ensemble at the surface
dump        1 all custom 10000 240K.lammpstrj id type x y z vx vy vz
run         5000000 every 2500000 "write_restart restart.*"
undump        1
```

# References


Abascal, J. L. and Vega, C. "A general purpose model for the condensed phases of water: TIP4P/2005". *Journal of Chemical Physics*, 123(23):234505, 2005.

Abascal, J. L., Sanz, E., Fernández, R. G., and Vega, C. "A potential model for the study of ices and amorphous water: TIP4P/Ice". *Journal of Chemical Physics*, 122 (23):234511, 2005.

Abrams, C. and Bussi, G. "Enhanced sampling in molecular dynamics using metadynamics, replica-exchange, and temperature-acceleration". *Entropy*, 16(1): 163–199, 2014.

Allen, M. P. and Tildesley, D. J. *Computer Simulation of Liquids*. Oxford University Press, Oxford, 2nd edition, 2017.

Allen, R. J., Frenkel, D., and Ten Wolde, P. R. "Simulating rare events in equilibrium or nonequilibrium stochastic systems". *Journal of Chemical Physics*, 124(2):024102, 2006.

Allen, R. J., Valeriani, C., and Rein Ten Wolde, P. "Forward flux sampling for rare event simulations". *Journal of Physics: Condensed Matter*, 21(46):463102, 2009.

Amirfazli, A. and Antonini, C. "Fundamentals of Anti-Icing Surfaces". In *Non-wettable Surfaces: Theory, Preparation and Applications*, chapter 11, pages 319–346. The Royal Society of Chemistry, 2017.

Atkins, P. W. and De Paula, J. *Atkins' Physical Chemistry*. Macmillan Higher Education, 8th edition, 2006.

Bai, X. M. and Li, M. "Test of classical nucleation theory via molecular-dynamics simulation". *Journal of Chemical Physics*, 122(22):1–4, 2005.

Barducci, A., Bussi, G., and Parrinello, M. "Well-tempered metadynamics: A smoothly converging and tunable free-energy method". *Physical Review Letters*, 100(2):1–4, 2008.

Bartels-Rausch, T. "Chemistry: Ten things we need to know about ice and snow". *Nature*, 494(7435):27–29, 2013.

Barthlott, W. and Neinhuis, C. "Purity of the sacred lotus, or escape from contamination in biological surfaces". *Planta*, 202(1):1, 1997.

Becker, R. and Döring, W. "Kinetische Behandlung der Keimbildung in übersättigten Dämpfen". *Annalen der Physik*, 416:719–752, 2006.

Berendsen, H. J., Grigera, J. R., and Straatsma, T. P. "The missing term in effective pair potentials". *Journal of Physical Chemistry*, 91(24):6269–6271, 1987.

Bernal, J. D. and Fowler, R. H. "A theory of water and ionic solution, with particular reference to hydrogen and hydroxyl ions". *Journal of Chemical Physics*, 1(8):515–548, 1933.

Bhabhe, A., Pathak, H., and Wyslouzil, B. E. "Freezing of heavy water (D2O) nanodroplets". *Journal of Physical Chemistry A*, 117(26):5472–5482, 2013.

Bi, Y., Cabriolu, R., and Li, T. "Heterogeneous ice nucleation controlled by the coupling of surface crystallinity and surface hydrophilicity". *Journal of Physical Chemistry C*, 120(3):1507–1514, 2016.

Bianco, V., Franzese, G., Dellago, C., and Coluzza, I. "Role of water in the selection of stable proteins at ambient and extreme thermodynamic conditions". *Physical Review X*, 7(2):1–15, 2017.

Björneholm, O., Hansen, M. H., Hodgson, A., Liu, L. M., Limmer, D. T., Michaelides, A., Pedevilla, P., Rossmeisl, J., Shen, H., Tocci, G., Tyrode, E., Walz, M. M., Werner, J., and Bluhm, H. "Water at Interfaces". *Chemical Reviews*, 116(13):7698–7726, 2016.

Bolhuis, P. G., Chandler, D., Dellago, C., and Geissler, P. L. "Transition path sampling: Throwing ropes over rough mountain passes, in the dark". *Annual Review of Physical Chemistry*, 53:291–318, 2002.

Brigham, L. W. "The Arctic Council's arctic marine shipping assessment". *Center for Oceans Law and Policy*, 14:159–176, 2010.

Campbell, J. M., Meldrum, F. C., and Christenson, H. K. "Is ice nucleation from supercooled water insensitive to surface roughness?". *Journal of Physical Chemistry C*, 119(2):1164–1169, 2015.

Carignano, M. A., Shepson, P. B., and Szleifer, I. "Molecular dynamics simulations of ice growth from supercooled water". *Molecular Physics*, 103(21-23):2957–2967, 2005.

Carignano, M., Baskaran, E., Shepson, P., and Szleifer, I. "Molecular dynamics simulation of ice growth from supercooled pure water and from salt solution". *Annals of Glaciology*, 44:113–117, 2006.

Carrasco, J., Hodgson, A., and Michaelides, A. "A molecular perspective of water at metal interfaces". *Nature Materials*, 11(8):667–674, 2012.

Chattopadhyay, S., Uysal, A., Stripe, B., Ha, Y. G., Marks, T. J., Karapetrova, E. A., and Dutta, P. "How water meets a very hydrophobic surface". *Physical Review Letters*, 105(3):1–4, 2010.

Chen, D., Gelenter, M. D., Hong, M., Cohen, R. E., and McKinley, G. H. "Icephobic surfaces induced by interfacial nonfrozen water". *ACS Applied Materials and Interfaces*, 9(4):4202–4214, 2017a.

Chen, J., Dou, R., Cui, D., Zhang, Q., Zhang, Y., Xu, F., Zhou, X., Wang, J., Song, Y., and Jiang, L. "Robust prototypical anti-icing coatings with a self-lubricating liquid water layer between ice and substrate". *ACS Applied Materials and Interfaces*, 5 (10):4026–4030, 2013.

Chen, J., Li, K., Wu, S., Liu, J., Liu, K., and Fan, Q. "Durable Anti-Icing Coatings Based on Self-Sustainable Lubricating Layer". *ACS Omega*, 2(5):2047–2054, 2017b.

Conde, M. M., Vega, C., and Patrykiejew, A. "The thickness of a liquid layer on the free surface of ice as obtained from computer simulation". *Journal of Chemical Physics*, 129(1):1–11, 2008.

Cox, S. J., Kathmann, S. M., Purton, J. A., Gillan, M. J., and Michaelides, A. "Non-hexagonal ice at hexagonal surfaces: The role of lattice mismatch". *Physical Chemistry Chemical Physics*, 14(22):7944–7949, 2012.

Cox, S. J., Raza, Z., Kathmann, S. M., Slater, B., and Michaelides, A. "The microscopic features of heterogeneous ice nucleation may affect the macroscopic morphology of atmospheric ice crystals". *Faraday Discussions*, 167:389–403, 2013.

Cox, S. J., Kathmann, S. M., Slater, B., and Michaelides, A. "Molecular simulations of heterogeneous ice nucleation. II. Peeling back the layers". *Journal of Chemical Physics*, 142(18), 2015a.

Cox, S. J., Kathmann, S. M., Slater, B., and Michaelides, A. "Molecular simulations of heterogeneous ice nucleation. I. Controlling ice nucleation through surface hydrophilicity". *Journal of Chemical Physics*, 142(18), 2015b.

Croteau, T., Bertram, A. K., and Patey, G. N. "Adsorption and structure of water on kaolinite surfaces: Possible insight into ice nucleation from grand canonical Monte Carlo calculations". *Journal of Physical Chemistry A*, 112(43):10708–10712, 2008.

Dai, Z., Lu, L., Sun, Y., Tang, Z., and Lu, X. "Wetting control through topography and surface hydrophilic/hydrophobic property changes by coarse grained simulation". *Molecular Simulation*, 43(13-16):1202–1208, 2017.

Darmanin, T. and Guittard, F. "Superhydrophobic and superoleophobic properties in nature". *Materials Today*, 18(5):273–285, 2015.

Dash, J. G., Rempel, A. W., and Wettlaufer, J. S. "The physics of premelted ice and its geophysical consequences". *Reviews of Modern Physics*, 78(3):695–741, 2006.

Davies, S. R., Hester, K. C., Lachance, J. W., Koh, C. A., and Dendy Sloan, E. "Studies of hydrate nucleation with high pressure differential scanning calorimetry". *Chemical Engineering Science*, 64(2):370–375, 2009.

Dellago, C., Bolhuis, P. G., and Geissler, P. L. *Transition Path Sampling Methods*, pages 349–391. Springer Berlin Heidelberg, Berlin, Heidelberg, 2006.

Dellago, C. and Bolhuis, P. G. "Transition path sampling and other advanced simulation techniques for rare events". *Advances in Polymer Science*, 221(1):167–233, 2009.

Dellago, C., Bolhuis, P. G., and Chandler, D. "Efficient transition path sampling: Application to Lennard-Jones cluster rearrangements". *Journal of Chemical Physics*, 108(22):9236–9245, 1998.

Dick, T. J. and Madura, J. D. "A Review of the TIP4P, TIP4P-Ew, TIP5P, and TIP5P-E Water Models". volume 1 of *Annual Reports in Computational Chemistry*, chapter 5, pages 59–74. Elsevier, 2005.

Döppenschmidt, A. and Butt, H. J. "Measuring the thickness of the liquid-like layer on ice surfaces with atomic force microscopy". *Langmuir*, 16(16):6709–6714, 2000.

Eberle, P., Tiwari, M. K., Maitra, T., and Poulikakos, D. "Rational nanostructuring of surfaces for extraordinary icephobicity". *Nanoscale*, 6(9):4874–4881, 2014.

Espinosa, J. R., Sanz, E., Valeriani, C., and Vega, C. "Homogeneous ice nucleation evaluated for several water models". *The Journal of Chemical Physics*, 141(18): 18C529, 2014.

Espinosa, J. R., Navarro, C., Sanz, E., Valeriani, C., and Vega, C. "On the time required to freeze water". *Journal of Chemical Physics*, 145(21), 2016a.

Espinosa, J. R., Vega, C., Valeriani, C., and Sanz, E. "Seeding approach to crystal nucleation". *Journal of Chemical Physics*, 144(3):211922, 2016b.

Factorovich, M. H., Molinero, V., and Scherlis, D. A. "Hydrogen-Bond Heterogeneity Boosts Hydrophobicity of Solid Interfaces". *Journal of the American Chemical Society*, 137(33):10618–10623, 2015.

Faraday. "XXIV. On regelation, and on the conservation of force ". *The London, Edinburgh, and Dublin Philosophical Magazine and Journal of Science*, 17(113): 162–169, 1859.

Farhadi, S., Farzaneh, M., and Kulinich, S. A. "Anti-icing performance of superhydrophobic surfaces". *Applied Surface Science*, 257(14):6264–6269, 2011.

Feibelman, P. J. "Lattice match in density functional calculations: ice Ih vs $\beta$-AgI". *Physical Chemistry Chemical Physics*, 10(32):4688–4691, 2008.

Fitzner, M., Sosso, G. C., Cox, S. J., and Michaelides, A. "The Many Faces of Heterogeneous Ice Nucleation: Interplay between Surface Morphology and Hydrophobicity". *Journal of the American Chemical Society*, 137(42):13658–13669, 2015.

Frenkel, D. and Smit, B. *Understanding Molecular Simulation*. Academic Press, Inc., USA, 2nd edition, 2001.

Fu, Q. T., Liu, E. J., Wilson, P., and Chen, Z. "Ice nucleation behaviour on sol-gel coatings with different surface energy and roughness". *Physical Chemistry Chemical Physics*, 17(33):21492–21500, 2015.

Furukawa, Y. "Snow and Ice Crystal Growth". In *Handbook of Crystal Growth (Second Edition)*, chapter 25, pages 1061–1112. Elsevier, Boston, 2015.

Gao, L. and McCarthy, T. J. "Teflon is hydrophilic. Comments on definitions of hydrophobic, shear versus tensile hydrophobicity, and wettability characterization". *Langmuir*, 24(17):9183–9188, 2008.

Gao, X. and Jiang, L. "Water-repellent legs of water striders". *Nature*, 432(7013):36, 2004.

Gerrard, N., Gattinoni, C., McBride, F., Michaelides, A., and Hodgson, A. "Strain relief during ice growth on a hexagonal template". *Journal of the American Chemical Society*, 141(21):8599–8607, 2019.

Glatz, B. and Sarupria, S. "The surface charge distribution affects the ice nucleating efficiency of silver iodide". *Journal of Chemical Physics*, 145(21):1–4, 2016.

Glatz, B. and Sarupria, S. "Heterogeneous Ice Nucleation: Interplay of Surface Properties and Their Impact on Water Orientations". *Langmuir*, 34(3):1190–1198, 2018.

Goertz, M. P., Houston, J. E., and Zhu, X. Y. "Hydrophilicity and the viscosity of interfacial water". *Langmuir*, 23(10):5491–5497, 2007.

Golovin, K., Kobaku, S. P., Lee, D. H., DiLoreto, E. T., Mabry, J. M., and Tuteja, A. "Designing durable icephobic surfaces". *Science advances*, 2(3):e1501496, 2016.

Guo, P., Zheng, Y., Wen, M., Song, C., Lin, Y., and Jiang, L. "Icephobic/anti-icing properties of micro/nanostructured surfaces". *Advanced Materials*, 24(19):2642–2648, 2012.

Haji-Akbari, A. and Debenedetti, P. G. "Computational investigation of surface freezing in a molecular model of water". *Proceedings of the National Academy of Sciences of the United States of America*, 114(13):3316–3321, 2017.

Haji-Akbari, A., DeFever, R. S., Sarupria, S., and Debenedetti, P. G. "Suppression of sub-surface freezing in free-standing thin films of a coarse-grained model of water". *Physical Chemistry Chemical Physics*, 16(47):25916–25927, 2014.

Haq, S., Clay, C., Darling, G. R., Zimbitas, G., and Hodgson, A. "Growth of intact water ice on Ru(0001) between 140 and 160 K: Experiment and density-functional theory calculations". *Physical Review B - Condensed Matter and Materials Physics*, 73(11):1–11, 2006.

He, Z., Zhuo, Y., Wang, F., He, J., and Zhang, Z. "Design and preparation of icephobic PDMS-based coatings by introducing an aqueous lubricating layer and macro-crack initiators at the ice-substrate interface". *Progress in Organic Coatings*, 147:105737, 2020.

Hockney, R. W. and Eastwood, J. W. *Computer Simulation Using Particles*. Taylor & Francis, Inc., USA, 1988.

Hoover, W. G. "Canonical dynamics: Equilibrium phase-space distributions". *Physical Review A*, 31(3):1695–1697, 1985.

Huang, H., Yarmush, M. L., and Usta, O. B. "Long-term deep-supercooling of large-volume water and red cell suspensions via surface sealing with immiscible liquids". *Nature Communications*, 9(1):1–10, 2018.

Huang, X., Tepylo, N., Pommier-Budinger, V., Budinger, M., Bonaccurso, E., Villedieu, P., and Bennani, L. "A survey of icephobic coatings and their potential use in a hybrid coating/active ice protection system for aerospace applications". *Progress in Aerospace Sciences*, 105:74–97, 2019.

Hudait, A., Allen, M. T., and Molinero, V. "Sink or Swim: Ions and Organics at the Ice-Air Interface". *Journal of the American Chemical Society*, 139(29):10095–10103, 2017.

Jellinek, H. H. "Liquidlike layers on ice". *Journal of Applied Physics*, 32(9):1793, 1961.

Jha, K., Anim-Danso, E., Bekele, S., Eason, G., and Tsige, M. "On Modulating Interfacial Structure towards Improved Anti-Icing Performance". *Coatings*, 6(1): 3, 2016.

Jiang, J., Li, G. X., Sheng, Q., and Tang, G. H. "Microscopic mechanism of ice nucleation: The effects of surface rough structure and wettability". *Applied Surface Science*, 510:145520, 2020.

Jiménez-Ángeles, F. and Firoozabadi, A. "Contact Angle, Liquid Film, and Liquid-Liquid and Liquid-Solid Interfaces in Model Oil-Brine-Substrate Systems". *Journal of Physical Chemistry C*, 120(22):11910–11917, 2016.

Jones, J. E. "On the Determination of Molecular Fields. I. From the Variation of the Viscosity of a Gas with Temperature". *Proceedings of the Royal Society of London.*

*Series A, Containing Papers of a Mathematical and Physical Character*, 106(738): 441–462, 1924a.

Jones, J. E. "On the determination of molecular fields.-II. From the equation of state of a gas". *Proceedings of the Royal Society of London. Series A, Containing Papers of a Mathematical and Physical Character*, 106(738):463–477, 1924b.

Jorgensen, W. L., Chandrasekhar, J., Madura, J. D., Impey, R. W., and Klein, M. L. "Comparison of simple potential functions for simulating liquid water". *The Journal of Chemical Physics*, 79(2):926–935, 1983.

Jung, S., Dorrestijn, M., Raps, D., Das, A., Megaridis, C. M., and Poulikakos, D. "Are superhydrophobic surfaces best for icephobicity?". *Langmuir*, 27(6):3059–3066, 2011.

Karim, O. A. and Haymet, A. D. J. "The ice/water interface: A molecular dynamics simulation study". *The Journal of Chemical Physics*, 89(11):6889–6896, 1988.

Kelton, K. F. "Crystal Nucleation in Liquids and Glasses". In *Solid State Physics*, volume 45, pages 75–177. Academic Press, 1991.

Kim, P., Wong, T. S., Alvarenga, J., Kreder, M. J., Adorno-Martinez, W. E., and Aizenberg, J. "Liquid-infused nanostructured surfaces with extreme anti-ice and anti-frost performance". *ACS Nano*, 6(8):6569–6577, 2012.

Kling, T., Kling, F., and Donadio, D. "Structure and Dynamics of the Quasi-Liquid Layer at the Surface of Ice from Molecular Simulations". *Journal of Physical Chemistry C*, 122(43):24780–24787, 2018.

Knott, B. C., Molinero, V., Doherty, M. F., and Peters, B. "Homogeneous nucleation of methane hydrates: Unrealistic under realistic conditions". *Journal of the American Chemical Society*, 134(48):19544–19547, 2012.

Kumar, S., Rosenberg, J. M., Bouzida, D., Swendsen, R. H., and Kollman, P. A. "The weighted histogram analysis method for free-energy calculations on biomolecules. I. The method". *Journal of Computational Chemistry*, 13(8):1011–1021, 1992.

Laforte, J. L., Allaire, M. A., and Laflamme, J. "State-of-the-art on power line de-icing". *Atmospheric Research*, 46(1-2):143–158, 1998.

Laio, A. "Escaping Free-Energy Minima". *Proceedings of the National Academy of Sciences of the United States of America*, 99(20):12562–12566, 2002.

Laio, A. and Gervasio, F. L. "Metadynamics: A method to simulate rare events and reconstruct the free energy in biophysics, chemistry and material science". *Reports on Progress in Physics*, 71(12):126601, 2008.

Lamb, D. and Verlinde, J. *Physics and Chemistry of Clouds*. Cambridge University Press, Cambridge, 2011.

Li, C., Gao, X., and Li, Z. "Roles of Surface Energy and Temperature in Heterogeneous Ice Nucleation". *Journal of Physical Chemistry C*, 121(21):11552–11559, 2017.

Li, K., Xu, S., Shi, W., He, M., Li, H., Li, S., Zhou, X., Wang, J., and Song, Y. "Investigating the effects of solid surfaces on Ice nucleation". *Langmuir*, 28(29): 10749–10754, 2012.

Li, K., Xu, S., Chen, J., Zhang, Q., Zhang, Y., Cui, D., Zhou, X., Wang, J., and Song, Y. "Viscosity of interfacial water regulates ice nucleation". *Applied Physics Letters*, 104(10):10–14, 2014.

Li, Q. and Guo, Z. "Fundamentals of icing and common strategies for designing biomimetic anti-icing surfaces". *Journal of Materials Chemistry A*, 6(28):13549–13581, 2018.

Li, T., Donadio, D., and Galli, G. "Ice nucleation at the nanoscale probes no man's land of water". *Nature Communications*, 4(1887):1–6, 2013.

Li, W. Z., Chen, C., and Yang, J. "Molecular dynamics simulation of self-diffusion coefficient and its relation with temperature using simple Lennard-Jones potential". *Heat Transfer - Asian Research*, 37(2):86–93, 2008.

Li, Y. and Somorjai, G. A. "Surface premelting of ice". *Journal of Physical Chemistry C*, 111(27):9631–9637, 2007.

Limmer, D. T. "Closer look at the surface of ice". *Proceedings of the National Academy of Sciences of the United States of America*, 113(44):12347–12349, 2016.

Limmer, D. T. and Chandler, D. "Premelting, fluctuations, and coarse-graining of water-ice interfaces". *Journal of Chemical Physics*, 141(18):18C505, 2014.

Lindenberg, C. and Mazzotti, M. "Effect of temperature on the nucleation kinetics of $\alpha$ l-glutamic acid". *Journal of Crystal Growth*, 311(4):1178–1184, 2009.

Ling, E. J. Y., Uong, V., Renault-Crispo, J. S., Kietzig, A. M., and Servio, P. "Reducing Ice Adhesion on Nonsmooth Metallic Surfaces: Wettability and Topography Effects". *ACS Applied Materials and Interfaces*, 8(13):8789–8800, 2016.

Liu, J., Zhu, C., Liu, K., Jiang, Y., Song, Y., Francisco, J. S., Zeng, X. C., and Wang, J. "Distinct ice patterns on solid surfaces with various wettabilities". *Proceedings of the National Academy of Sciences of the United States of America*, 114(43): 11285–11290, 2017.

Lorentz, H. "Ueber die Anwendung des Satzes vom Virial in der kinetischen Theorie der Gase". *Annalen der Physik*, 248(1):127–136, 1881.

Lupi, L. and Molinero, V. "Does hydrophilicity of carbon particles improve their ice nucleation ability?". *Journal of Physical Chemistry A*, 118(35):7330–7337, 2014.

Lupi, L., Hudait, A., and Molinero, V. "Heterogeneous nucleation of ice on carbon surfaces". *Journal of the American Chemical Society*, 136(8):3156–3164, 2014.

Lupi, L., Peters, B., and Molinero, V. "Pre-ordering of interfacial water in the pathway of heterogeneous ice nucleation does not lead to a two-step crystallization mechanism". *Journal of Chemical Physics*, 145(21), 2016.

MacKerell, A. D., Bashford, D., Bellott, M., Dunbrack, R. L., Evanseck, J. D., Field, M. J., Fischer, S., Gao, J., Guo, H., Ha, S., Joseph-McCarthy, D., Kuchnir, L., Kuczera, K., Lau, F. T., Mattos, C., Michnick, S., Ngo, T., Nguyen, D. T., Prodhom, B., Reiher, W. E., Roux, B., Schlenkrich, M., Smith, J. C., Stote, R., Straub, J., Watanabe, M., Wiórkiewicz-Kuczera, J., Yin, D., and Karplus, M. "All-atom empirical potential for molecular modeling and dynamics studies of proteins". *Journal of Physical Chemistry B*, 102(18):3586–3616, 1998.

Mackerell, A. D. "Empirical force fields for biological macromolecules: Overview and issues". *Journal of Computational Chemistry*, 25(13):1584–1604, 2004.

Mahoney, M. W. and Jorgensen, W. L. "A five-site model for liquid water and the reproduction of the density anomaly by rigid, nonpolarizable potential functions". *Journal of Chemical Physics*, 112(20):8910–8922, 2000.

Maitra, T., Tiwari, M. K., Antonini, C., Schoch, P., Jung, S., Eberle, P., and Poulikakos, D. "On the nanoengineering of superhydrophobic and impalement resistant surface textures below the freezing temperature". *Nano Letters*, 14(1):172–182, 2014.

Mason, B. J. "Physics of Clouds and Precipitation". *Nature*, 174(4438):957–959, 1954.

Meier, K., Laesecke, A., and Kabelac, S. "A Molecular Dynamics Simulation Study of the Self-Diffusion Coefficient and Viscosity of the Lennard-Jones Fluid". *International Journal of Thermophysics*, 22(1):161–173, 2001.

Meuler, A. J., Smith, J. D., Varanasi, K. K., Mabry, J. M., McKinley, G. H., and Cohen, R. E. "Relationships between water wettability and ice adhesion". *ACS Applied Materials and Interfaces*, 2(11):3100–3110, 2010.

Michaelides, A. and Morgenstern, K. "Ice nanoclusters at hydrophobic metal surfaces". *Nature Materials*, 6(8):597–601, 2007.

Mishchenko, L., Hatton, B., Bahadur, V., Taylor, J. A., Krupenkin, T., and Aizenberg, J. "Design of ice-free nanostructured surfaces based on repulsion of impacting water droplets". *ACS Nano*, 4(12):7699–7707, 2010.

Mochizuki, K. and Molinero, V. "Antifreeze Glycoproteins Bind Reversibly to Ice via Hydrophobic Groups". *Journal of the American Chemical Society*, 140(14):4803–4811, 2018.

Molinero, V. and Moore, E. B. "Water modeled as an intermediate element between carbon and silicon". *Journal of Physical Chemistry B*, 113(13):4008–4016, 2009.

Momen, G., Farzaneh, M., and Jafari, R. "Wettability behaviour of RTV silicone rubber coated on nanostructured aluminium surface". *Applied Surface Science*, 257(15): 6489–6493, 2011.

Moore, E. B., de la Llave, E., Welke, K., Scherlis, D. A., and Molinero, V. "Freezing, melting and structure of ice in a hydrophilic nanopore". *Physical Chemistry Chemical Physics*, 12(16):4124–4134, 2010.

Murata, K. I., Asakawa, H., Nagashima, K., Furukawa, Y., and Sazaki, G. "Thermodynamic origin of surface melting on ice crystals". *Proceedings of the National Academy of Sciences of the United States of America*, 113(44):E6741–E6748, 2016.

Nada, H. and Furukawa, Y. "Anisotropic growth kinetics of ice crystals from water studied by molecular dynamics simulation". *Journal of Crystal Growth*, 169(3): 587–597, 1996.

Nada, H. and Furukawa, Y. "Anisotropy in structural phase transitions at ice surfaces: A molecular dynamics study". *Applied Surface Science*, 121-122:445–447, 1997.

Nada, H. and Furukawa, Y. "Anisotropy in growth kinetics at interfaces between proton-disordered hexagonal ice and water: A molecular dynamics study using the six-site model of H2O". *Journal of Crystal Growth*, 283(1-2):242–256, 2005.

Nguyen, A. H. and Molinero, V. "Identification of Clathrate Hydrates, Hexagonal Ice, Cubic Ice, and Liquid Water in Simulations: The CHILL+ Algorithm". *Journal of Physical Chemistry B*, 119(29):9369–9376, 2015.

Nie, S., Feibelman, P. J., Bartelt, N. C., and Thürmer, K. "Pentagons and Heptagons in the First Water Layer on Pt(111)". *Physical Review Letters*, 105(2):26102, 2010.

Nosé, S. "A molecular dynamics method for simulations in the canonical ensemble". *Molecular Physics*, 52(2):255–268, 1984.

Nosonovsky, M. and Hejazi, V. "Why superhydrophobic surfaces are not always icephobic". *ACS Nano*, 6(10):8488–8491, 2012.

Özilgen, S. and Reid, D. S. "The Use of DSC to Study the Effects of Solutes on Heterogeneous Ice Nucleation Kinetics in Model Food Emulsions". *LWT - Food Science and Technology*, 26(2):116–120, 1993.

Parent, O. and Ilinca, A. "Anti-icing and de-icing techniques for wind turbines: Critical review". *Cold Regions Science and Technology*, 65(1):88–96, 2011.

Pedevilla, P., Cox, S. J., Slater, B., and Michaelides, A. "Can Ice-Like Structures Form on Non-Ice-Like Substrates? The Example of the K-feldspar Microcline". *Journal of Physical Chemistry C*, 120(12):6704–6713, 2016.

Pedevilla, P., Fitzner, M., Sosso, G. C., and Michaelides, A. "Heterogeneous seeded molecular dynamics as a tool to probe the ice nucleating ability of crystalline surfaces". *Journal of Chemical Physics*, 149(7), 2018.

Pereyra, R. G., Szleifer, I., and Carignano, M. A. "Temperature dependence of ice critical nucleus size". *Journal of Chemical Physics*, 135(3):034508, 2011.

Pickering, I., Paleico, M., Sirkin, Y. A., Scherlis, D. A., and Factorovich, M. H. "Grand Canonical Investigation of the Quasi Liquid Layer of Ice: Is It Liquid?". *Journal of Physical Chemistry B*, 122(18):4880–4890, 2018.

Plimpton, S. "Fast Parallel Algorithms for Short-Range Molecular Dynamics". *Journal of Computational Physics*, 117(1):1–19, 1995.

Pollock, E. L. and Glosli, J. "Comments on P3M, FMM, and the Ewald method for large periodic Coulombic systems". *Computer Physics Communications*, 95(2-3): 93–110, 1996.

Price, W. S., Ide, H., and Arata, Y. "Self-Diffusion of Supercooled Water to 238 K Using PGSE NMR Diffusion Measurements". *Journal of Physical Chemistry A*, 103(4):448–450, 1999.

Pruppacher, H. R. and Klett, J. D. *Microphysics of Clouds and Precipitation.* Springer, 2nd edition, 1997.

Qiu, Y. and Molinero, V. "Why Is It so Difficult to Identify the Onset of Ice Premelting?". *Journal of Physical Chemistry Letters*, 9(17):5179–5182, 2018.

Quigley, D. and Rodger, P. M. "Metadynamics simulations of ice nucleation and growth". *Journal of Chemical Physics*, 128(15):154518, 2008.

R. Gent, P. Dart, T. C. "Aircraft icing". *The Royal Society*, 358(1776):2873–2911, 2000.

Raabe, G. *Molecular Simulation Studies on Thermophysical Properties - With Application to Working Fluids. Springer Series Molecular Modeling and Simulation.* Springer, 1st edition, 2017.

Radhakrishnan, R. and Trout, B. L. "Nucleation of Crystalline Phases of Water in Homogeneous and Inhomogeneous Environments". *Physical Review Letters*, 90 (15):4, 2003.

Ramachandran, R., Kozhukhova, M., Sobolev, K., and Nosonovsky, M. "Anti-icing superhydrophobic surfaces: Controlling entropic molecular interactions to design novel icephobic concrete". *Entropy*, 18(4):132, 2016.

Reinhardt, A. *Computer simulation of the homogeneous nucleation of ice.* PhD thesis, Oxford University, UK, 2013.

Reinhardt, A., Doye, J. P., Noya, E. G., and Vega, C. "Local order parameters for use in driving homogeneous ice nucleation with all-atom models of water". *Journal of Chemical Physics*, 137(19):194504, 2012.

Roelands, C. P., Roestenberg, R. R., Ter Horst, J. H., Kramer, H. J., and Jansens, P. J. "Development of an experimental method to measure nucleation rates in reactive precipitation". *Crystal Growth and Design*, 4(5):921–928, 2004.

Ruckenstein, E. and Djikaev, Y. S. "Recent developments in the kinetic theory of nucleation". *Advances in Colloid and Interface Science*, 118(1-3):51–72, 2005.

Russo, J. and Tanaka, H. "The microscopic pathway to crystallization in supercooled liquids". *Scientific Reports*, 2(505):1–8, 2012.

Ryckaert, J. P., Ciccotti, G., and Berendsen, H. J. "Numerical integration of the cartesian equations of motion of a system with constraints: molecular dynamics of n-alkanes". *Journal of Computational Physics*, 23(3):327–341, 1977.

Rykaczewski, K., Anand, S., Subramanyam, S. B., and Varanasi, K. K. "Mechanism of frost formation on lubricant-impregnated surfaces". *Langmuir*, 29(17):5230–5238, 2013.

Saleema, N. and Farzaneh, M. "Thermal effect on superhydrophobic performance of stearic acid modified ZnO nanotowers". *Applied Surface Science*, 254(9):2690–2695, 2008.

Santiso, E. E., Herdes, C., and Müller, E. A. "On the calculation of solid-fluid contact angles from molecular dynamics". *Entropy*, 15(9):3734–3745, 2013.

Sanz, E., Vega, C., Espinosa, J. R., Caballero-Bernal, R., Abascal, J. L., and Valeriani, C. "Homogeneous ice nucleation at moderate supercooling from molecular simulation". *Journal of the American Chemical Society*, 135(40):15008–15017, 2013.

Sarkar, D. K., Farzaneh, M., and Paynter, R. W. "Superhydrophobic properties of ultrathin rf-sputtered Teflon films coated etched aluminum surfaces". *Materials Letters*, 62(8-9):1226–1229, 2008.

Sayer, T. and Cox, S. J. "Stabilization of AgI's polar surfaces by the aqueous environment, and its implications for ice formation". *Physical Chemistry Chemical Physics*, 21(27):14546–14555, 2019.

Schutzius, T. M., Jung, S., Maitra, T., Eberle, P., Antonini, C., Stamatopoulos, C., and Poulikakos, D. "Physics of icing and rational design of surfaces with extraordinary icephobicity". *Langmuir*, 31(17):4807–4821, 2015.

Sellberg, J. A., Huang, C., McQueen, T. A., Loh, N. D., Laksmono, H., Schlesinger, D., Sierra, R. G., Nordlund, D., Hampton, C. Y., Starodub, D., Deponte, D. P., Beye, M., Chen, C., Martin, A. V., Barty, A., Wikfeldt, K. T., Weiss, T. M., Caronna, C., Feldkamp, J., Skinner, L. B., Seibert, M. M., Messerschmidt, M., Williams, G. J., Boutet, S., Pettersson, L. G., Bogan, M. J., and Nilsson, A. "Ultrafast X-ray probing of water structure below the homogeneous ice nucleation temperature". *Nature*, 510 (7505):381–384, 2014.

Shultz, M. J. "Ice Surfaces". *Annual Review of Physical Chemistry*, 68(1):285–304, 2017.

Singh, J. K. and Müller-Plathe, F. "On the characterization of crystallization and ice adhesion on smooth and rough surfaces using molecular dynamics". *Applied Physics Letters*, 104(2):2–7, 2014.

Sojoudi, H., Wang, M., Boscher, N. D., McKinley, G. H., and Gleason, K. K. "Durable and scalable icephobic surfaces: similarities and distinctions from superhydrophobic surfaces". *Soft Matter*, 12(7):1938–1963, 2016.

Solangi, A. R. *Icing Effects on Power Lines and Anti-icing and De-icing Methods*. Master's thesis, The Arctic University of Norway, 2018.

Sosso, G. C., Chen, J., Cox, S. J., Fitzner, M., Pedevilla, P., Zen, A., and Michaelides, A. "Crystal Nucleation in Liquids: Open Questions and Future Challenges in Molecular Dynamics Simulations". *Chemical Reviews*, 116(12):7078–7116, 2016a.

Sosso, G. C., Li, T., Donadio, D., Tribello, G. A., and Michaelides, A. "Microscopic Mechanism and Kinetics of Ice Formation at Complex Interfaces: Zooming in on Kaolinite". *Journal of Physical Chemistry Letters*, 7(13):2350–2355, 2016b.

Steinhardt, P. J., Nelson, D. R., and Ronchetti, M. "Bond-orientational order in liquids and glasses". *Physical Review B*, 28(2):784–805, 1983.

Stillinger, F. H. and Weber, T. A. "Computer simulation of local order in condensed phases of silicon". *Physical Review B*, 31(8):5262–5271, 1985.

Sunyaev, R. A. "On the Theory of New Phase Formation. Cavitation". In Sunyaev, R. A., editor, *Selected Works of Yakov Borisovich Zeldovich, Volume I*, chapter 10, pages 120–137. Princeton University Press, 2014.

Swope, W. C., Andersen, H. C., Berens, P. H., and Wilson, K. R. "A computer simulation method for the calculation of equilibrium constants for the formation of physical clusters of molecules: Application to small water clusters". *Journal of Chemical Physics*, 76(1):637–649, 1982.

Ten Wolde, P. R., Ruiz-Montero, M. J., and Frenkel, D. "Numerical calculation of the rate of crystal nucleation in a Lennard-Jones system at moderate undercooling". *Journal of Chemical Physics*, 104(24):9932–9947, 1996.

Tian, J., Dong, X., Xi, B., Minnis, P., Smith Jr, W. L., Sun-Mack, S., Thieman, M., and Wang, J. "Comparisons of Ice Water Path in Deep Convective Systems Among Ground-Based, GOES, and CERES-MODIS Retrievals". *Journal of Geophysical Research: Atmospheres*, 123(3):1708–1723, 2018.

Torrie, G. M. and Valleau, J. P. "Nonphysical sampling distributions in Monte Carlo free-energy estimation: Umbrella sampling". *Journal of Computational Physics*, 23 (2):187–199, 1977.

Toxvaerd, S. and Dyre, J. C. "Communication: Shifted forces in molecular dynamics". *Journal of Chemical Physics*, 134(8):1–5, 2011.

Turnbull, D. and Fisher, J. C. "Rate of nucleation in condensed systems". *Journal of Chemical Physics*, 17(1):71–73, 1949.

Turnbull, D. and Vonnegut, B. "Nucleation Catalysis". *Industrial & Engineering Chemistry*, 44(6):1292–1298, 1952.

Uchida, S., Fujiwara, K., and Shibahara, M. "Molecular Dynamics Study of Interactions between the Water/ice Interface and a Nanoparticle in the Vicinity of a Solid Surface". *Nanoscale and Microscale Thermophysical Engineering*, 24(2):53–65, 2020.

Varanasi, K. K., Deng, T., Smith, J. D., Hsu, M., and Bhate, N. "Frost formation and ice adhesion on superhydrophobic surfaces". *Applied Physics Letters*, 97(23):234102, 2010.

Volmer, M. and Weber, A. "Keimbildung in übersättigten Gebilden". *Zeitschrift für Physikalische Chemie*, 119U:277–301, 1926.

Vrbka, L. and Jungwirth, P. "Brine rejection from freezing salt solutions: A molecular dynamics study". *Physical Review Letters*, 95(14):1–4, 2005.

Vrbka, L. and Jungwirth, P. "Molecular dynamics simulations of freezing of water and salt solutions". *Journal of Molecular Liquids*, 134(1-3):64–70, 2007.

Wei, N., Lv, C., and Xu, Z. "Wetting of graphene oxide: A molecular dynamics study". *Langmuir*, 30(12):3572–3578, 2014.

Wilson, P. W., Lu, W., Xu, H., Kim, P., Kreder, M. J., Alvarenga, J., and Aizenberg, J. "Inhibition of ice nucleation by slippery liquid-infused porous surfaces (SLIPS)". *Physical Chemistry Chemical Physics*, 15(2):581–585, 2013.

Wong, T. S., Kang, S. H., Tang, S. K., Smythe, E. J., Hatton, B. D., Grinthal, A., and Aizenberg, J. "Bioinspired self-repairing slippery surfaces with pressure-stable omniphobicity". *Nature*, 477(7365):443–447, 2011.

Xu, Y., Xu, D., and Liang, J. *Computational Methods for Protein Structure Prediction and Modeling: Volume 1: Basic Characterization.* Biological and Medical Physics, Biomedical Engineering. Springer New York, 2007.

Yan, J. Y. and Patey, G. N. "Heterogeneous ice nucleation induced by electric fields". *Journal of Physical Chemistry Letters*, 2(20):2555–2559, 2011.

Yang, X., Lu, J., Wang, X. J., and Ching, C. B. "Effect of sodium chloride on the nucleation and polymorphic transformation of glycine". *Journal of Crystal Growth*, 310(3):604–611, 2008.

Yang, Y. I., Shao, Q., Zhang, J., Yang, L., and Gao, Y. Q. "Enhanced sampling in molecular dynamics". *Journal of Chemical Physics*, 151(7), 2019.

Zaragoza, A., Conde, M. M., Espinosa, J. R., Valeriani, C., Vega, C., and Sanz, E. "Competition between ices Ih and Ic in homogeneous water freezing". *The Journal of Chemical Physics*, 143(13):134504, 2015.

Zeng, Q. and Li, K. "Quasi-Liquid Layer on Ice and Its Effect on the Confined Freezing of Porous Materials". *Crystals*, 9(5):250, 2019.

Zhang, X. X., Chen, M., and Fu, M. "Impact of surface nanostructure on ice nucleation". *Journal of Chemical Physics*, 141(12), 2014.

Zhang, Z. and Liu, X. Y. "Control of ice nucleation: Freezing and antifreeze strategies". *Chemical Society Reviews*, 47(18):7116–7139, 2018.

Zheng, Y., Gao, X., and Jiang, L. "Directional adhesion of superhydrophobic butterfly wings". *Soft Matter*, 3(2):178–182, 2007.

Zhou, H., Wang, H., Niu, H., Gestos, A., Wang, X., and Lin, T. "Fluoroalkyl silane modified silicone rubber/nanoparticle composite: A super durable, robust superhydrophobic fabric coating". *Advanced Materials*, 24(18):2409–2412, 2012.

Zielke, S. A., Bertram, A. K., and Patey, G. N. "Simulations of Ice Nucleation by Kaolinite (001) with Rigid and Flexible Surfaces". *Journal of Physical Chemistry B*, 120(8):1726–1734, 2016.